

Chapter 4

Characterization Problems and Results

The Ω -methods have been presented in the previous chapters. In this chapter, the CADIS- Ω -method is applied to a number of small, anisotropy-inducing problems. Recall that the Ω -methods are a version of CADIS and FW-CADIS that use an adjusted contribution-based flux rather than a pure-adjoint flux to generate biasing parameters. The CADIS- Ω -method's performance is compared to CADIS and standard nonbiased Monte Carlo. Because the Ω -methods have been designed to generate variance reduction parameters in problems where there is a strong degree of anisotropy in the flux, their characterization is dependent on testing them in anisotropic problems. This chapter begins with a presentation of the characterization problems that have been designed to induce anisotropy in the particle flux by different physical mechanisms. The results of the Ω -methods when applied to these problems follows. Two problems that highlight interesting aspects of the Ω -methods are subsequently used in a deeper parametric study to determine the Ω -method's sensitivity to different angular flux information. Using the results obtained from this study, recommendations on favorable parameters with which to run the Ω -methods are made.

4.1 Description of the Characterization Problems

In characterizing the Ω -methods, we aim to determine in which problems they perform well, and then quantify that success. First, we must determine how effective the Ω -methods are in reducing the variance for a tally result in Monte Carlo. This is done by assessing and comparing the FOMs between different VR methods. Also, the method must be investigated using a diverse set of anisotropic problems. By constructing problems that have different mechanisms causing or inducing anisotropy in the flux, potential strengths or weaknesses of the method can be isolated as a function of these mechanisms. In addition to comparing the FOMs or REs between methods, another desirable metric by which to measure the

method's success given the degree of anisotropy in the problem. Recall that different means of quantifying the flux anisotropy are described in Section 3.2.1. With a diverse selection of characterization problems, we obtain variation in the flux anisotropy in each problem as well as the resultant FOMs. This provides us with a path forward with which to use the Ω -methods in a deeper angular-sensitivity study.

4.1.1 Identification of Anisotropy-Inducing Physics

There exists a rich history of using hybrid methods in problems with strong angular dependence, as summarized in Chapter 2. Angular dependence may appear in a problem through several means—both physical and computational. Mosher et al. [61] noted in their threat-detection work with ADVANTG that problems with strongly directional sources and problems with “thin” materials like air were difficult for ADVANTG to effectively reduce the variance. They attributed this to strongly anisotropic behavior of the importance function that were not reflected well by the scalar flux. Sweezy [65] also found that weight windows obtained from a hybrid S_N calculation were not good for a dogleg void problem, where ray effects from the S_N calculation generated poorer weight windows than a method without ray effects¹. Though they did not observe ray effects in the importance map for the problem, Peplow et al. [52] also found that CADIS struggled with thin material streaming in a spherical boat test problem.

The examples of angle-dependence in problems affecting hybrid methods' success illustrate that the flux can have anisotropy resulting from more than one mechanism. Based on these examples, we have identified several separate processes that affect the flux anisotropy. These processes can be grouped into three categories:

- anisotropy in the flux resulting from strongly directional sources,
- anisotropy resulting from strong differences between material properties (this can be due to differences in materials spatially or due to changes in interaction probabilities as a function of energy),
- anisotropy in the flux from algorithmic limitations (ray effects).

These processes overlap. Consequently, this section continues with a brief discussion about how each mechanism applies to anisotropic problems.

A strongly directional source is one that emits particles in a very small solid angle of angle-space. The most extreme example of this would be a monodirectional source, while an extreme opposite would be an isotropic source. This particular anisotropy-creating process is source-specific and does not depend on the rest of the problem configuration. Our characterization problems will have sources of both types to ensure the full parameter space is covered.

¹Recall from Sections 2.2.3 and 2.6 that ray effects are a nonphysical effect seen in the flux solution that arise from the angular discretization of the problem. Ray effects are common in situations where there are strong streaming effects or if a strong source is emitting particles with long mean free paths in the material.

The next subset of anisotropy-inducing processes are those that result from strong differences between material properties. As noted, this can be from the geometric configuration of the problem, or from variations in the cross sections within a geometric location. To illustrate the differences in the way the problem can physically induce anisotropy in the flux, several simple thought experiments will be presented.

Consider first the extreme example of material A which has some low absorption probability, and material B which is a pure absorber. Only particles that travel through material A will eventually reach the tally location. This is an example of a type of problem with strong material heterogeneity. In constructing a set of characterization problems, creating channels through which particles will preferentially travel will induce anisotropy in the flux. These types of flow paths are also of interest in shielding application problems, and were discussed at length in Section 2.2.3. In this type of problem, material A can either have a low scattering probability (airlike), or it can be highly scattering. In scattering events, neutral particles can either lose very little energy with a high Z material, like lead, or they can lose a lot of energy with a low Z material. These are considered separately, because the energy spectrum of the particles affects the particle's interaction probability.

Consider another example of an isotropic point source immersed in a pure thin material. Because particles have a very low probability of interaction in the material, they will travel almost uniformly outwards away from the point source. At some distance from the point source, the majority of the particles in a cell will be traveling in the same direction. This is an example of a problem with streaming paths. To summarize, we have identified several sub-distinctions of this type of effect: regions with streaming where particles far from the source are primarily monodirectional, regions that are highly scattering where particles have a preferential flowpath through one material and are downscattered in energy, and regions with strong material heterogeneity where particles have preferential flowpaths but are not necessarily downscattered in energy. It should be noted that while streaming and scattering problems will almost always be subsets of problems with material homogeneity, it is possible to have a highly scattering or a streaming problem without material heterogeneity.

The last factor that can influence anisotropy in the flux solution is ray effects. While ray effects are a result of anisotropy in the flux solution, this is a nonphysical effect and can actually affect variance reduction performance. In the case of ray effects, we aim to see if the Ω -methods are more robust in avoiding them in generating VR parameters. Because ray effects are primarily seen in large regions with low interaction probabilities, some of the characterization problems must incorporate these types of regions into their geometries.

In this subsection, four primary physical mechanisms by which the flux may be anisotropic were identified. These are: streaming paths, problems with high scattering effects, problems with high material heterogeneity (specifically with materials with strong differences in scattering and absorption probabilities), and problems with monodirectional sources. As described in the preceding paragraphs, a few of these mechanisms may overlap with one another. Together, they compose an assortment of anisotropy-inducing physics. Combined with different geometric arrangements a diverse group of anisotropic problems can be formulated.

4.1.2 Problem Specifications

With the anisotropy-inducing physics described in Section 4.1.1, a set of characterization problems that have different combinations of each of these effects can be conceptualized. These problems provide an overview of how the Ω -methods perform in an assortment of anisotropic problems. As previously described, these fall into two broad categories: anisotropy caused by the problem materials and geometry, and anisotropy caused by the source definition. In the next several paragraphs, the material and geometric configuration of each problem will be described. This will be supplemented with an explanation of which anisotropy-inducing physics are contained in each problem. A summary of which physics are in each problem is provided in Table 4.1.

Labyrinths

The labyrinth problems have isotropic point sources on the left hand side of the problem emitting a Watt spectrum of neutrons approximating the energy spectrum emitted by that of ^{235}U fission. On the right hand side of the problem there is a NaI detector recording the flux. They are composed of a concrete maze with an air channel through the maze, and then open air channels at either end of the channels. The first variant of the labyrinth has a single turn, as illustrated in Figure 4.1, and the second labyrinth has multiple turns, as illustrated in Figure 4.2. These problems are both likely to have ray effects in the air region near the forward source. However, because far more scattering events will be required for a particle to exit the channel in the multi-turn maze, ray effects will likely be less prominent in the air region near the detector of that variant problem than in the single turn maze. Both problems have strong differences in interaction probabilities between the air and the concrete, thus they will have material heterogeneity. Further, because the concrete is composed of several lighter-mass elements, these will also be highly scattering.

Steel beam in Concrete

Figure 4.3 is a variant problem with a steel beam embedded in concrete. A NaI detector is located on the right hand side of the problem to record the response in CADIS problems. The source is a 80x80 centimeter sheet pointed in towards the steel structure in the $+x$ direction emitting 10 MeV neutrons. Because the particles have preferential flow through the steel but do not have long streaming paths, this problem has material heterogeneity and will be highly scattering, but will not have streaming paths in the shielding region. Further, because the source is emitted from a thin plate in $+x$, it is monodirectional. This problem may have some ray effects occurring from backscattering off of the steel and concrete in the left side air region. It may also have ray effects exiting the beam on the right hand side. However, because significantly more scattering will happen in the concrete, the ray effects on the right hand side will be less pronounced than in the air exits of the labyrinths.

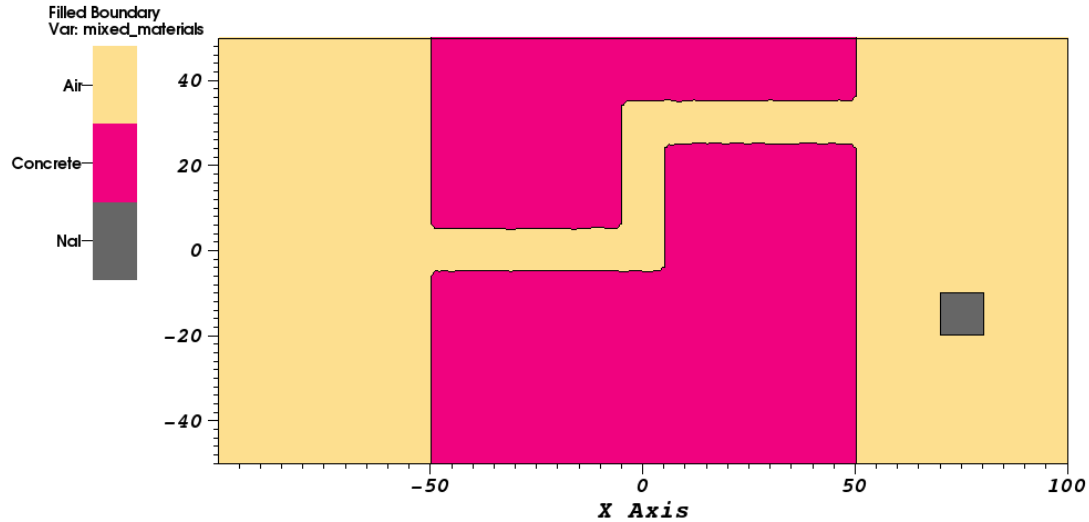


Figure 4.1: Single turn labyrinth geometry.

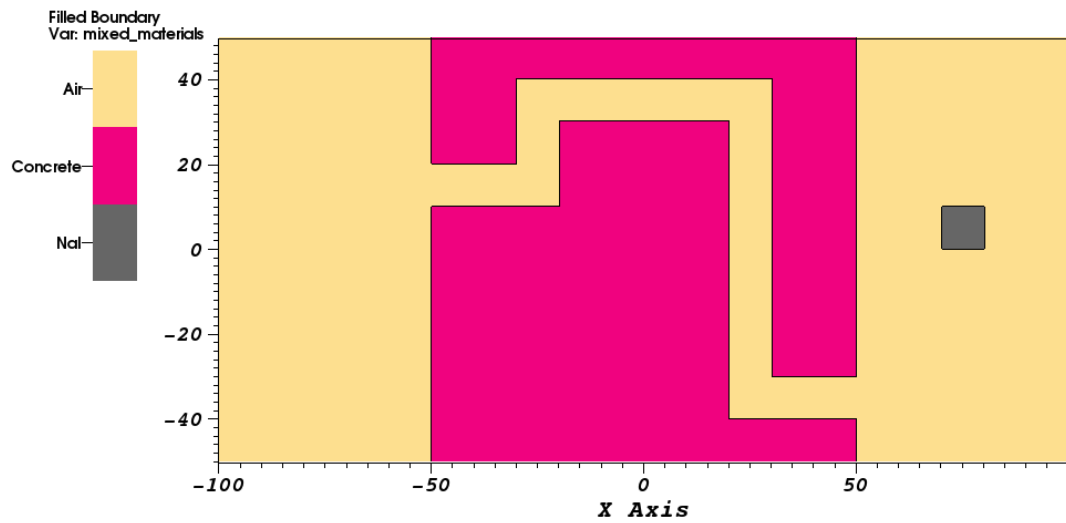


Figure 4.2: Multi-turn labyrinth geometry.

U-shaped corridor

The U-shaped corridor illustrated in Figure 4.4 is somewhat similar to the maze variants from Figs. 4.1 and 4.2. On the left-hand side of the corridor there is a point source emitting

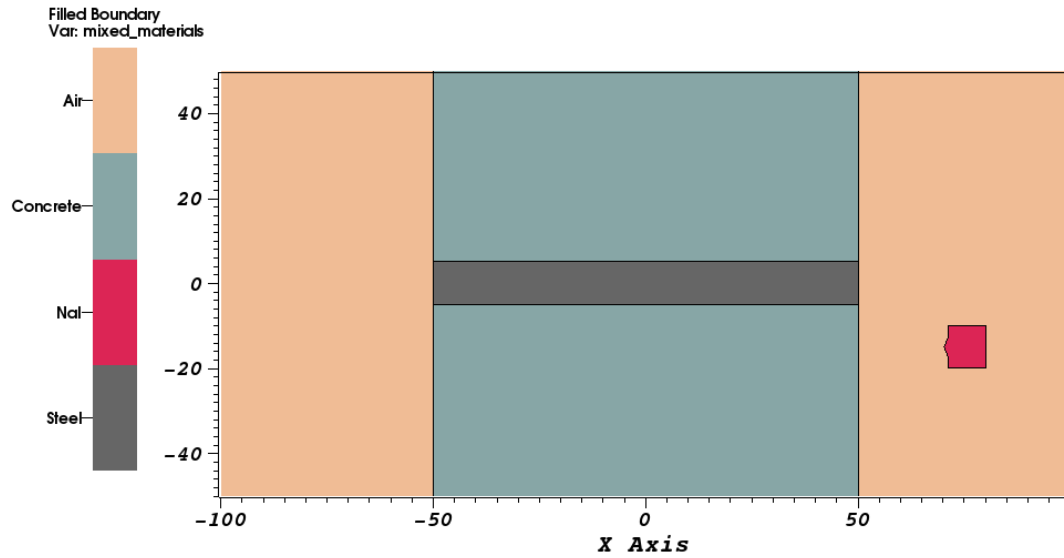


Figure 4.3: Steel plate embedded in concrete.

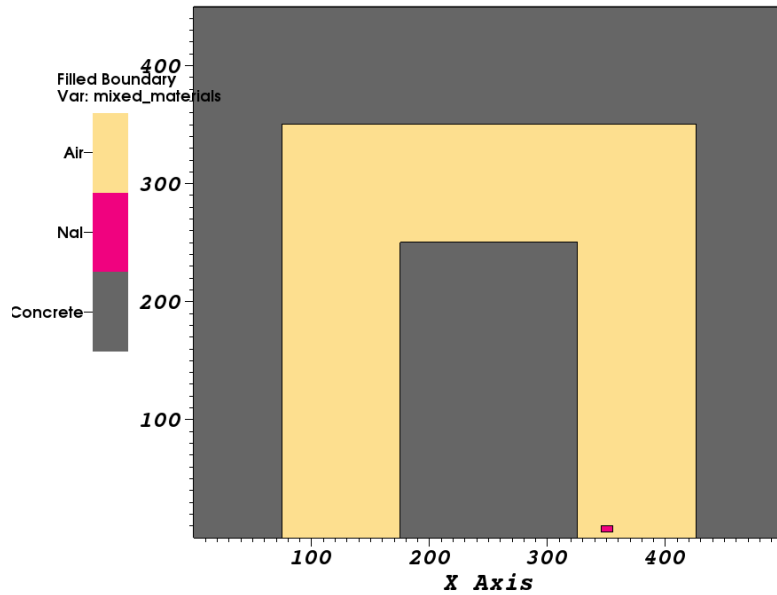
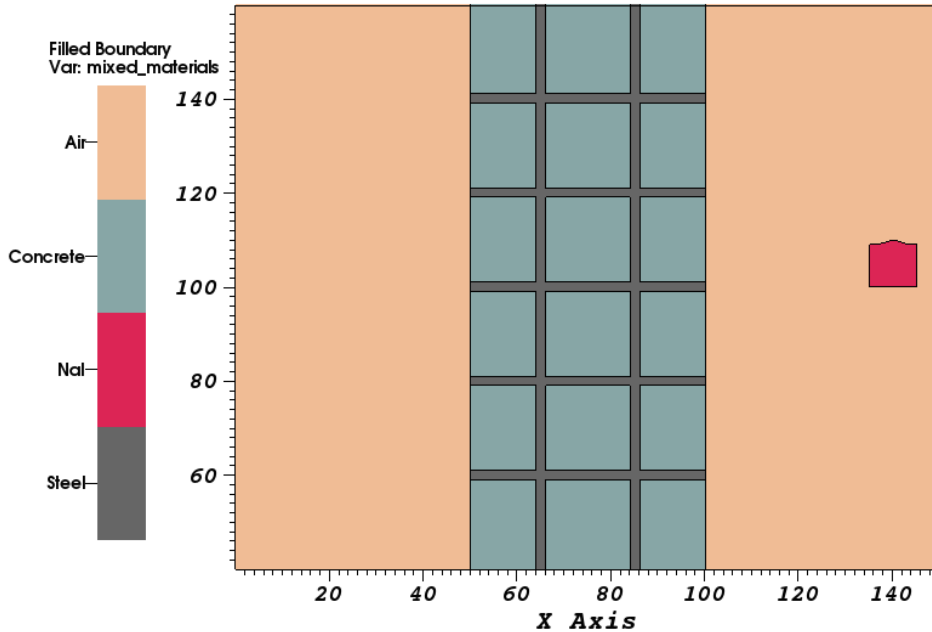


Figure 4.4: U-shaped corridor in concrete.

a Watt spectrum of ^{235}U neutrons. The right leg of the corridor has a NaI detector. Without the large air voids in the labyrinth variants, the U-shaped corridor will have less prominent

ray effects. The heterogeneity between the air and concrete will preferentially transport particles through the air, and particles interacting with the concrete will downscatter in energy.

Concrete shielding with rebar



(a) Slice at $y = 100$ centimeters

The shielding material illustrated in Figure 4.5 is built off of the steel structural beam problem in Figure 4.3. However, this is a more realistic illustration of rebar in concrete. In this problem, a NaI detector is used to measure the response on the right hand side of the problem in yellow. The source is both space- and energy-dependent, emitting a Watt spectrum of neutrons characteristic of ^{235}U fission, and is distributed in a 100x160 centimeter plate on the left hand side of the problem. The source is monodirectional in $+x$. The two images provided show different xy-plane cutaways of the shielding, with steel rebar running through the concrete in different directions. This problem will have angular dependence, but preferential flowpaths through the concrete are not directed towards the detector location on the other side of the shielding in some of the rebar. This problem has material heterogeneity both in the concrete and between the concrete and air. This problem is highly scattering from the concrete, and is unlikely to have ray effects without a strong single preferential flowpath through the shield.

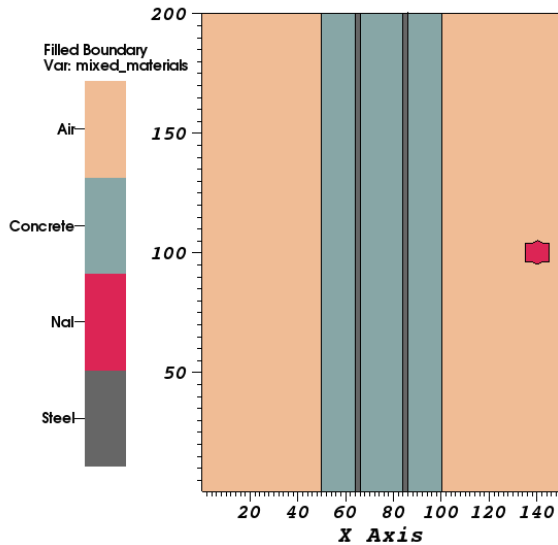
(b) Slice at $z = 105$ centimeters

Figure 4.5: Concrete shielding with rebar.

Nuclear medicine therapy room

A small application problem relevant to the interests of this project is the therapy room illustrated in Figure 4.6. This room has concrete walls, a water-based phantom that is being irradiated by a monodirectional source in the room, and a hallway where a therapy technician might walk. In a CADIS run of this problem, we seek to calculate the response in the technician in the hallway from particles that are not absorbed by the patient in the room. Because this problem is primarily air with concrete borders, it will have strong streaming effects in the air. Particles that do make it to the technician will be produced by emission from the patient in the room, by scattering off air or by scattering off walls. Because of the high fraction of air in this problem, we also anticipate ray effects to occur. While there will be scattering in this problem, it will not be as strong of an effect as other characterization problems.

Now that the broad subset of characterization problems have been described, the physics that each contains is summarized in Table 4.1. The table illustrates that it is difficult to separate one cause of flux anisotropy from another in a characterization problem. This is especially true in generating a problem that has ray effects without streaming paths, and in constructing a highly scattering problem that has preferential flow paths but does not have material heterogeneity. This is a deficiency of the characterization problem construction, and is certainly an area that may be improved upon in future work.

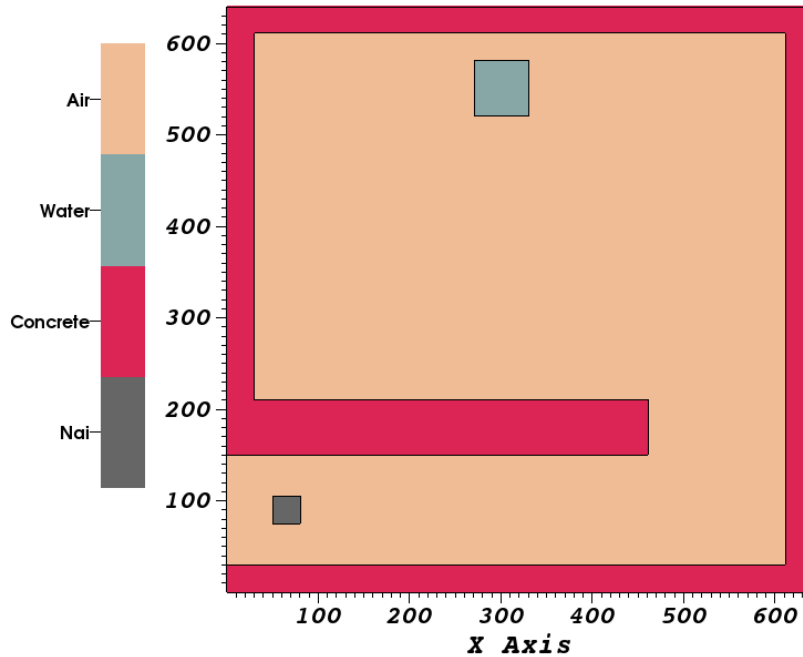


Figure 4.6: Therapy room geometry.

Problem Name	Problem Coverage				
	Streaming Paths	Highly Scattering	Material Heterogeneity	Monodirectional Source	Ray Effects
Single turn labyrinth	x	x	x		x
Multi-turn labyrinth	x	x	x		x
Steel plate		x	x	x	x [†]
U-shaped corridor	x	x	x		
Shielding with rebar		x	x	x	
Therapy Room	x		x	x	x

[†] May have ray effects in low density region exiting the metal plate, but effects will be less pronounced than other problems.

Table 4.1: Anisotropy-inducing physics of each of the characterization problems. Each identified anisotropy-inducing physical metric is used in different combinations for the characterization problems. This will help to aid in extrapolating to which real problems the Ω -methods may be applied.

4.1.3 Introduction to Data Visualization and Analysis

At this point several characterization problems have been identified for their properties in inducing anisotropy in the particle flux. Prior to going through the results for each of the characterization problems, this section shows how the data for each problem is presented and walks through the reasoning behind this approach to the analysis. This starts with example tables and figures of the FOM and tally results. Then, plots explaining the anisotropy metrics follow. This is accompanied by a discussion about how the anisotropy metrics can be related to the FOM and the relative error.

Figure of Merit and Timing Tables

In Section 3.2.2 several equation variants of the FOM were presented as quantifications of method success. The FOMs for each characterization problem are presented in tabular form, similar to Table 4.2. As discussed in that section, the FOM is dependent on the relative error and the time to obtain that relative error. For the hybrid cases, six different FOMs will be presented: three FOMs based on the tally average relative error, the tally maximum relative error, and the tally minimum relative error, and two FOMs based on the Monte Carlo runtime and the hybrid runtime. The unbiased analog Monte Carlo does not have a deterministic runtime, so only the three FOM variants based on the relative error are presented for those runs. When analyzing the results in the FOM table for each characterization problem, consider that the tally average relative error is calculated from all particles contributing to all tally bins in the problem. Thus the FOM reported for the tally average relative error may be outside of the bounds of the tally minimum or the tally maximum relative error. Table 4.2 summarizes which equations were used to calculate each FOM; each equation number is noted in brackets.

FOM Variant	CADIS or CADIS- Ω MC (3.15a)	CADIS or CADIS- Ω MC_{hybrid} (3.15b)	analog MC
tally avg (3.12a)	$FOM_{avg,MC}$	$FOM_{avg,hybrid}$	$FOM_{avg,MC}$
max RE (3.12b)	$FOM_{max,MC}$	$FOM_{max,hybrid}$	$FOM_{min,MC}$
min RE	$FOM_{min,MC}$	$FOM_{min,hybrid}$	$FOM_{min,MC}$
time (mins)	T_{MC}	T_{hybrid} (3.13)	T_{MC}

Table 4.2: Table of FOM variants used to measure Ω performance. Relevant equations can be found in Section 3.2.2 and are referenced in the table in parentheses.

Tables calculating the FOMs summarized in Table 4.2 may not have evaluated FOMS in some locations. These will be noted with a dashed line, or “—”. These values will generally be in the minimum relative error section of the FOM tables, and they represent a zero relative error. This does not mean that infinite particles have been sampled (so the relative error is infinitely small), but rather that no particles have been binned for that energy bin. This

technically results in an infinite FOM, but in reality represents a bin that will never converge. Because this value will hold no meaning in our quantification of the Ω -methods' success, the infinite valued FOM is not included.

Table 4.3 reports the times used to calculate the FOM values in Table 4.2 more detail. This table is split into three vertical regions: the MCNP time spent doing Monte Carlo transport (T_{MC}), the deterministic time spent in ADVANTG/Denovo (T_{det}), and the walltime (T_{hybrid}), which is the summation of the two. The deterministic time section contains further segmentations of timing. This is because processes in ADVANTG are run using different computational resources. ADVANTG itself is a driver script that can launch a parallelized run in Exnihilo/Denovo, but it also postprocesses the Denovo fluxes into source biasing and weight window parameters. The processes exclusive to ADVANTG, like generating the biasing parameters, are performed in serial on a single processor. Conversely, all of the Denovo calculation is run in parallel on any number of cores specified by the user. To ensure that a comparable time is used when calculating the adjusted FOM, we have chosen to calculate the total walltime spent in each calculation. Thus, the parallelized clock time is multiplied by the total number of cores to obtain T_{denovo} . This quantity is summed with the runtimes of the other serial tasks to obtain the total deterministic runtime.

	CADIS time (minutes)	CADIS- Ω time (minutes)	analog time (minutes)
MCNP time	$T_{MC,cad}$	$T_{MC,cad-\Omega}$	$T_{MC,analog}$
deterministic time	0.18	0.18	—
advantg time (T_{adv})			
denovo time (T_{denovo})	5.69	25.64	—
dispose time	0.00	0.16	—
omega time (T_Ω)	—	0.66	—
total (T_{det})	$T_{adv} + T_{denovo}$	$T_{adv} + T_{denovo} + T_\Omega$	—
wall time	$T_{MC,cad} + T_{det,cad}$	$T_{MC,cad-\Omega} + T_{det,cad-\Omega}$	$T_{MC,analog}$
total (T_{hybrid})			

Table 4.3: Table of differing times used to measure Ω performance. These times are used to calculate the FOMS in Table 4.2.

Two other times are listed under the deterministic time that may or may not be included in T_{hybrid} , which are T_Ω and $T_{dispose}$. $T_{dispose}$ is the reported times that are not included in the calculation of T_{det} in either CADIS or CADIS- Ω . It is a sum of time results that either are not important to comparing the methods—like calculating the anisotropy metrics—or times that are accounted for by other tasks in T_{det} . This prevents overlap of times and provides a

more realistic comparison between the performance of both methods.

The reported Ω time, T_Ω , is the total time spent in the tasks unique to the Ω -methods. This includes reading in the angular flux files, performing the computation of Eq. (3.1), and writing the Ω -results to a file. The Ω time, though run in Denovo, is still a serial calculation so is separated out from the total Denovo time. The Ω -method tasks at this time are not parallelized, so the clock time is treated in the same way as the reported ADVANTG time. Because the majority of the Ω -flux generation infrastructure is implemented in Exnihilo rather than ADVANTG, future expansions of the method could be parallelized for faster clock times.

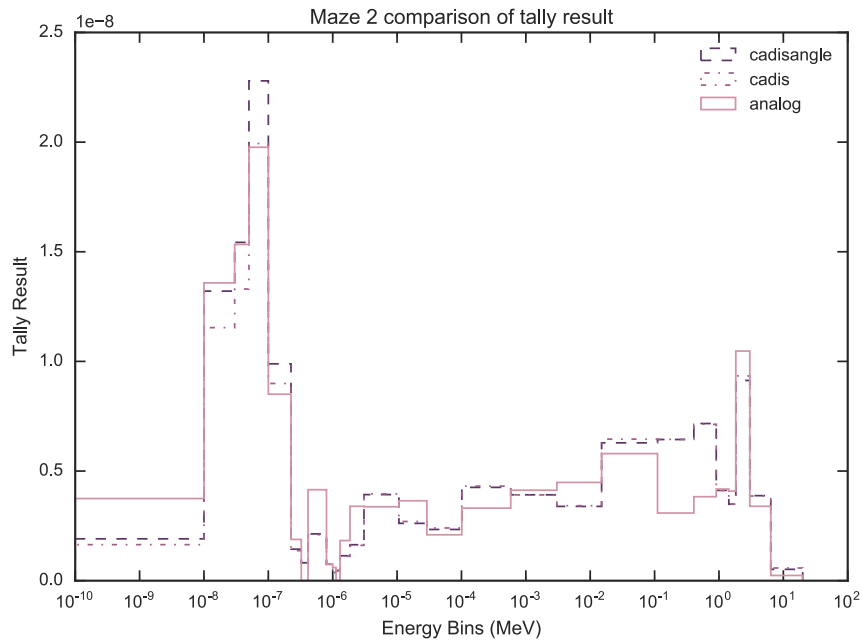
Because the adjusted FOM (the FOMs labeled FOM_{hybrid} in Table 4.2) uses T_{Hybrid} , which is the total runtime of the Monte Carlo calculation (T_{MC}) and the hybrid/deterministic run preceding it (T_{det}), it will differ between the Ω -methods, standard CADIS, and standard FW-CADIS. For CADIS, T_{det} is the sum of the ADVANTG runtime and the wall time of the Denovo transport. For CADIS- Ω , this is the sum of the ADVANTG runtime, the wall time of the Denovo transport, and the time spent in the Ω -flux calculation. How each time is calculated is summarized in Table 4.3.

Beyond adding the Ω -flux compute time, CADIS- Ω will generally have much longer Denovo runtimes than CADIS. This is a combination of the Ω -methods' requirement of both a forward and adjoint calculation (recall that CADIS requires only the adjoint calculation), and that the Ω -methods require full angular flux solutions to calculate the Ω -flux. While standard CADIS has the ability to print the full angular flux solutions as CADIS- Ω , it is neither a requirement nor is it standard practice. The I/O demands to both write the angular fluxes and then read them back in is a potential bottleneck in the method based on the current implementation.

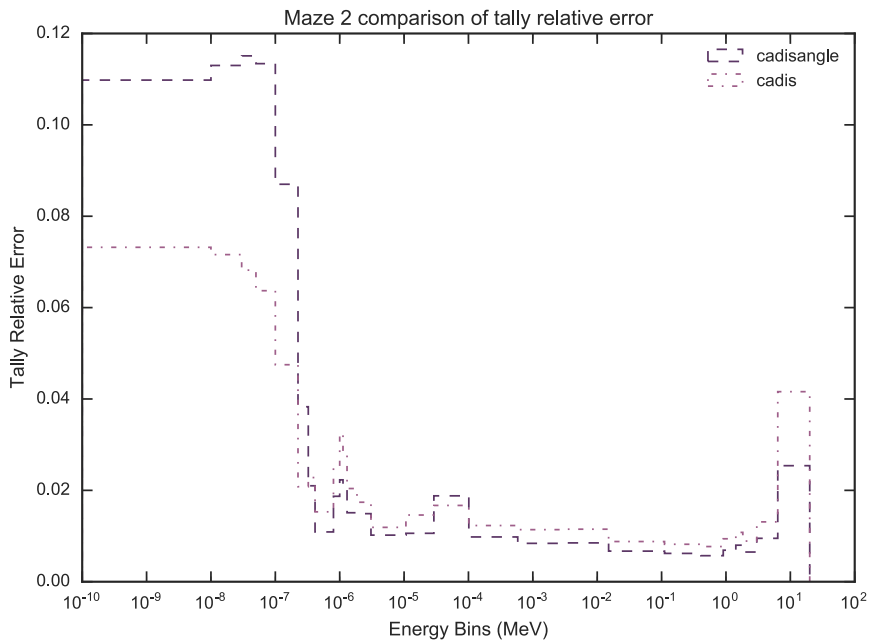
Tally Result and Relative Error Plots

Each of the problems introduced in Section 4.1.2 has a 10x10x10 cm detector in which the tally response is calculated. The tallies are discretized in energy; the tally result and associated relative error are tabulated for each energy bin. Some of this information can be inferred from Table 4.2, but seeing the distribution of the relative errors for each energy bin for each method is a useful way of seeing how effective each method is at biasing particles all of the tally bins, without time effects. As described in the previous paragraph, CADIS- Ω 's deterministic time will be longer than CADIS', so the FOM_{hybrid} may be lower for the Ω -methods, even if the relative errors are better. Presenting both the relative error distribution and the FOM will provide a clear picture of the performance of the Ω -methods.

The tally results and relative errors for CADIS, CADIS- Ω , and the nonbiased analog Monte Carlo will be presented in figures similar to 4.7a and 4.7b. In the case where the relative error of the nonbiased analog Monte Carlo far exceeds the errors achieved by CADIS and CADIS- Ω , it will be omitted. The example given in Figure 4.7b shows a result where this is the case. The hybrid methods will be marked with a dashed line; the nonbiased analog Monte Carlo will be a solid line.



(a) Comparison between methods of the tally result.



(b) Comparison between methods of the tally relative error.

Figure 4.7: Sample results for a characterization problem tally.

Anisotropy Metrics

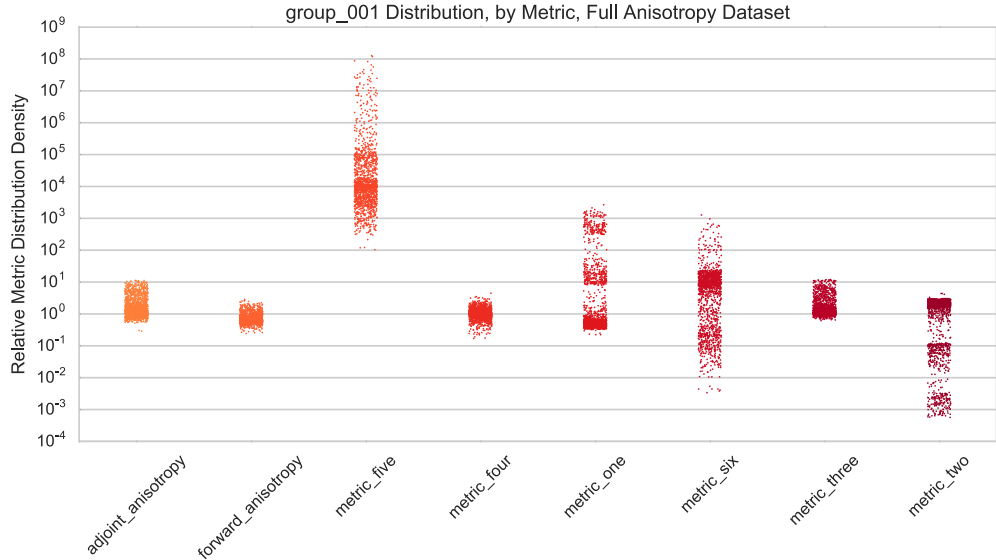
Equations (3.6) through (3.11) in Section 3.2.1 presented several different ways by which the anisotropy of each problem could be quantified. As discussed in that section, Each metric will show slightly differing effects. For example, the ratio of the Ω - to adjoint-flux in metric two will differ significantly from the angular contributon max to average of metric three. The Ω -flux may be larger or smaller than the adjoint scalar flux depending on the directionality of the adjoint and forward particles relative to one another. If the particles are travelling in opposite directions, this will result in a larger omega flux than the adjoint flux. If they stream in the same direction (away from the tally detector, for example), then the resultant Ω flux will be smaller than the adjoint. In the case of the angular contributon max to average the distribution will have a lower limit where the maximum is very close to the average contributon flux. It can never be lower than the average. In a isotropic problem, the majority of the cells in the problem will be this ratio, whereas in a strongly anisotropic problem this distribution will shift upwards, but will still have the same limiting lower value as the isotropic case.

To illustrate the effect of how different the anisotropy metrics' distributions are, Figure 4.8 shows stripplots for all of the anisotropy metrics for three different energy groups in one of the characterization problems. The effects of thermalization—and consequently more induced isotropy—on each of the metrics can be seen clearly as one scans from Fig 4.8a to 4.8c.

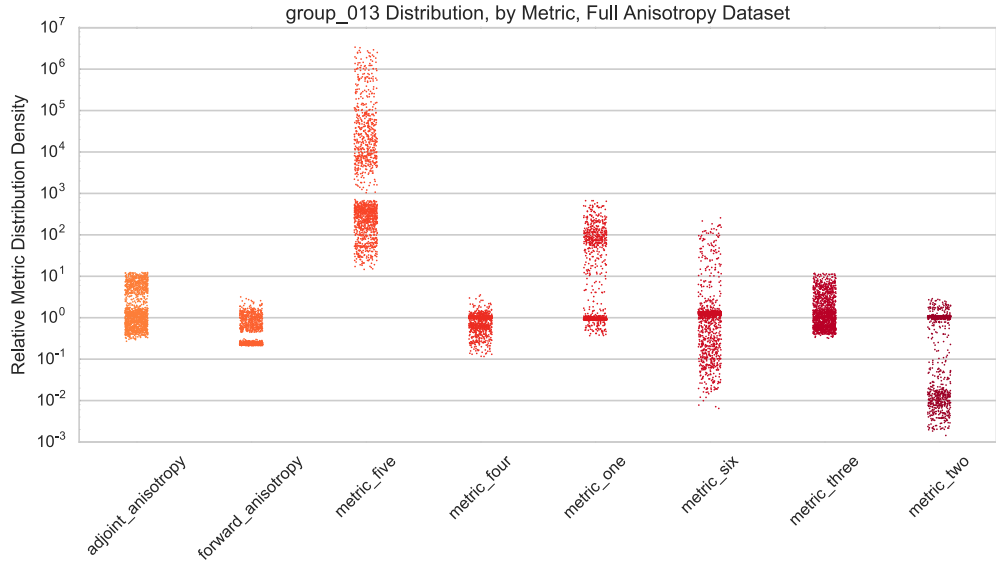
The adjoint anisotropy metric, the forward anisotropy metric, and metric three are all shifted by a factor of 4π . Their natural lowest limit should be near unity but all lie lower. This may be corrected in the future, but for the purposes of this analysis we are more interested in the relative distribution and the consistent factor of 4π is not important to that effect.

A stripplot shows distinct data points, but easily can be overwhelmed if the full number of cells is used in a single strip. The figures in 4.8 contain a random selection of 1500 data points from the full anisotropy datasets, which is only a small fraction of the number of cells in the characterization problem meshes. There are other ways to visualize the full distribution of the dataset. Figure 4.9 shows three modes by which an anisotropy metric can be visualized. These plots, unlike Figure 4.8, show a single metric but all energy groups. The highest/fastest energy group is plotted in deep red, and the lowest or most thermal energy group is shown in blue.

All three subfigures in 4.9 show the effects of thermalization on the chosen metric distribution and density. The stripplot of 4.9a is a clear representation of the density, but not much more can be ascertained about the distribution of the metric. Figure 4.9b has box and whisker plots that show the data quartiles, the mean, and outliers. However, in the case where the distribution is heavily towards a limiting value, the mean is hard to separate from the distribution. Further, no data on how the metric is distributed beyond the quartile markers is provided. The violin plot of Figure 4.9c is a hybrid of the former two plots. The width of the violin is related to the density of values, but inside the violin the limits of the



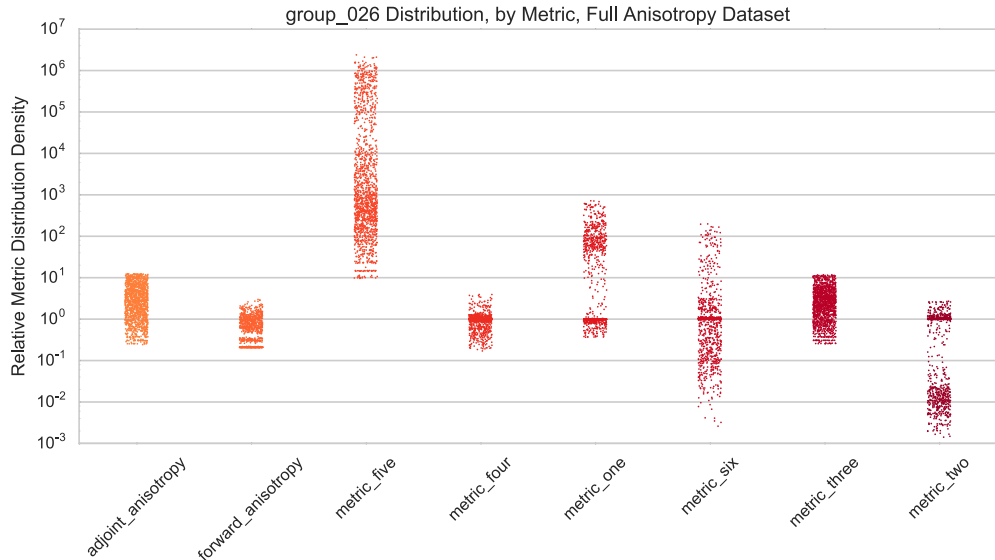
(a) Example distribution of anisotropy metrics for fastest energy group.



(b) Example distribution of anisotropy metrics for epithermal energy group.

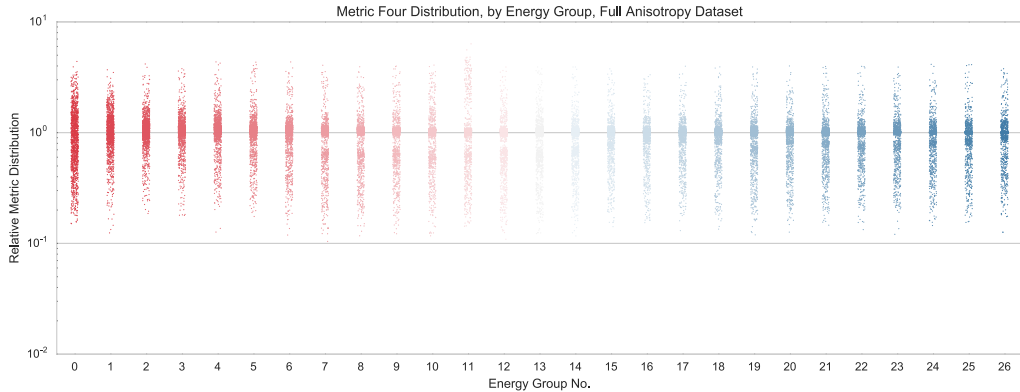
box plots are marked in black. The violin limits extend to the outliers.

The analysis for each of the characterization problems look at the result for the tally average relative error, the tally maximum relative error, and the tally minimum relative error. Because we are interested in how the relative error in each energy bin changes with respect to CADIS- Ω and CADIS, the plots showing the distributions over all energy groups for a single metric is generally more applicable than the plots for a single energy group but with all metrics. As a result, future plots of the metrics will be in the style of those in Figure



(c) Example distribution of anisotropy metrics for thermal energy group.

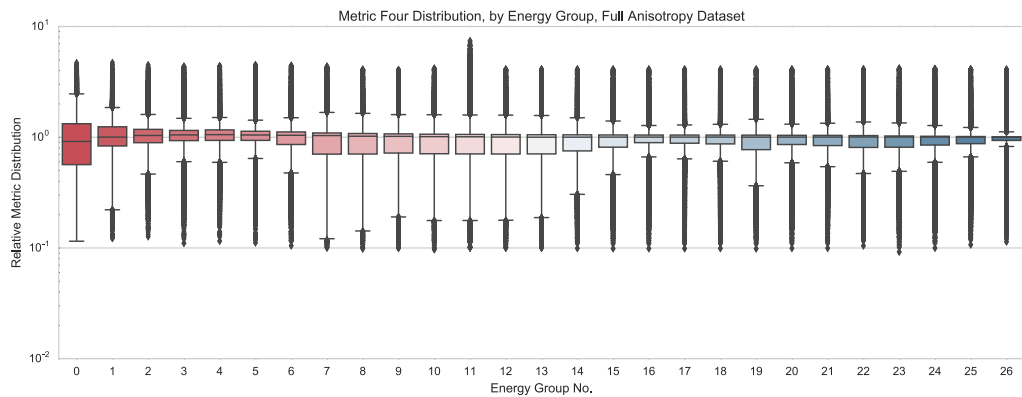
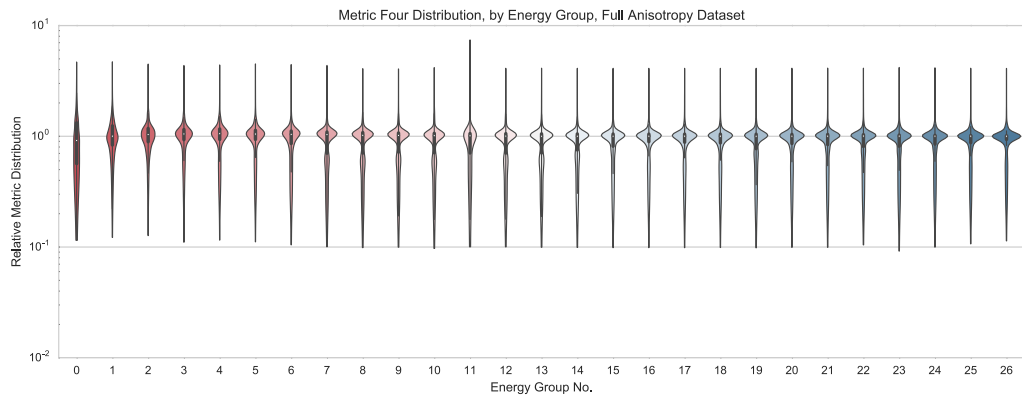
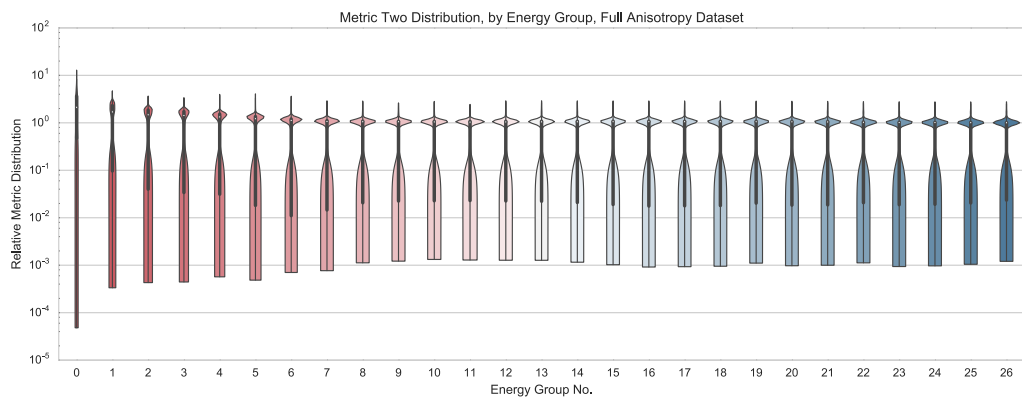
Figure 4.8: Example distribution of all anisotropy metrics for highest, intermediate, and lowest energy groups.

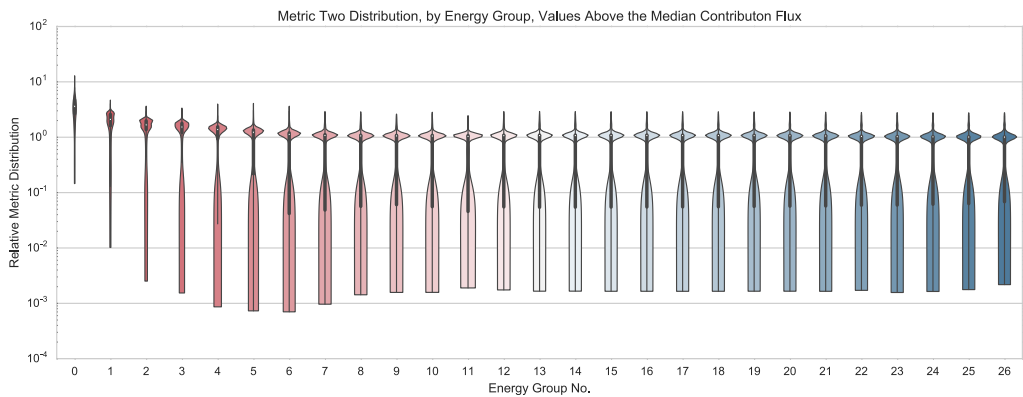
(a) Example distribution of M_4 , all energy groups, strip plot.

4.9 rather than 4.8.

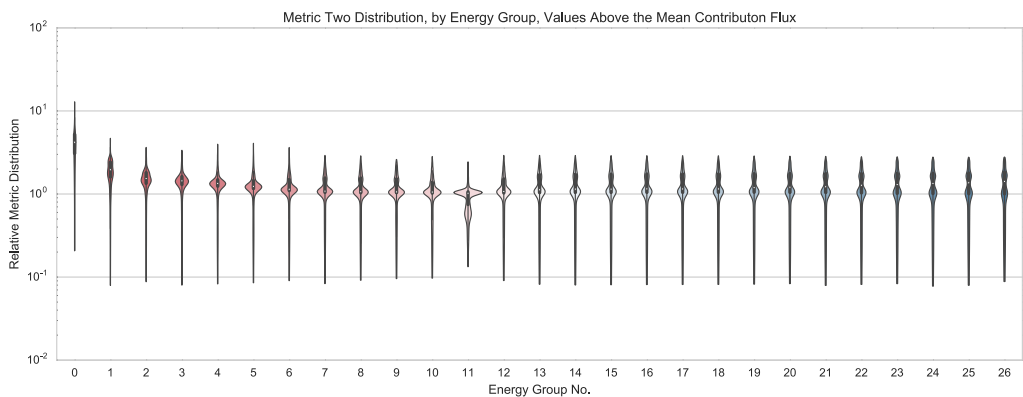
Filtered Anisotropy Metrics

Beyond plotting the anisotropy metrics as a function of energy group, we are interested in how the relative error or FOM will respond as a function of each metric. However, not all cells in the problem are as important as others to contributing to the tally. A cell on the problem boundary is very unlikely to contribute to the tally result when compared to a cell

(b) Example distribution of M_4 , all energy groups, box plot.(c) Example distribution of M_4 , all energy groups, violin plot.Figure 4.9: Different ways of visualizing M_4 for a characterization problem.(a) Example distribution of M_2 , all energy groups, violin plot



(b) Example distribution of M_2 , all energy groups, violin plot using only datapoints above the median metric value in each energy group.



(c) Example distribution of M_2 , all energy groups, violin plot using only datapoints above the mean metric value in each energy group.

Figure 4.10: M_2 violin plots using different selections of the metric data.

next to the adjoint source. As discussed in Section 2.2.3, the contribution flux measures the response importance of a cell. By selectively choosing anisotropy metrics from cells that are likely to induce a response, some of the noise of less important cells can be cut out.

To consistently cut out the same number of datapoints across all metrics, we have chosen to use a filtering algorithm based on the contribution flux in each cell. The first filter is choosing metric values from cells where the contribution flux is above the problem median contribution flux. This median is evaluated separately for each energy group to ensure that the same number of cells in each group is plotted. The second filter is choosing metric values from cells where the contribution flux is above the problem mean contribution flux. Again, the mean is computed separately for each energy group such that energy groups with higher contribution fluxes do not cut out important flux values from a different energy group.

However, unlike the median filter a different number of cells for each energy group will be filtered. This is dependent on the skew between the contribution mean and median value for each energy group. Because the filter is evaluated based on the contribution flux, it can be applied to each metric consistently, meaning that the same number of cells are filtered out between different metrics.

Figure 4.10 shows the effects of cutting out data from unimportant cells on the M_2 distribution. The first figure in the series, 4.10a, is the M_2 full distribution. As discussed previously, M_2 will be above unity in cells where the forward and adjoint angular fluxes travel in opposing directions, and will be below unity in cells where they travel in the same direction. Very unimportant cells should be below unity. Applying the first filter-selecting values above the contribution median—to this distribution results in Figure 4.10b. The bottom tails of all of the distributions have been shortened, but still many unimportant cells remain. This should be expected, as only half of cells have been removed. Applying the second filter results in Figure 4.10c. The unimportant tails have been almost completely removed from the M_2 distributions. Further, features in the metric distribution once obscured by the tails are now visible.

Improvement Factor Correlations with Anisotropy

Now that a way of visualizing the metric distributions has been presented, we seek to find how the metric distributions relate to the relative error or FOM for a given problem. First, an improvement ratio for the relative error and FOM will be defined. For the relative error it is

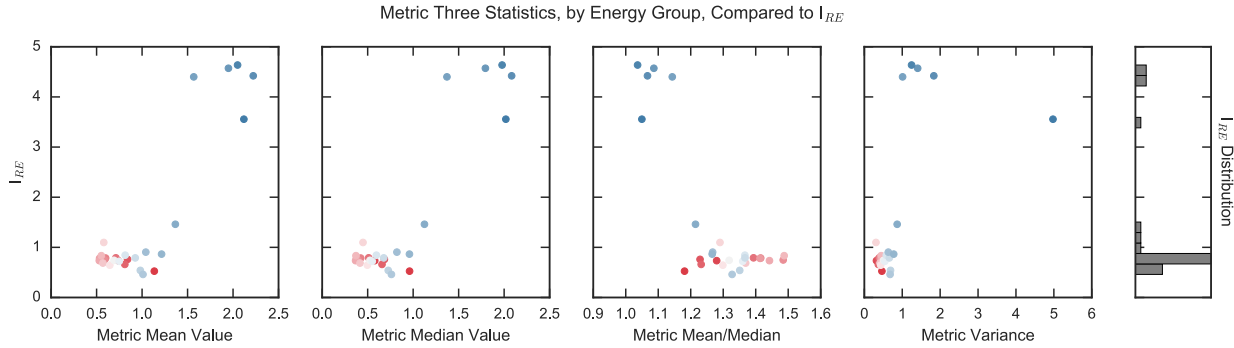
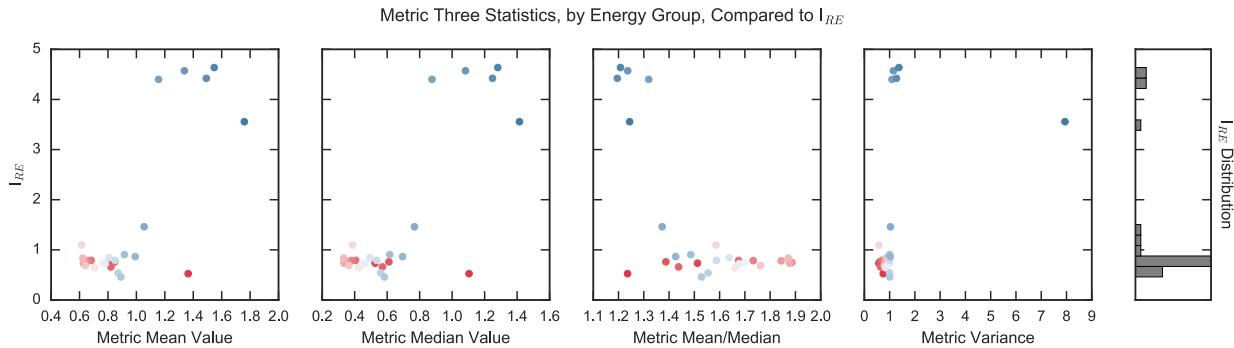
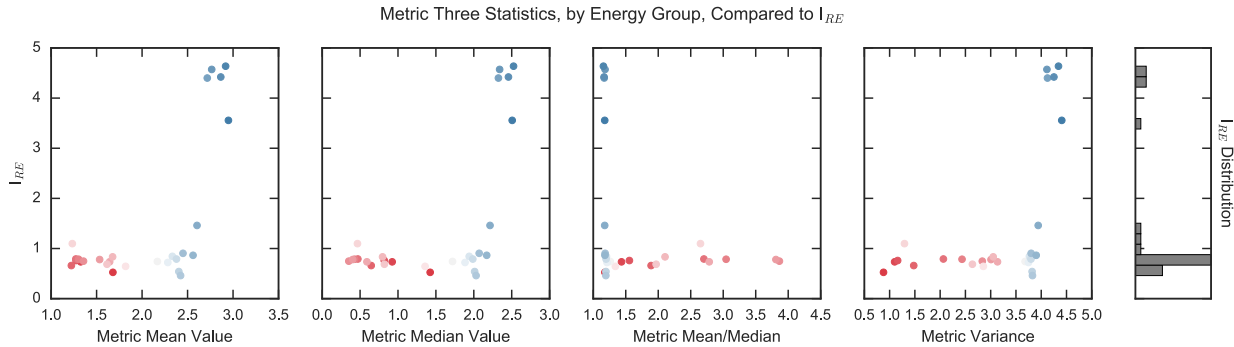
$$I_{RE} = \left. \frac{RE_{CADIS-\Omega}}{RE_{CADIS}} \right|_{E_g}, \quad (4.1)$$

and for the FOM it is

$$I_{FOM} = \left. \frac{FOM_{CADIS-\Omega}}{FOM_{CADIS}} \right|_{E_g}. \quad (4.2)$$

These will be henceforth be referred to as the relative error and FOM improvement factors. With this definition of the improvement in the FOM or the relative error from CADIS to CADIS- Ω , we now have a comparison between the updated and standard methods. By relating this metric to the anisotropy metrics, we can see how anisotropy of the problem influences the improvement in the relative error or the FOM.

There are several ways in which the improvement factor I_{RE} or I_{FOM} may be compared against the anisotropy metrics. The first are against the metric mean and median values. A plot of I versus either of these values should look very similar, with some shifting depending on the distribution. However, if the mean and median are shifted significantly, this would indicate a skew of the distribution. This skew may also be correlated with either of the I values. Last, it is possible that the spread of metric values may be correlated with the I factor. Figure 4.11a is an illustration of how I can be plotted with each of these measurements of the metric distribution.

(a) M₃ average, mean, skew, and variance plotted against the relative error improvement I_{RE} (b) M₃ data selection above the metric median for each energy group, value average, mean, skew, and variance plotted against the relative error improvement I_{RE} Figure 4.11: Sample scatterplots of the M₃ distribution against the relative error improvement factor, I_{RE} .

Similar to using the filtering algorithms in Figure 4.10, the data in the statistical trend plots can also be filtered. The subfigures in 4.11 illustrate how filtering out the data by the

contribution flux influences the location of I_{RE} for each energy group. Figure 4.11b calculates the metric mean, median, skew, and variance for each energy group using only metric values in cells above the contribution median. Conversely, Figure 4.11c calculates the metric mean, median, skew, and variance for each energy group using only metric values in cells above the contribution median value.

The dots in each plot correspond to the same energy groups plotted in 4.10. That is, the lowest energy is plotted in blue and the highest in red. Note that this type of plot is possible because the Monte Carlo tally has been discretized to have the same binning as the deterministic code. It would be far more difficult if the energy bin widths of the Monte Carlo tally did not match the deterministic code.

The data that will be presented for each characterization problem can be subdivided into three distinct categories: data primarily obtained by the Monte Carlo calculation, data primarily obtained by the deterministic calculation, and data that is a combination of both. The FOM values using Monte Carlo runtimes, for example, is in the first category. The anisotropy metrics presented in Section 3.2.1 are an example of a deterministic-exclusive dataset. The results presented in Figure 4.11 are a combination of both deterministic and Monte Carlo-influenced results. In studying the Ω methods, we seek to understand how the Ω methods' performance influence the Monte Carlo results. Beyond observing the FOM and relative error distribution obtained in the Monte Carlo, the anisotropy metrics will provide another avenue by which to investigate Ω -method performance.

One may have deduced that the results for the characterization problems and the subsequent angle sensitivity study will be substantive. Only the most pertinent fraction of the available data will be presented with each problem in Sections 4.2 and 4.3. For example, in most cases only a single figure—and perhaps only a single metric—from the three presented in 4.11 will be presented for a particular problem, because only one will show a trend relevant to the Ω -methods' performance. A more extensive set of data and figures is accessible in the public repositories listed in Appendix A.

4.2 Characterization Problem Results

To quantify the Ω -method success for a variety of anisotropy-inducing physics, we will present various forms of the Figure of Merit, as described in Section 3.2. In the preceding subsections, a subset of flux anisotropy-inducing physics have been identified and a subset of problems that contain these physics have been conceived. In this section, the results for CADIS- Ω , CADIS, and nonbiased Monte Carlo will be presented for each of these problems. Explanations on the performance of the Ω methods will accompany the results for each problem. In some cases, variants of problems were run to confirm or refute observations seen in other problems.

4.2.1 Computational Specifications

As noted in a number of the previous sections, hybrid methods require both a deterministic and a Monte Carlo calculation to obtain a problem result. These transport codes require different computational parameters to obtain an answer. For the characterization problems the computational parameters are summarized in Table 4.4; the parameters for the deterministic and Monte Carlo calculations are demarcated in the table.

Parameter Type	Parameter Value
ADVANTG Values	
P_N Order	3
Quadrature Type	Quadruple Range
Quadrature Order	10
Spatial Solver	Step Characteristic
Energy Group Library [†]	27G19N
Boundary Conditions	vacuum
MCNP Values	
Particle Count	$1e7$
Boundary Conditions	vacuum

[†] Parameter type that has no default in ADVANTG.

Table 4.4: Default simulation values for the characterization problems. The values for ADVANTG primarily signify parameters used to run Denovo, with exceptions for calculating biasing parameters, which is done exclusively in ADVANTG. MCNP-specific values are those used for Monte Carlo runs.

The first portion of the table summarizes the values used by ADVANTG. Note that these values all pertain to the Denovo deterministic solver, which is set up by ADVANTG. The parameter types marked with a dagger have no default in ADVANTG. We have chosen to use a relatively coarse 27 group energy group library. Because the characterization problems are meant to identify the method’s performance pertaining to flux anisotropy, and we expect the energy group structure to have less of an effect on anisotropy conditions than other parameters, we opted for a computationally inexpensive energy group mesh for the deterministic solver. Further, this group library was designed for radiation shielding applications, so it applies to the majority of the characterization problems.

The boundary conditions for all of the characterization problems will be vacuum. At this time, ADVANTG does not support reflective or mirror boundary conditions so this is a limitation in application space that we cannot address at this time. The Monte Carlo code we use does support vacuum boundary conditions, but a discrepancy in boundary conditions

between deterministic and Monte Carlo calculations would result in the simulation of a fundamentally different problem.

Unless noted, the values in this subsection of the table are ADVANTG default values. They are a good initial choice for characterization of the method because they are often chosen as the parameters for hybrid methods studies by experienced and inexperienced ADVANTG users. Further, these values are defaults in ADVANTG for their computational stability, such as not having negative valued weights or fluxes, stable convergence, a relatively fast time to a solution, et cetera. Due to the good properties exhibited by the solver options and because users first using the Ω -methods are likely to choose these values, the values in Table 4.4 will be used for the characterization of the Ω -methods.

The latter section of the table summarizes the Monte Carlo code MCNP values for each of the problems. The value of $1e7$ particles as a particle cutoff was chosen because it made the error bins in the majority of the nonbiased Monte Carlo characterization problems less than 100%. In some problems that are extraordinarily difficult for Monte Carlo to solve without biasing, there were tally bins with very high errors. In the following subsections they will be clearly indicated and their results will not be plotted so as to not obfuscate the CADIS and CADIS- Ω results. Time cutoffs were not chosen because we decided to measure how effective the Ω methods were at reducing the variance per particle. Depending on the flux maps generated from CADIS and CADIS- Ω , the time to transport a finite amount of particles may vary. As a result, the reported times from a simulation can tell us whether the method requires more sampling than other methods in addition to how fast it takes to reach a desired relative error.

The responses in the NaI detectors of each of the problems was measured with an MCNP track length tally (f4). The tally was energetically binned to match the dataset of the multigroup dataset provided in ADVANTG, and the entire volume of the detectors were used with no spatial binning. It should be noted that while the tally is energetically binned, Monte Carlo transport is not discretized in space or energy like deterministic transport. In a nonbiased analog Monte Carlo calculation, transport is completely continuous in space, energy, and angle. In a hybrid calculation using VR parameters from a deterministic solution, the VR parameters will be discretized to reflect the solution obtained from the deterministic solver. As a result, the particle's transit throughout the problem will be a combination of sampling both continuous and discretized-energy dependent factors. Consider a particle that goes through a scattering event in shielding material. In this scattering event, the particle samples from a continuous-energy cross section and changes direction based on its energy. However, depending on how much energy it loses in the scattering event it may cross into the energy range of a lower-energy weight window and will require further sampling.

All characterization problems were run on Remus, a machine operated and maintained by the Radiation Transport and Nuclear Systems Division at Oak Ridge National Laboratory. The ADVANTG runs were run on 16 cores of a 32 core node, with 256Gb of memory. The MCNP runs were run on the same machine, with 256Gb of memory but using all 32 cores of the node.

Each problem presented in Section 4.2 will use the values specified in Table 4.4 unless

otherwise noted. Times to transport the Monte Carlo particle quantity varies between methods due to differences in sampling. Monte Carlo and ADVANTG inputs and directions on how to acquire them are provided in Appendix A.3.

4.2.2 Single Turn Labyrinth

The analysis of the characterization problems begins with the single turn labyrinth. The single turn labyrinth FOM results are summarized in Table 4.5, and are illustrated in Figures 4.12 and 4.13. The table has six FOM values for CADIS and CADIS- Ω results, and three FOM values for the analog (nonbiased) Monte Carlo results. The equations to calculate each of these FOMS is summarized in Table 4.2.

	CADIS		CADIS- Ω		analog
	MC	MC _{hybrid}	MC	MC _{hybrid}	MC
tally avg	18.6	14.9	2.36	1.56	17.4
max RE	2.76	2.21	0.481	0.318	0.0857
min RE	249	200	196	130	–
time (mins)	67.7	84.4	157	237	11.7

Table 4.5: Figure of Merit comparison for single turn maze. The relative errors used are the tally average relative error, the tally maximum relative error, and the tally minimum relative error; the times are total walltimes for the Monte Carlo calculation and the sum of the hybrid method software, the deterministic transport time, and the Monte Carlo calculation time.

		CADIS	CADIS- Ω	analog
		time (minutes)		
MCNP time	total	67.71	157.01	11.67
deterministic time	advantg_time	0.26	0.28	–
	denovo_time	16.41	78.19	–
	dispose_time	0.01	0.40	–
	omega_time	0.00	1.61	–
	total	16.67	80.08	–
wall time		84.38	237.09	11.67

Table 4.6: Detailed timing results for single turn maze.

In Table 4.5 the FOM results for CADIS, CADIS- Ω , and nonbiased Monte Carlo for the single turn maze are presented. In all cases, the CADIS FOMs are better than those obtained by CADIS- Ω . The FOMS calculated using the tally average relative error are better in the nonbiased analog Monte Carlo than CADIS- Ω as well. However, this is a

product of two effects: the time for the analog to run the same particle count is far shorter than either CADIS or CADIS- Ω . As a result, to obtain the same FOM, CADIS- Ω needs to have $R_1/R_2 = \sqrt{T_2/T_1}$ (this is from taking a ratio of the FOMs) the tally average relative error, or 0.27. Because this problem is highly scattering and many low-energy particles can make it through the concrete labyrinth, even the analog can have good sampling at low energies, resulting in a tally average FOM that reaches this threshold.

Table 4.6 contains more detailed timing information spent in each of the codes for each type of problem. We can see that the Monte Carlo runtime for CADIS- Ω is more than twice that of CADIS, and almost fifteen times that of the nonbiased analog Monte Carlo. The time to run just the hybrid/deterministic portion of the calculation is also four times longer for CADIS- Ω than it is for CADIS. These disparities in runtimes have a strong negative impact on the CADIS- Ω FOMs, which was observed in the FOM results in Table 4.5.

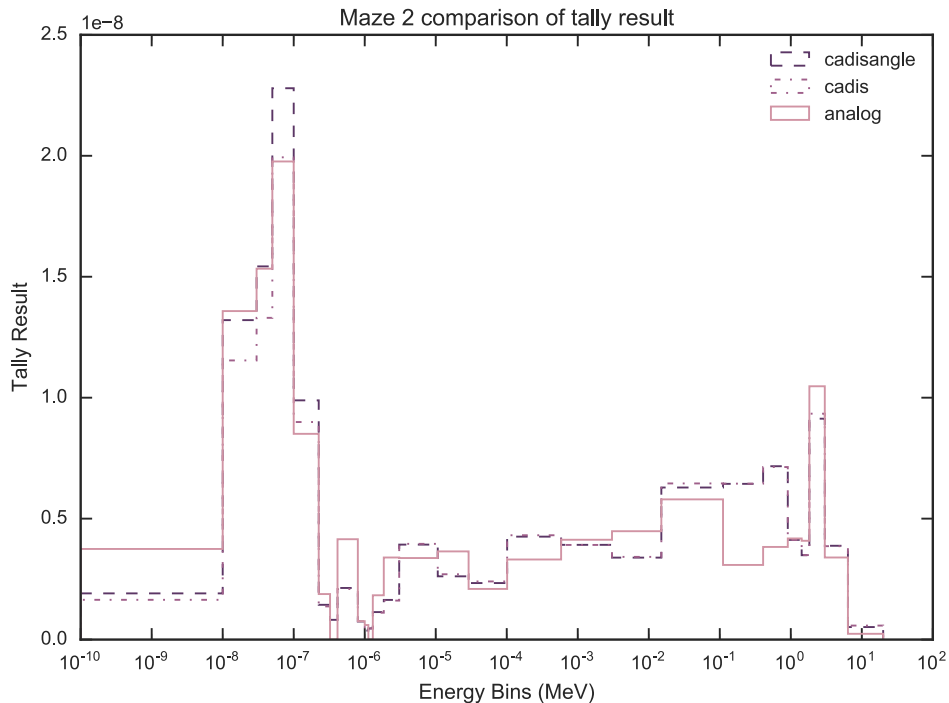


Figure 4.12: Tally results comparison between methods for single turn labyrinth.

Figures 4.12 and 4.13 show the tally result and the relative errors for each result in the single turn maze, respectively. This particular relative error plot, Figure 4.13, does not include the relative error bins of the analog result because they are significantly higher than the CADIS and CADIS- Ω results. This is further confirmed in Table 4.5, where the minimum relative error FOM is a non-tallied bin.

By inspecting Figure 4.12, one can observe that the CADIS and CADIS- Ω results are in agreement in bins greater than 10^{-7} MeV. At lower energy bins, CADIS- Ω generally

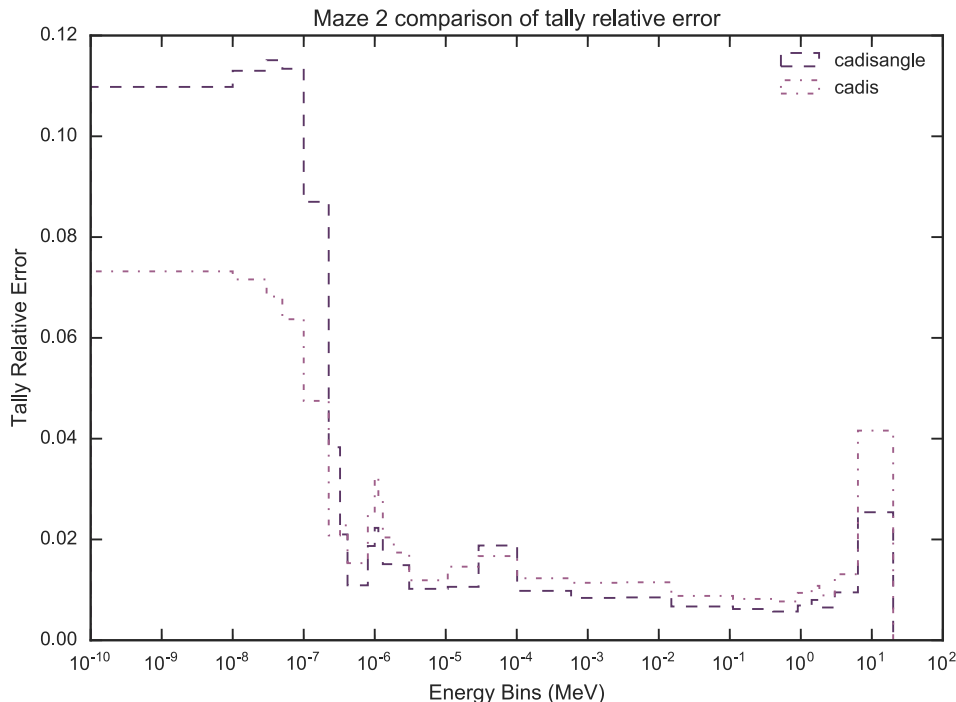
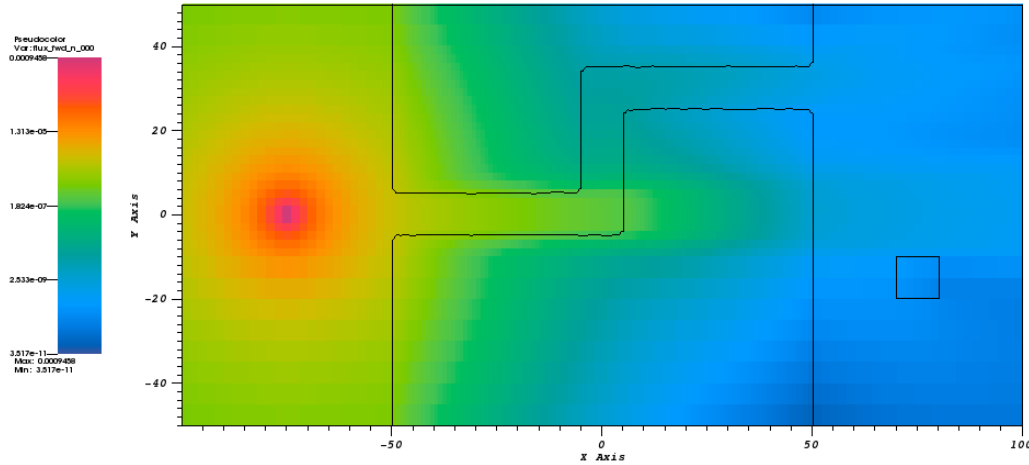


Figure 4.13: Tally relative error comparison between methods for a single turn labyrinth.

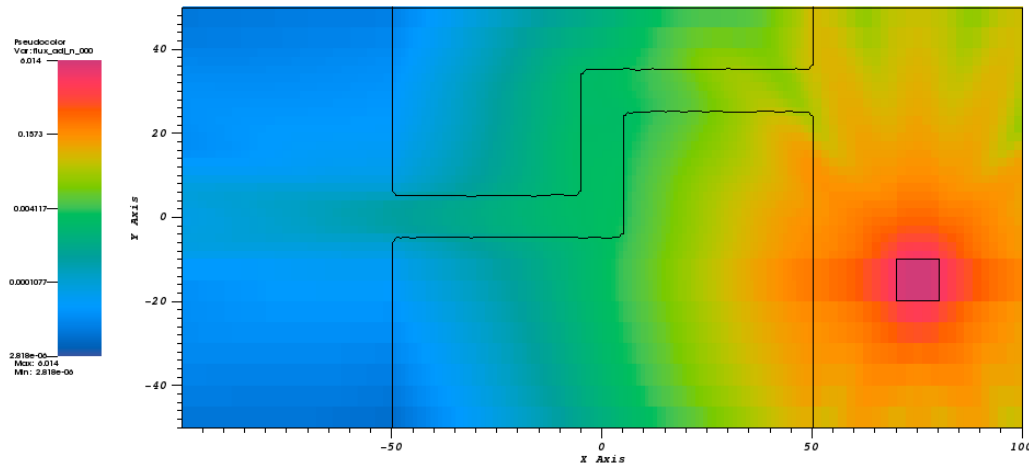
has a higher value for the tally result than standard CADIS. However, in comparing the errors for these low energy bins in Figure 4.13, CADIS has a lower relative error. This indicates that CADIS sampled many more low-weight particles than CADIS- Ω in these regions. Conversely, CADIS- Ω has a lower calculated relative error than CADIS for bins greater than $5 * 10^{-6}$ MeV. This is expected, as higher energy particles generally exhibit a stronger angular dependence than low-energy particles. In geometric and energetic regions where the angular dependence is stronger, the importance map generated by CADIS- Ω may show more of an effect in improving the relative error.

To aid in our understanding of how the Ω -method's importance map differs from the standard adjoint flux map, let us compare the flux distributions obtained by different deterministic solutions of the single turn labyrinth. Figure 4.14 shows several different flux distributions that represent the single turn labyrinth geometry. This figure is of the highest energy group for each flux type.

Figure 4.14a shows the forward flux for the labyrinth. It is clear that in this problem, particles emanate isotropically outwards from the source on the left side of the problem. Some particles travel towards the shield and enter the labyrinth. These particles travel 50cm and hit the wall in the first turn of the labyrinth. Many high energy particles reach fairly deep into the concrete past this turn, as indicated by the green channel partway through the concrete.

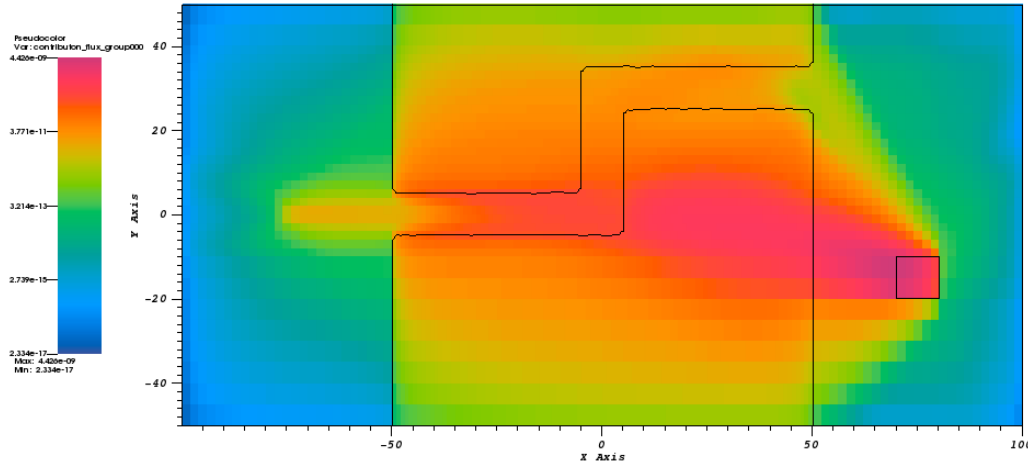


(a) Forward flux map for highest energy group, single turn labyrinth.



(b) Adjoint flux map for highest energy group, single turn labyrinth.

Figure 4.14b complements Figure 4.14a by showing the adjoint flux distribution for the fastest energy group. Recall that this distribution is what is used by CADIS to generate VR parameters. Particles are generated throughout the NaI detector and exit the detector

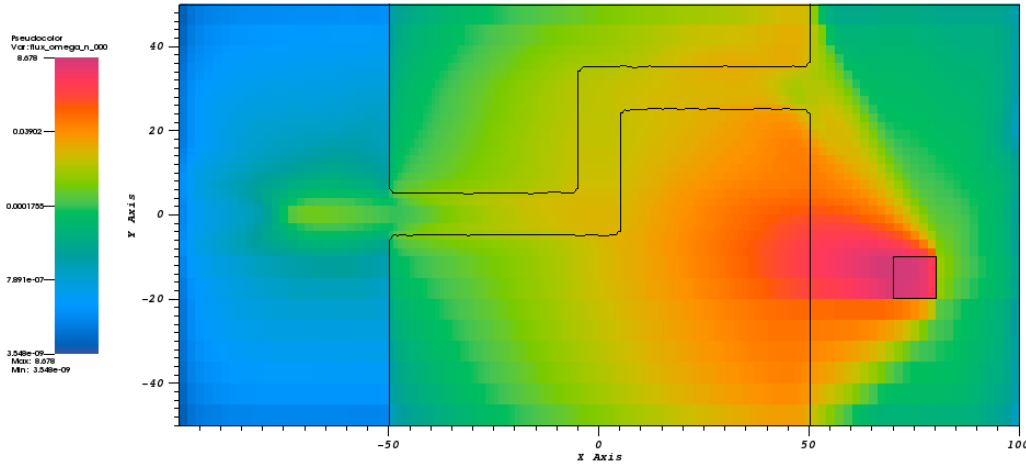


(c) Contribution flux map for highest energy group, single turn labyrinth.

in all directions. Because the source is not in line with the labyrinth entrance, particles end up colliding much closer to the labyrinth edge than in the forward distribution. There also exist some prominent ray effects in this distribution on the right hand side of the problem. In particular, the contrasting orange and green fingers of the ray effects show at least an order of magnitude change in the flux for forward particles exiting the maze in this region. In reality, the importance in this region should be close to a spherical surface some distance away from the adjoint source.

Recall that the Ω -flux is computed using the angle-integrated contribution flux in the numerator. For this problem, the contribution flux will be used to illustrate how the Ω -flux is a combination of the adjoint and the contribution flux. Figure 4.14c shows the distribution of angle-integrated contribution flux values for the single turn labyrinth. Interestingly, because so many forward particles penetrated deeply into the shield, the contribution flux points directly into this section of the shield. It is also clear that near the forward source, only particles moving in the direction towards the labyrinth entrance contribute to a high contribution flux. In the left-side of the labyrinth, we can observe directional importance in the labyrinth channels, but in the first turn this directional importance is no different than the concrete barriers surrounding the channels.

Figure 4.14d shows how the Ω -flux is built off of the adjoint and contribution fluxes by showing the Ω -flux distribution for the single turn labyrinth. Comparing this figure to 4.14c, the majority of high flux regions are pushed back towards the NaI detector. The flux gradient exiting the maze does not span as many orders of magnitude as it did in the contribution flux plot, too. Further, the importance of particles does not remain as high or



(d) Ω -flux flux map for highest energy group, single turn labyrinth.

Figure 4.14: Flux map slice of single turn labyrinth. Flux maps have scales normalized to maximum and minimum values for each slice; between plots the scales are not consistent. These plots show the highest energy group, group 000, for each cell in the problem midplane.

go as deep into the concrete shield as the contributon flux plot. This is because the Ω flux normalizes by the forward flux, resulting in reducing importance in regions where only the forward flux is strong. As with the contributon flux, the Ω -flux strongly reduces particle importance near the problem boundaries. Recall from Section 2.2.3 that in the contributon transport equation that the cross section becomes very high near problem boundaries, thus encouraging particles back towards the problem source and sink. Because the Ω -flux uses standard forward and adjoint transport, the cross section is not manipulated. However, the flux magnitude reflects importance consistent with contributon theory.

Both the Ω - and the contributon fluxes show a mitigation of ray effects on the right hand side of the problem. Note that there are no “fingers” of flux magnitude at distances several cm away from the NaI detector on the right side of the problem in either Figure 4.14c or 4.14d. Reducing these numerical apparitions is a positive effect of the method. However, there exists a fairly strong gradient in flux magnitude for a particle travelling directly out of the maze exit. As a result, a particle traveling several cm of distance across this strong gradient line may move from a region of very low importance to very high importance, causing very significant sampling requirements for the Ω -importance that may not exist with the standard adjoint.

A description of filtering algorithms accompanied the discussion of the anisotropy metrics

in Section 4.1.3. The filtering algorithms are based on the contributon flux distribution in the problem, or 4.14c. Recall that the two filter matrices discussed included those from cells where the contributon flux is above the average contributon flux value, and where values are above the mean contributon flux value. For the single-turn labyrinth, the filter matrix in the highest energy group (Figure 4.14c) will use values in the orange and pink region of the figure and exclude values from the blue and green regions of the figure. As a result, only anisotropy metric values from within the maze will be used. The very anisotropic values near the edge of the problem (where significant particle streaming exists), will not be included because they are likely to be inconsequential to the tally response.

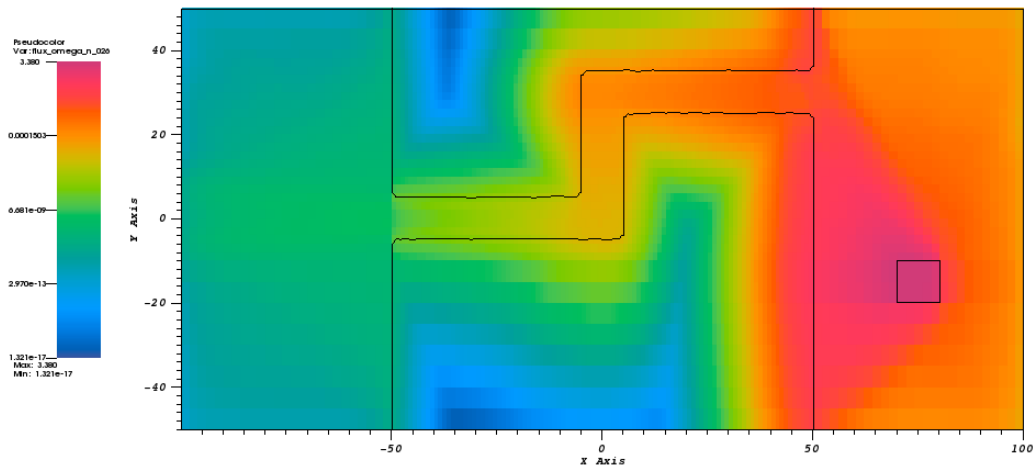


Figure 4.15: Ω -flux flux map for lowest energy group, single turn labyrinth.

Figure 4.15 shows the Ω -flux distribution for the lowest energy group. This differs quite a bit from 4.14d in that the flux in the labyrinth has a much stronger gradient once entering concrete than the higher energy group. This is expected, as the mean free path of a low energy neutron is much shorter than a high energy one, especially in a dense, hydrogenous material like concrete. As a result of the stronger flux gradient in concrete, low energy particles entering the concrete shield will be rouleotted at a much greater frequency than high energy particles. Particles exiting the labyrinth also have a lower gradient of importance than they may cross than in the high energy flux map. As a result, particle splitting and rouleetting in this air region will be less extreme at low energies than at high energies.

Comparing the figures of Ω -fluxes in 4.14d and 4.15, we can start to explain some of the timing behavior observed in Tables 4.5 and 4.6. High energy particles exiting the maze towards the tally detector have much longer mean free paths than the low energy particles,

and will generally show a much stronger effect in the Ω -flux in those regions. This is illustrated in Figure 4.14d. The shape of the Ω flux around the detector region is much more strongly dependent on direction in the high energy group 000 flux than it is for the lower energy group 026 flux. Despite having lower relative errors than CADIS at higher energies, CADIS- Ω has lower FOMs than CADIS for the FOMS calculated with the minimum relative error. As discussed previously, this is due to the long runtime of CADIS- Ω , which is more than twice as long as CADIS. From this, we can conclude that while CADIS- Ω is better at transporting particles in high energy regions than CADIS, achieving lower relative errors, the length of time to do so is prohibitive and achievable by CADIS should the runtimes be the same for both.

4.2.3 Multiple Turn Labyrinth

The multiple turn labyrinth is built off of the single turn labyrinth geometry. The labyrinth materials are much the same, but the geometry differs. Table 4.7 summarizes the Figure of Merit results for CADIS, CADIS- Ω and nonbiased Monte Carlo. Figures 4.16 and 4.17 show the results obtained by the track length tally in each method.

	CADIS		CADIS- Ω		analog
	MC	MC _{hybrid}	MC	MC _{hybrid}	MC
tally avg	327	248	224	71	0.054
max RE	1.46	1.11	1.02	0.322	0.0393
min RE	113	85.6	71	22.5	–
time (mins)	51.5	68	35.5	112	25.5

Table 4.7: Figure of Merit comparison for multiple turn maze.

		CADIS	CADIS- Ω	analog
		time (minutes)		
MCNP time	total	51.52	35.55	25.46
deterministic time	advantg_time	0.25	0.21	–
	denovo_time	16.28	74.85	–
	dispose_time	0.01	0.40	–
	omega_time	0.00	1.74	–
	total	16.53	76.80	–
wall time		68.05	112.35	25.46

Table 4.8: Detailed timing results for multiple turn maze.

In Tables 4.7 and 4.8 it is notable that the CADIS- Ω runtime is shorter in the Monte Carlo simulation than CADIS. This differs most of the other cases presented in this section.

However, it is also notable that because the deterministic time is so much longer for CADIS- Ω , T_{hybrid} ends up being greater for CADIS- Ω than CADIS.

Table 4.7 shows that both CADIS and CADIS- Ω outperform the analog by a factor of 10^2 or 10^3 , indicating the necessity of variance reduction for a problem like this. In comparing the FOMs, CADIS slightly outperforms CADIS- Ω for all relative errors, meaning that the time to reach any relative error will be achieved faster by CADIS.

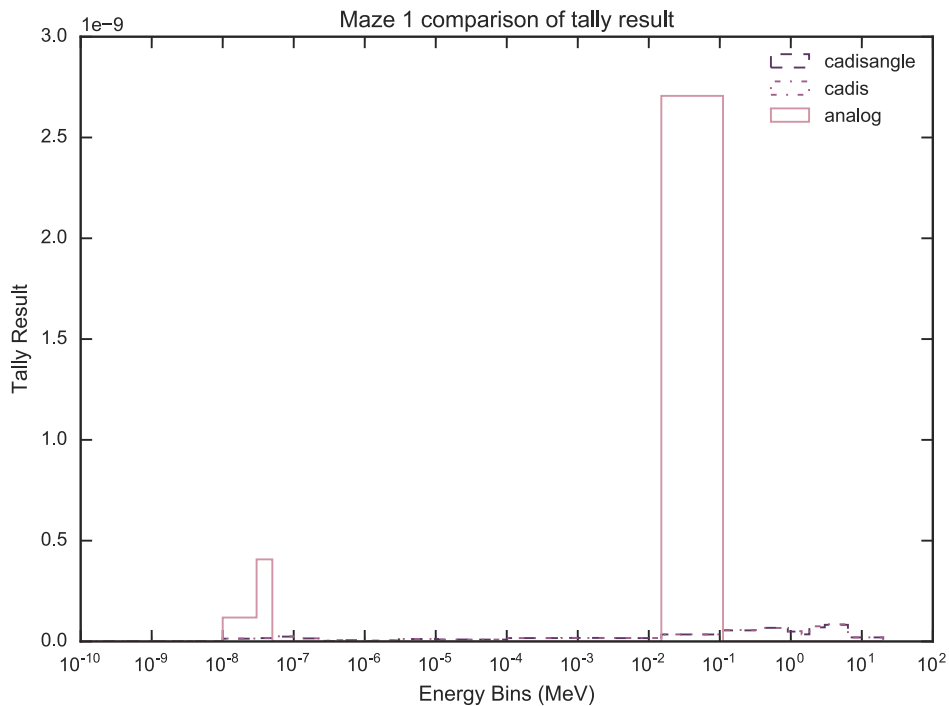


Figure 4.16: Tally results comparison between methods for multiple turn labyrinth.

Looking at Figures 4.16 and 4.17, we can see that the analog Monte Carlo results differ significantly from either CADIS or CADIS- Ω . Two distinct regions of tally bins have been recorded in the analog case: a high energy region comprised of particles that have scattered very few times before reaching the detector, and a much smaller low energy region, comprised of particles that are very thermal. These thermal particles have a very small mean free path in the concrete labyrinth, thus the majority of them were absorbed in the shield. However, given the errors on this result, these results are not trustworthy. In the case of this problem, some of what was discussed in the single-turn labyrinth is confirmed. This particular case requires that particles scatter several more times if they are to exit the labyrinth from the air duct. As a result, the spectrum is more thermal than the first case and the problem has less anisotropy from the scattering effects. As discussed in the single-turn labyrinth subsection, CADIS outperformed CADIS- Ω in problems in energy bins that had less angular dependence. Because this problem has far more scattering event, it overall has less angular

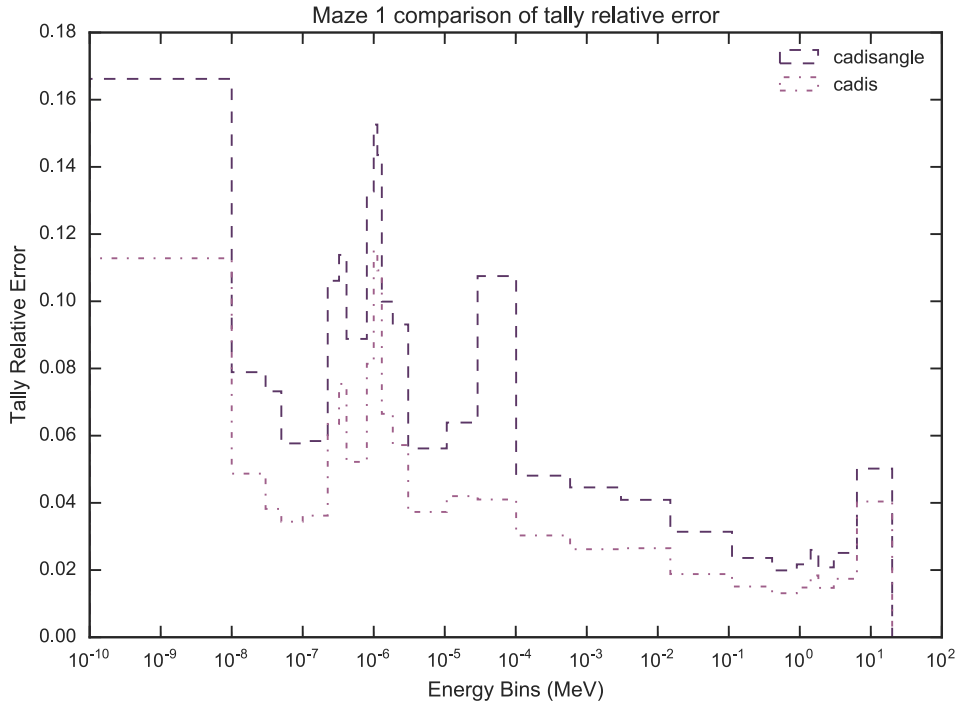
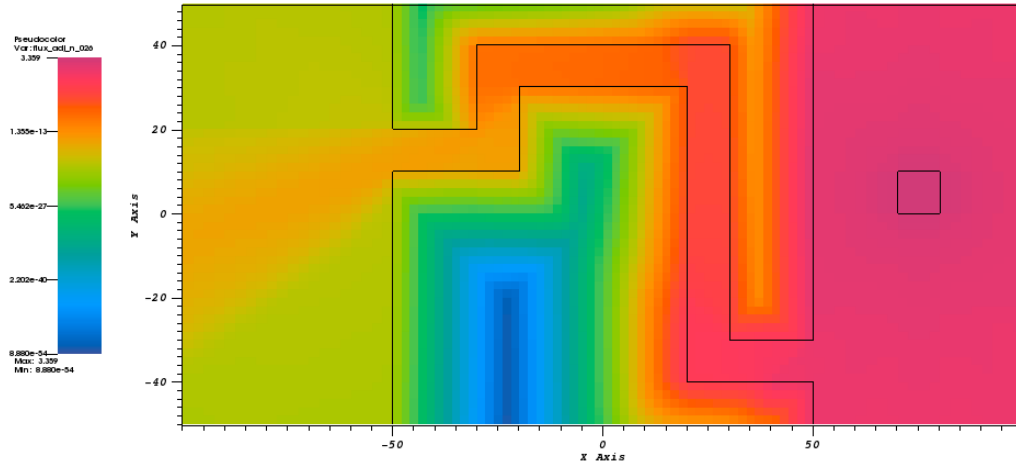


Figure 4.17: Tally relative error comparison between methods for a multiple turn labyrinth.

dependence and CADIS outperforms CADIS- Ω in all energy bins. This problem is poorly suited to CADIS- Ω .

Figure 4.18 shows the adjoint and Ω flux maps for the lowest energy group at the problem midplane for the multiple turn labyrinth. These figures look remarkably similar, showing that this problem does not have significant anisotropy to capture. The region that does differ is near the detector region, where the region of high importance is focused towards the labyrinth and the labyrinth exit. The other region with noticeable difference is located at the entrance to the maze. These figures show the lowest energy group particles, so for forward particles of this energy to go the same direction as adjoint particles, they must have gone into the labyrinth, scattered back out, and then scattered again. As a result, we do not see a strong directional dependence in the Ω -flux plot in the region near the forward source. The adjoint flux plot shows more of a streaming effect from the adjoint particles that exit the maze.

In Section 4.2.2, it was discussed that higher energy regions that contribute to the tally are more anisotropic, and that these regions benefit more from the Ω -flux map than they do with standard CADIS' importance map. Using the anisotropy metrics from Section 3.2.1, let us compare the anisotropy distributions of the single turn and multiple-turn labyrinth problems. Figure 4.19 are violin plots of the M_3 distributions of the labyrinth problems. To filter out values of the metric distribution that do not have a strong importance to



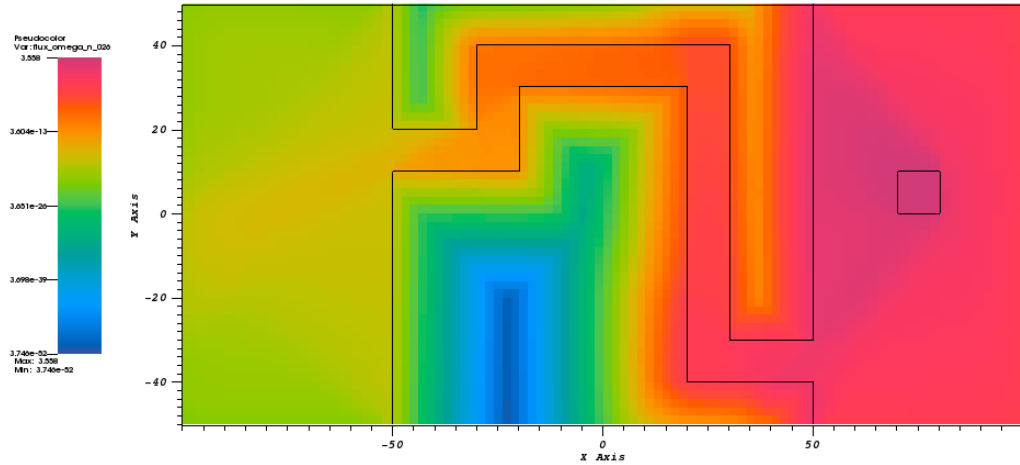
(a) Adjoint flux map for lowest energy group, multiple turn labyrinth.

contributing to the tally, only values from cells above the contribution flux mean value are included in the violins.

First, looking at the metric three distributions for both the single- (4.19a) and multiple-turn (4.19b) labyrinths, we can see that the violins in both plots shift from a fairly small grouping of values at high energies to a broad range of values at low energies. The bottom of the violin in each group also tells us a bit about the metric distribution. Because only values from “more important” cells have been included in these distributions, the bottom cutoff tells us how anisotropic the cells of median importance might be. It also tells us how many cells have high-valued anisotropy metrics. For both the single- and multi-turn labyrinths, we see higher-valued cutoff point in high energies than in low energies. This indicates that more cells in high energies have higher values of M_3 .

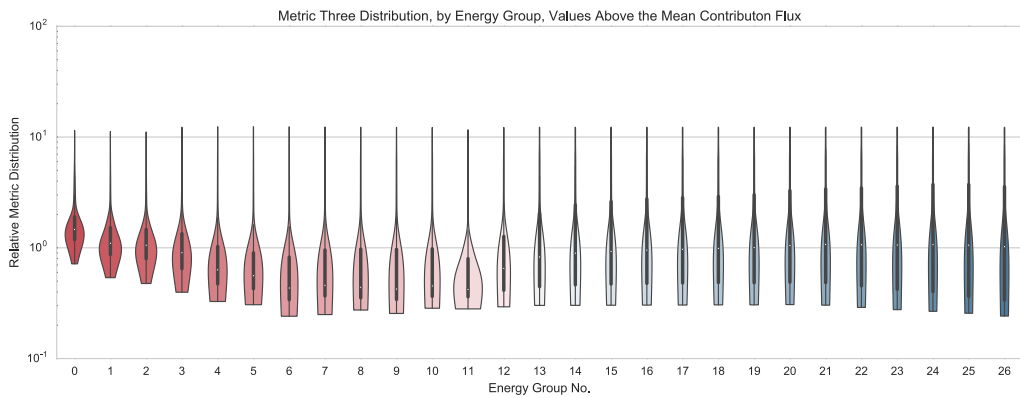
The violin plots of the multi-turn labyrinth (Fig. 4.19b) tend to span a larger range of values. That is, the violins tend to be longer. All of the violins in both plots have a bounding upper limit, meaning that in every energy group there are some very anisotropic cells. Interestingly, it appears that for the multi-turn labyrinth the distribution of anisotropies at low energies has no distinctive bunching, as observed in the single-turn labyrinth. This means that in important cells, there is an even distribution of very anisotropic, slightly anisotropic, and isotropic cells.

While the violin plots of Figure 4.19 are useful in seeing the overall distribution of metrics for the whole problem, it is also possible to plot them similarly to the flux maps shown previously. Figure 4.20 shows the M_4 distribution for the single and multiple turn labyrinth problems. Recall that this metric is the ratio of the contribution anisotropy to the standard



(b) Ω -flux flux map for lowest energy group, multiple turn labyrinth.

Figure 4.18: Flux map slice of multiple turn turn labyrinth. Flux maps have scales normalized to maximum and minimum values for each slice; between plots the scales are not consistent. These plots show the lowest energy group, group 026, for each cell in the problem midplane.



(a) M_3 distribution for single turn labyrinth

adjoint anisotropy. Cells that have blue coloring are those where the contribution max to average flux is lower than the adjoint. As a result, the forward and adjoint fluxes do not synergistically combine in angle. This generally means this is a region of lower importance. Values of unity mean that the contribution anisotropy is comparable to the adjoint anisotropy.

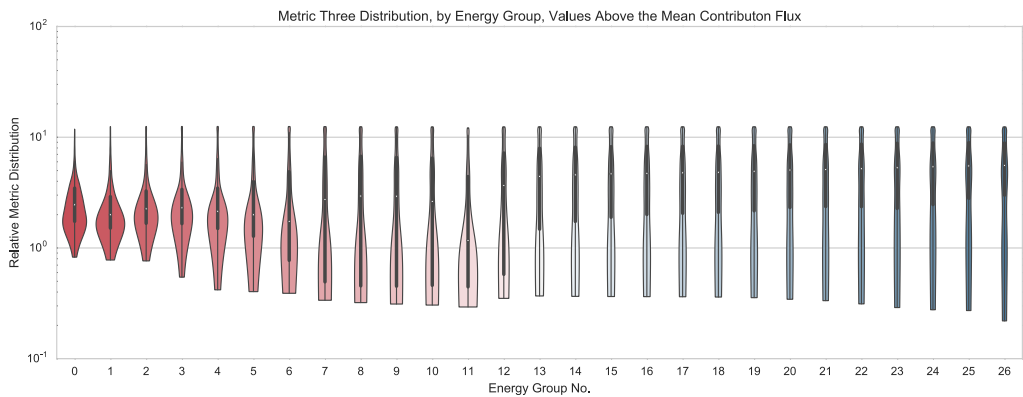
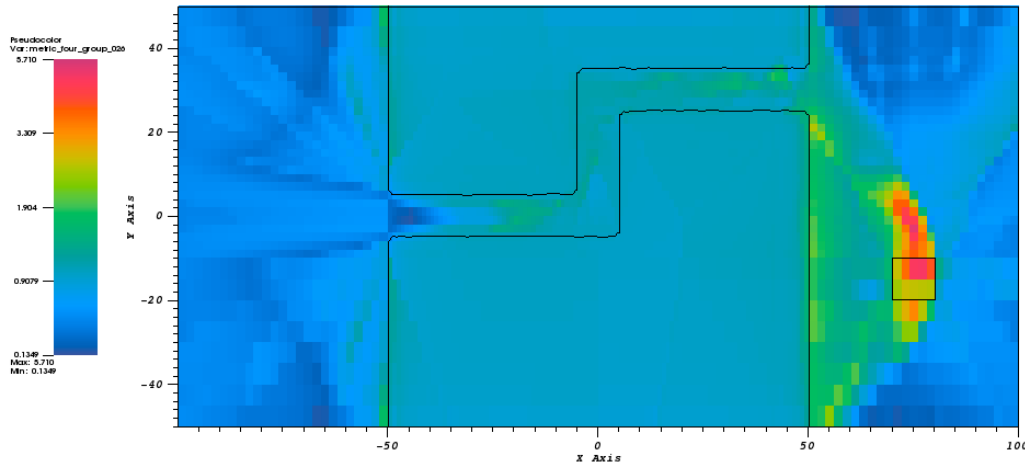
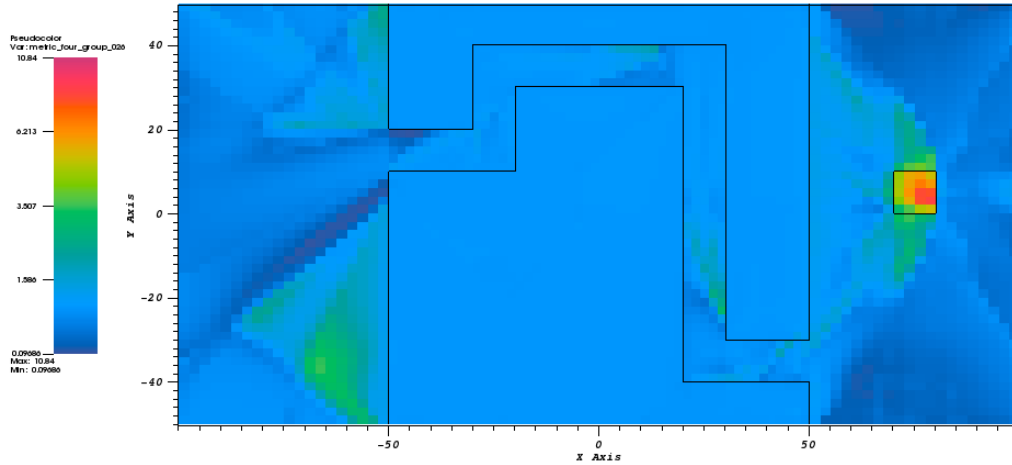
(b) M_3 distribution for multi-turn labyrinth

Figure 4.19: Violin plots of M_3 distribution using values above the mean contributon flux for labyrinth problems. Low energy group numbers correspond to high energies or fast particles, and are marked in red.

(a) M_4 lowest energy group, single turn labyrinth.

In figure 4.20a, it is clear that the concrete body of the maze is a region where the anisotropies are similar.

Figure 4.20a shows that the region where the anisotropy of the contributon flux differs the most from the adjoint flux is in the air region near the detector, and also in the air regions of the maze. Specifically, the anisotropy of the contributon flux is greater in the

(b) M_4 for lowest energy group, multiple turn labyrinthFigure 4.20: M_4 distributions at problem midplane for labyrinth problems.

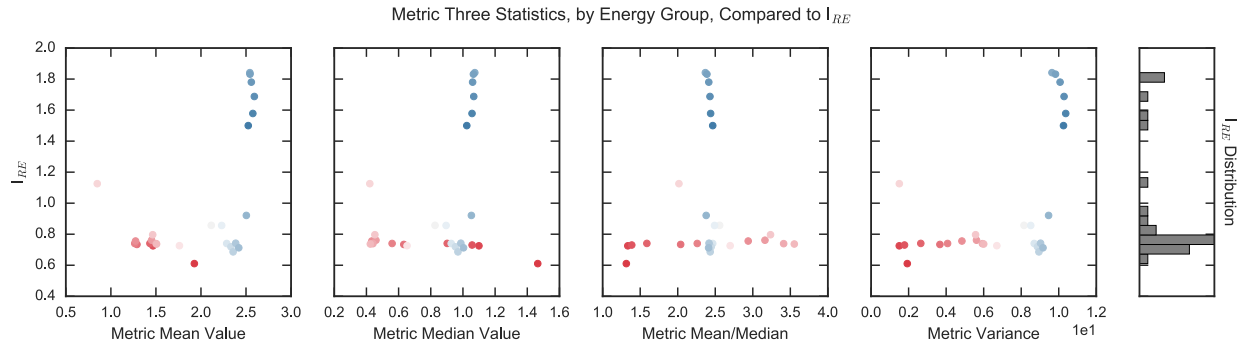
air region between the detector and the maze, and the anisotropy of the contributon flux is lower in regions behind the detector. Conceptually, we expect this anisotropy behavior in the region just past the detector, as the contributon flux will combine positively if the forward and adjoint fluxes are travelling in opposite directions, and will combine negatively if they are travelling in the same direction. As a result, the anisotropy of the contributon flux behind the detector will be minimized when compared to the original adjoint angular flux.

Figure 4.20b shows, like Figure 4.20a, the M_4 distribution at the problem midplane for the lowest energy group for the multiple turn labyrinth. In this problem we similarly see the strongest anisotropy in the flux near the NaI detector. However, the range of values is different. The concrete region of the maze still shows similar anisotropies between the contributon and adjoint angular fluxes. The maze edge next to the NaI detector also has some fairly anisotropic regions, but overall the anisotropies are less different in this problem than in the single turn labyrinth. As a result, CADIS- Ω does not have as much angular information to capture, and its importance map is less effective. This was also illustrated in the flux map comparison of Figure 4.18.

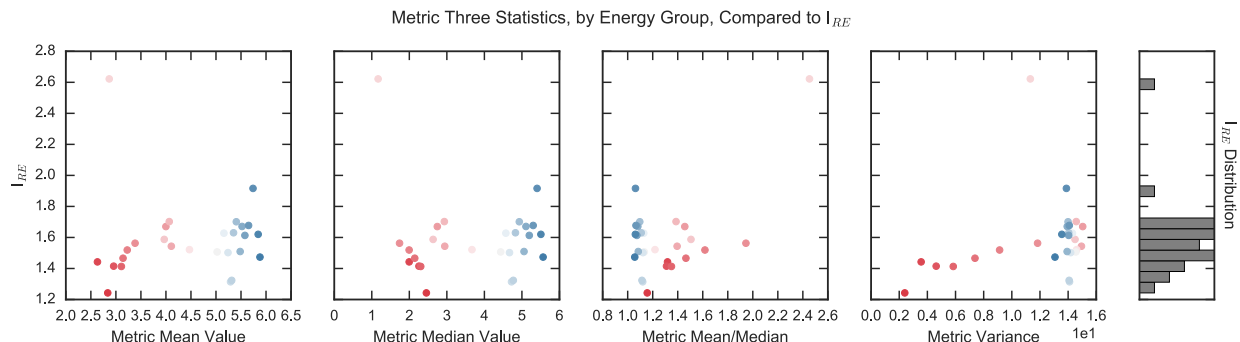
Both figures have interesting secondary features in the anisotropy in the air regions. These regions look similar to ray effects, but are not always reflected in the flux maps themselves. The author is not sure how to explain these effects, but they are worth future study.

It must be noted that while the trends in these violins are interesting, we must also be

wary of using comparing the violins directly. The filtering algorithm used to pull values out is dependent only on the contributon flux solution for that problem, so the average contributon flux cutoff for the single-turn labyrinth and multiple-turn labyrinth are different. Using a raw value from the violin plot in Figure 4.19b and directly comparing it to one from Figure 4.19a may be misleading. Instead, this analysis will focus on the general behavior of the metrics in each problem, not specific metric values.



(a) RE improvement factor as a function of M_3 statistics for single turn labyrinth



(b) RE improvement factor as a function of M_3 statistics for multi-turn labyrinth

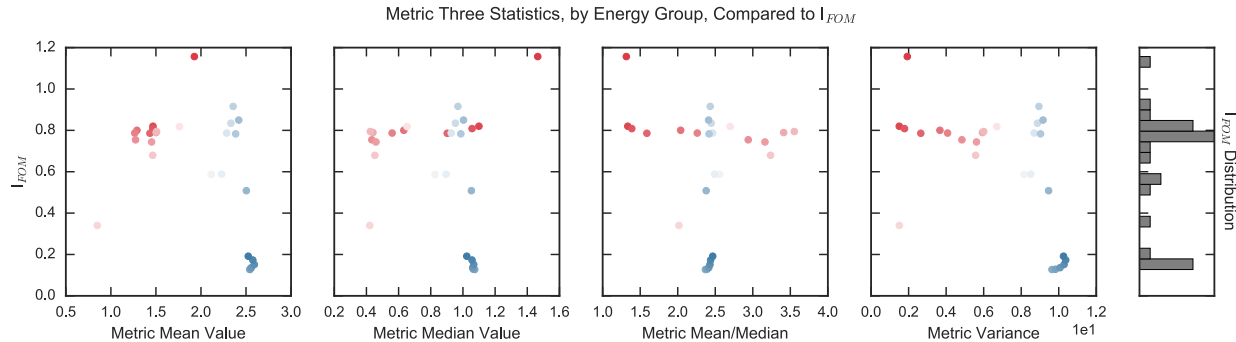
Figure 4.21: Relative error improvement factor as a function of M_3 distribution statistics. Metric distribution statistics are calculated using values of M_3 in cells with contributon flux values above the mean. Colors of datapoints correspond to the energy group to which they belong.

Figure 4.21 shows the improvement factors of the relative errors between CADIS- Ω and CADIS for the labyrinth problems. The x-axes of the plots in Figures 4.21a and 4.21b use the distribution statistics from the violins in Figures 4.19a and 4.19b, respectively. Recall that because I_{RE} is the ratio of the relative error between CADIS- Ω and CADIS—and we seek a low relative error—that values of I_{RE} below 1.0 indicate method improvement for CADIS- Ω .

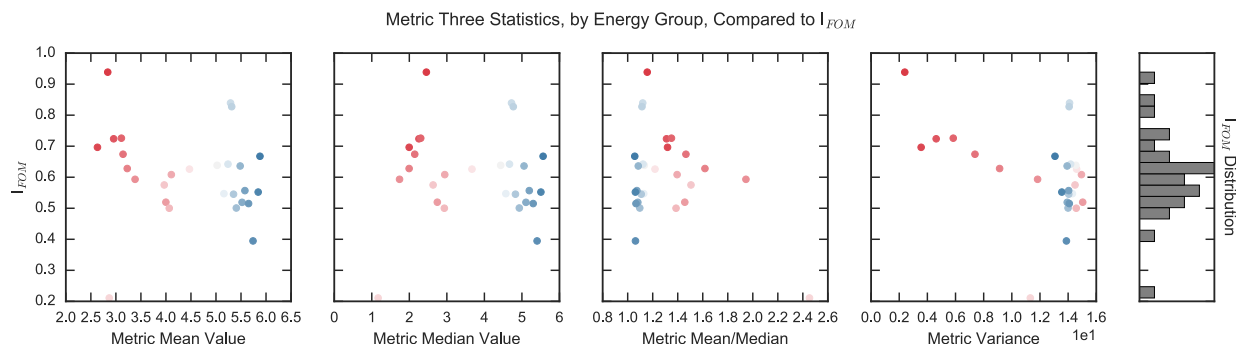
Looking at the differences between Figures 4.21a and 4.21b, some interesting effects can be observed. Recall from the relative error distribution plots for each problem (Figures 4.17

and 4.13) that CADIS- Ω had higher relative errors in all energy bins than CADIS for the multi-turn labyrinth, and a higher relative error in thermal energy groups in the single-turn labyrinth. Figure 4.21a shows the isolated grouping of poorer results for low energy bins in the single turn labyrinth. The rest of the values in this figure all show improvement in the relative error, while the low-energy group show better performance for CADIS. There is no distinct grouping in Figure 4.21b because all of the CADIS- Ω relative errors are higher than CADIS, so a distinct turnover in I_{RE} does not occur.

There does not seem to be a tight trend observable for any measurement of the M_3 distribution and I_{RE} in Figure 4.21a, but the higher values of I_{RE} generally occur in high mean values of M_3 and higher variances of M_3 . Figure 4.21b also shows this trend in the metric mean and variance subplots, with a single outlier in an intermediate energy group. It also appears that the spread of I_{RE} values does not change as a function of any of the metric values.



(a) FOM improvement factor as a function of M_3 statistics for single turn labyrinth



(b) FOM improvement factor as a function of M_3 statistics for multi-turn labyrinth

Figure 4.22: Figure of Merit improvement factor as a function of M_3 distribution statistics. Metric distribution statistics are calculated using values of M_3 in cells with contribution flux values above the mean. Colors of datapoints correspond to the energy group to which they belong.

Figure 4.22 builds off of what we've already observed in Figure 4.21. In this series of figures, I_{FOM} is plotted rather than I_{RE} . If CADIS- Ω has better FOM performance than CADIS, the resulting value of I_{FOM} will be above 1.0.

Many features from Figure 4.21 continue in Figure 4.22. The distinct grouping of low-energy results for the single turn labyrinth are also observable in 4.22a. The intermediate energy outlier for the multiple turn labyrinth is located at the bottom of all of the subplots in Figure 4.22b. By adjusting our results to include timing, even less of a trend with metric distribution measurements is seen in the improvement metric for the single turn labyrinth. However, for the multiple turn labyrinth it does appear that as the metric mean value increases, I_{FOM} decreases.

4.2.4 Steel Beam

The steel beam embedded in concrete FOM and timing results are summarized in Tables 4.9 and 4.10. Figures 4.23 and 4.24 show the results obtained by the track length tally in CADIS, CADIS- Ω and the nonbiased analog Monte Carlo.

	CADIS		CADIS- Ω		analog
	MC	MC_{hybrid}	MC	MC_{hybrid}	MC
tally avg	668	659	3e+03	2.96e+03	1.39
max RE	3.74	3.69	6.79	6.71	0.0448
min RE	1.43e+03	1.41e+03	1.33e+03	1.31e+03	–
time (mins)	414	420	2.09e+03	2.11e+03	22.3

Table 4.9: Figure of Merit comparison for steel bar embedded in concrete.

		CADIS	CADIS- Ω	analog
		time (minutes)		
MCNP time	total	414.45	2086.60	22.33
deterministic time	advantg_time	0.18	0.18	–
	denovo_time	5.69	25.64	–
	dispose_time	0.00	0.16	–
	omega_time	0.00	0.66	–
	total	5.87	26.49	–
wall time		420.32	2113.09	22.33

Table 4.10: Detailed timing results for steel bar embedded in concrete.

Tables 4.9 and 4.10 show that this problem is very difficult for analog Monte Carlo and that CADIS- Ω generally performs better than CADIS. In fact, CADIS- Ω has the best performance in this problem of all of the characterization problems.

For both CADIS and CADIS- Ω , this problem has a huge disparity in the FOMs calculated with the maximum and minimum relative error. As a result, depending on the convergence requirements that a user might require, the time to achieve a desired solution could vary significantly in applications. However, both CADIS and CADIS- Ω improve on the unbiased analog Monte Carlo's FOM by a factor of 10^2 or more.

CADIS- Ω outperforms CADIS for the FOMs calculated with the tally average relative error and the tally maximum relative error. This indicates that giving a limiting relative error to which all energy bins must converge, CADIS- Ω will achieve it in 1/3rd the time that CADIS will. Further, CADIS- Ω has a better FOM than CADIS when the deterministic runtimes are added. As shown in the timing table, the time to run and generate the variance reduction parameters for CADIS- Ω will always be longer than CADIS due to the addition of the forward transport run. The addition of deterministic runtimes has the potential to lower the FOM of CADIS- Ω more than that of CADIS, so CADIS- Ω 's achievement of a FOM higher FOM with much longer runtimes in both Monte Carlo and ADVANTG illustrates just how much lower the relative error it achieves is. CADIS- Ω is very well-suited to a problem with these conditions.

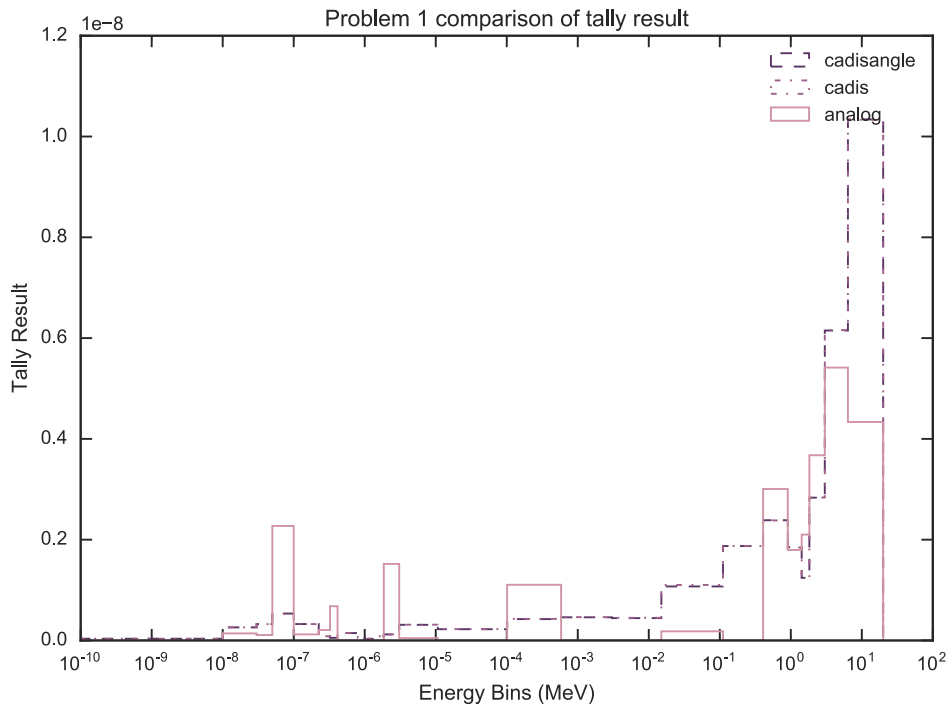


Figure 4.23: Tally results comparison between methods for steel bar embedded in concrete.

Figure 4.23 shows that CADIS and CADIS- Ω are in agreement for the tally results in all energy bins. The nonbiased Monte Carlo calculation differs from both of the hybrid methods. This supports what was observed in the nonbiased analog FOM values of Table

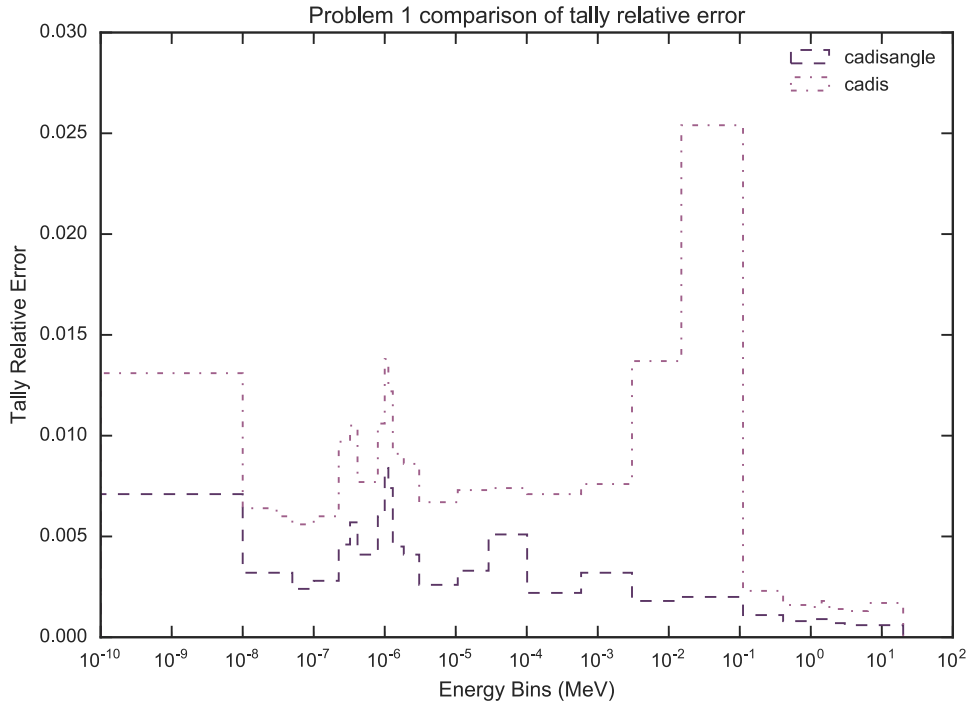


Figure 4.24: Tally relative error comparison between methods for steel bar embedded in concrete.

4.9. Figure 4.24 shows that CADIS- Ω achieves a consistently lower relative error than CADIS for all energy bins. For most energy bins, CADIS- Ω 's relative errors are shifted a consistent fraction below CADIS'. In the energy regions between 10^{-4} and 10^{-1} MeV, this is not the case. For these energy regions CADIS' relative errors spike while CADIS- Ω 's do not.

From the FOM results presented in Table 4.9 and the tally results and error in Figures 4.23 and 4.24, we can conclude that CADIS- Ω 's source biasing parameters consistently move more particles in all tally energy bins more effectively than CADIS. The importance map generated by CADIS- Ω better reflects the problem physics and more efficiently transports particles to the desired tally location.

4.2.4.1 Air Channel Variant

The characterization problems have been designed to induce anisotropy in the flux. Most of these problems do so, in some part, by using air to induce particle streaming. The steel beam in concrete problem requires that particles interact with a high density material (either steel or concrete) before reaching the detector to induce a response. These next two variant problems explore whether the material choice of steel strongly affects the Ω -method's ability to generate variance reduction parameters. This first variant keeps the

geometric configuration of the steel beam problem the same, but the steel is replaced with air. If the Ω -methods are more sensitive to air, then this change in the materials composition should affect the results.

	cadis		cadisangle		analog	
	MC	MC_adjusted	MC	MC_adjusted	MC	
tally avg	432	390	396		364	5.63
max RE	1.17	1.05	0.247		0.227	0.0467
min RE	273	247	296		272	–
time (mins)	47.3	52.3	247		268	21.4

Table 4.11: Figure of Merit comparison for air variant of the steel beam problem geometry. In this variant problem, the steel bar volume region is replaced with air to exacerbate the suggested splitting issues encountered in other hybrid problems.

		cadis	cadisangle	analog
	time (minutes)	time (minutes)	time (minutes)	time (minutes)
MCNP time	total	47.29	246.83	21.42
deterministic time	advantg_time	0.16	0.15	–
	denovo_time	4.90	20.50	–
	dispose_time	0.00	0.15	–
	omega_time	0.00	0.65	–
	total	5.05	21.30	–
wall time		52.34	268.13	21.42

Table 4.12: Detailed timing results for steel beam geometry air variant.

Tables 4.11 and 4.12 summarize the FOM and timing results for the air variant of the steel beam problem. Comparing the FOMs for this variant and for the steel variant (Table 4.9), it is clear that CADIS- Ω performs more poorly than CADIS with air. Interestingly, CADIS- Ω 's minimum relative error FOM is better than CADIS', which is opposite to the results for the standard steel problem. For the maximum relative error, CADIS- Ω 's FOM is 1/5th that of CADIS'. However, for this problem CADIS- Ω 's runtime is almost five times that of CADIS. Considering this time difference, it appears that CADIS- Ω requires far more sampling with its importance map than CADIS. These sampling requirements also exist with the original steel problem, but the importance map reduces the tally variance enough to offset the time addition. This is not the case for the air variant. From this, we can conclude that the addition of air into this problem geometry reduces the sampling interaction points enough to negatively affect the Ω -method. Further, it lowers the FOMs achieved by both CADIS and

CADIS- Ω substantially that their improvement over the nonbiased analog reduces almost an order of magnitude.

The runtimes in Table 4.12 are also worth comparing with the original steel variant. In particular, the deterministic runtime in both of the problems is on the same order of magnitude. However, the Monte Carlo runtime is far longer in the original steel version. The runtimes in the air variant are generally much shorter for CADIS and CADIS- Ω , but comparable for the nonbiased analog. In this problem, the fraction of time spent in the deterministic solve is much higher than in the steel version.

4.2.4.2 Concrete Channel Variant

In addition to the air variant of the steel beam geometry, we can see if having non-preferential flowpaths might affect the Ω -method's performance. Recall that the Ω -methods have been designed to incorporate angular information into the importance map. If no preferential flowpaths exist through the problem geometry, then the Ω -importance map may have less of an impact on improving the tally convergence. However, because the entire shield is composed of concrete, then the distance to sampling location should still be quite small as with the original steel version of the problem. As a result, there should be some positive effects on the Ω -methods due to sampling interaction frequency. Tables 4.13 and 4.14 show the FOM and timing results for this material variant of the steel beam geometry.

	cadis		cadisangle		analog	
	MC	MC_adjusted	MC	MC_adjusted	MC	MC
tally avg	2.6e+03	2.55e+03	3.16e+03	3.13e+03	1.54	
max RE	14.5	14.2	9.48	9.39	0.0457	
min RE	1.54e+03	1.51e+03	1.4e+03	1.39e+03	–	
time (mins)	385	393	1.98e+03	2e+03	21.9	

Table 4.13: Figure of Merit comparison for concrete variant of steel bar geometry. In this variant problem, the steel bar volume region is replaced with concrete to eliminate the preferential particle travel through the beam region.

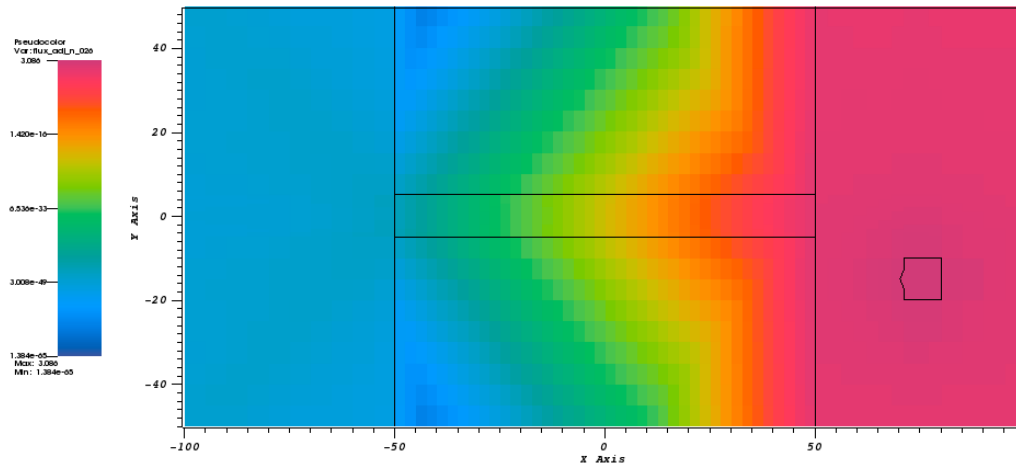
Tables 4.13 and 4.14 show the results of the concrete variant of the steel beam problem. As with the original steel and air versions described previously, the runtimes for CADIS- Ω are quite long when compared to CADIS. In each variant, the runtimes are about five times longer than those observed for CADIS. Similarly to the steel variant, in this version CADIS- Ω achieves a superior FOM for the tally average FOM. However, CADIS- Ω 's FOMs for the maximum and minimum relative error FOMs are both lower than CADIS'. Both CADIS and CADIS- Ω far outperform the nonbiased analog Monte Carlo.

To compare the performance of each of the variants of this problem, let us first compare the differences in the flux distributions for the Ω and CADIS versions of the problem. Figure 4.25 shows the adjoint and Ω fluxes for the steel beam in concrete version of this geometry.

		cadis time (minutes)	cadisangle time (minutes)	analog time (minutes)
MCNP time	total	385.11	1978.46	21.88
deterministic time	advantg_time	0.23	0.15	—
	denovo_time	7.42	19.58	—
	dispose_time	0.00	0.09	—
	omega_time	0.00	0.56	—
	total	7.65	20.29	—
wall time		392.76	1998.75	21.88

Table 4.14: Detailed timing results for concrete variant of steel bar.

It is clear from both of these two figures that there is a preferential flowpath through the steel beam for both the standard adjoint and for the Ω -fluxes.



(a) Adjoint flux distribution, lowest energy group

As with the multiple-turn labyrinth, the flux maps are very similar between the adjoint and Ω -flux plots in this figure. Recall that M_2 is the ratio of the scalar Ω -flux to the scalar adjoint flux in each cell. Figure 4.26 shows the M_2 distributions for each of the material variants of the steel beam problem. Figure 4.26a contains the distribution of M_2 for the original steel variant, Figure 4.26b is of the variant with air replacing the steel, and Figure 4.26c. Note that Figure 4.26b has the colormap scaled to a log scale, while the other two

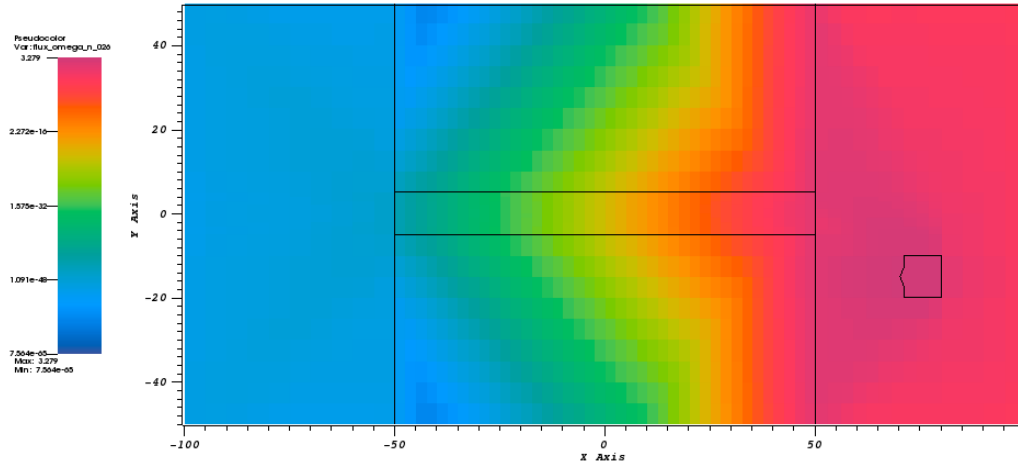
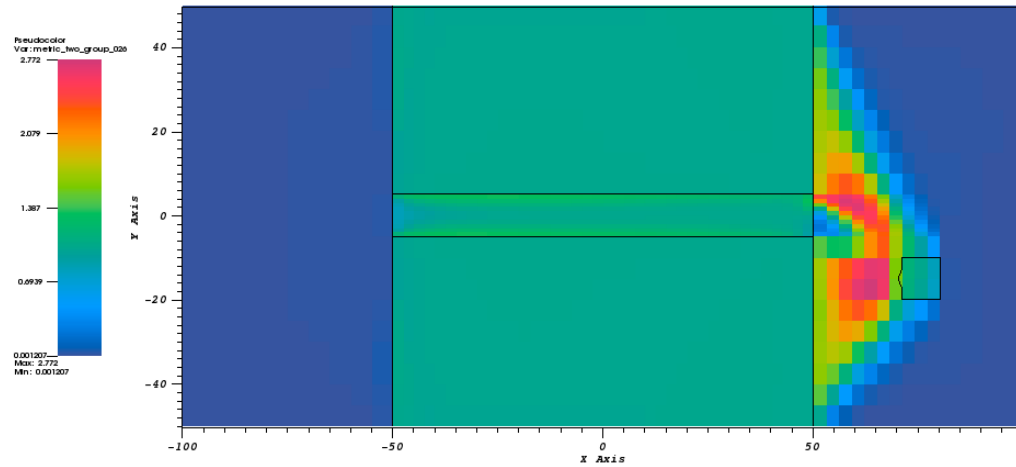
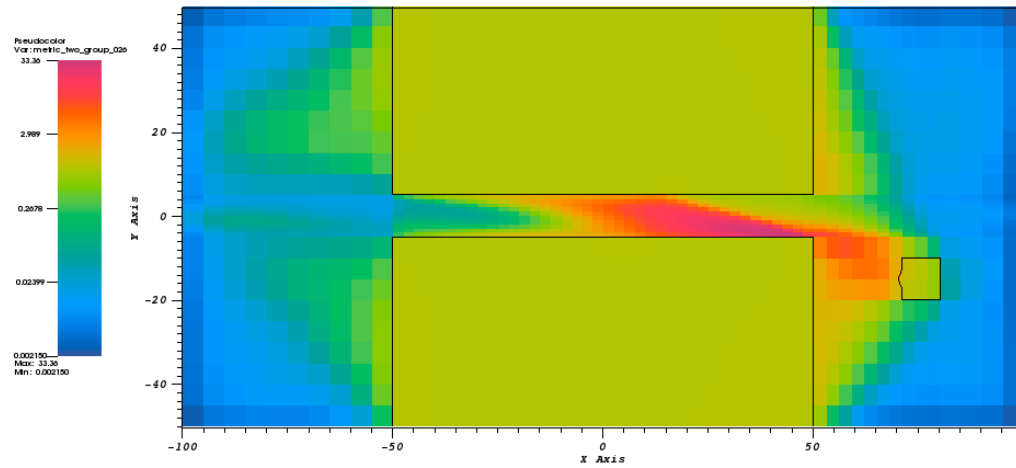
(b) Ω -flux distribution, lowest energy group

Figure 4.25: Flux maps for steel beam in concrete. Fluxes shown are at problem midplane, and energy group 026. The colormap for each has been scaled to the data in the plane.

figures do not. This is because the range is much larger in this figure, and a linear scale obscures the data.

By comparing the ratio of the Ω - to adjoint-fluxes in each of the figures in 4.26, the effect that material choice has on changing the Ω -flux becomes more apparent. First, all three plots show a constant value of M_2 within the concrete shield itself. As a result, we can conclude that materials in which the particles have a small mean free path of travel, the flux isotropy is fairly constant and does not differ between the Ω - and adjoint fluxes. Next, having a preferential flowpath through the shield does change the resultant Ω -flux. Depending on material, the flux may be very different (as with the air in Figure 4.26b) or fairly similar (as with the flux ratio in the steel in Figure 4.26a). All three problems show a very different distribution of fluxes near the adjoint source. This is the case with both of the labyrinth variants previously discussed.

The subfigures of Figure 4.27 complement those presented in Figure 4.26. As with Figure 4.26, the subfigures here are normalized by the adjoint problem. Rather than comparing the adjoint scalar fluxes, here the contribution anisotropy in each cell is compared to the adjoint. Similar features can be observed between the subfigures in 4.27 and their counterparts in 4.26. For example, the anisotropies in the cells in the shield are the same as the adjoint. As a result, we see little- to no- difference between the Ω -method anisotropy or the standard adjoint anisotropy. Figure 4.27b shows some interesting streaming effects on the anisotropy

(a) M_2 distribution for steel beam in concrete.(b) M_2 distribution for steel beam in concrete, air variant.

in the air channel within the shield. In particular, the contribution anisotropy is larger for the majority of the air channel than the adjoint anisotropy. There is an exception to this observation at the M_4 values marked with dark blue in the air channel.

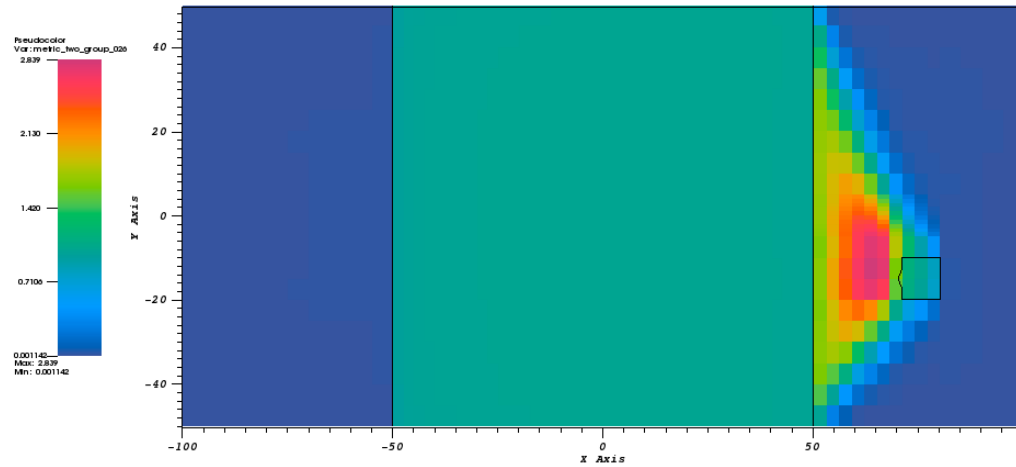
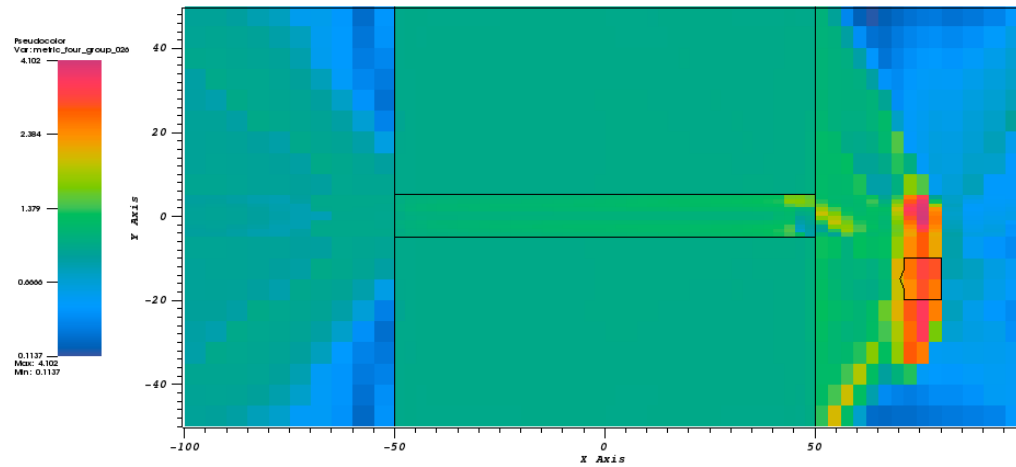
(c) M_2 distribution for steel beam in concrete, concrete variant.

Figure 4.26: M_2 distribution plots for material variants of steel beam in concrete. Distribution shown is for lowest energy group. Scales adjusted to match dataset of each figure.

(a) M_4 distribution for steel beam in concrete.

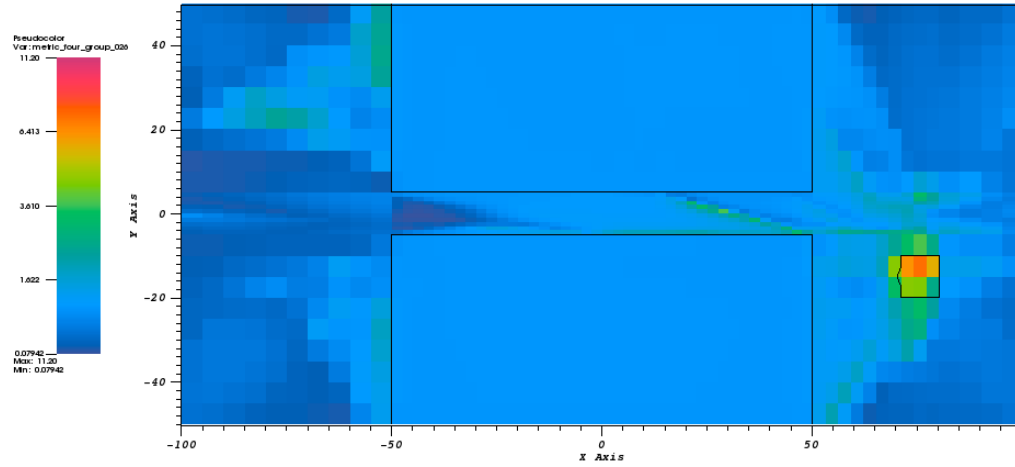
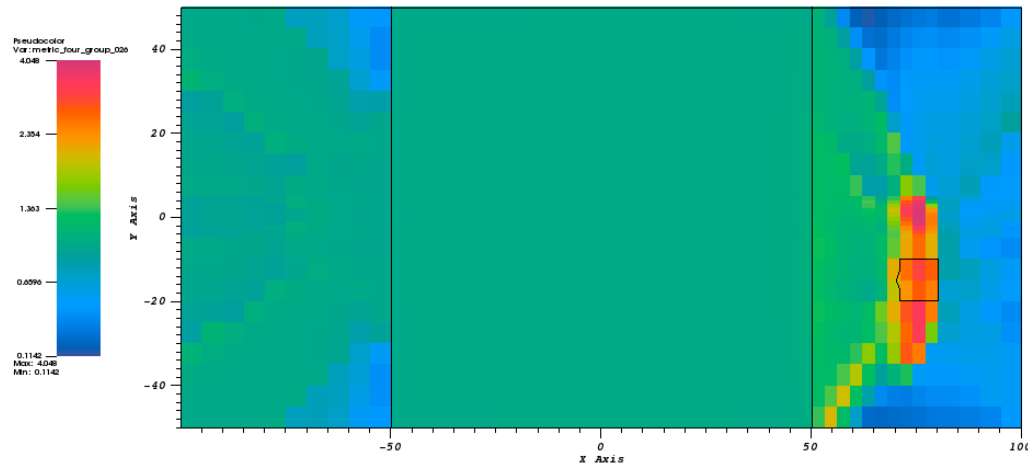
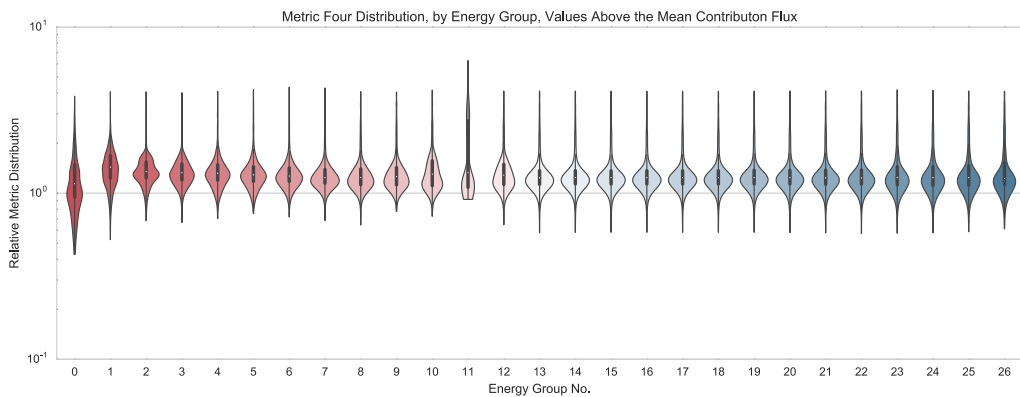
(b) M_4 distribution for steel beam in concrete, air variant.(c) M_4 distribution for steel beam in concrete, concrete variant.

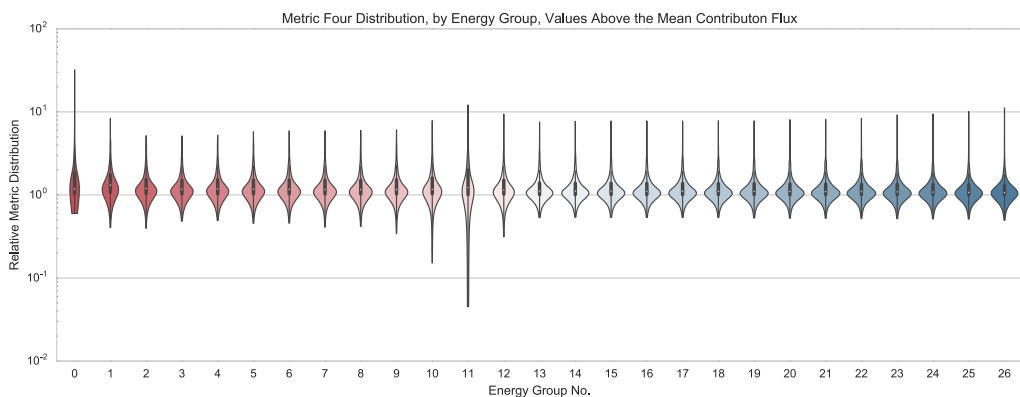
Figure 4.27: M_4 distribution plots for material variants of steel beam in concrete. Distribution shown is for lowest energy group. Scales adjusted to match dataset of each figure.

All three subfigures in 4.27 show that there exist differences in the anisotropy near the adjoint source and near the forward source in all material variants of this problem. Unlike the subfigures of 4.26, the anisotropies extend all the way to the problem boundaries in the air regions of the problem. However, the anisotropy in the area of each problem near the detector is generally larger than the anisotropy in the area nearer the forward source.

With an intuition of how the Ω and adjoint-scalar fluxes differ both on the cell-scale, and how their anisotropies differ on the cell scale, we can now look at the effectiveness of each at predicting the Ω -method's success (or lack thereof). Recall that Figures 4.26 and 4.27 show the anisotropy distributions for the lowest energy group. On the next several figures, the data illustrated by these figures will correspond with the darkest blue violin and the darkest blue scatterplot data point, respectively. The next several figures attempt to collapse the substantial quantity of data available in Figures 4.26 and 4.27 to values with which we can correlate with Ω -relative error or FOM improvement.



(a) M_4 distribution for steel beam geometry



(b) M_4 distribution for air beam geometry

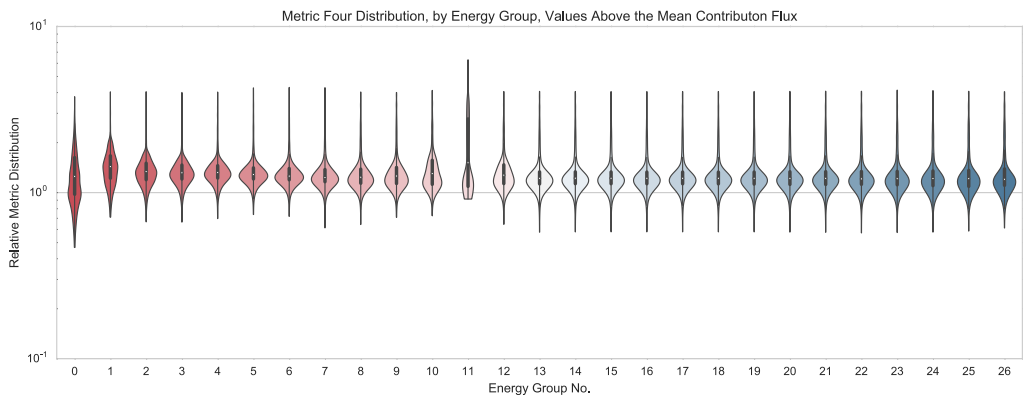
(c) M₄ distribution for concrete beam geometry

Figure 4.28: Distribution plots of M₄ for the steel beam problem geometry material variants. Distributions have been filtered from cells that are in bins above the contribution average flux in each problem. Coloring corresponds to energy group, red indicates a higher energy group and blue a lower energy group.

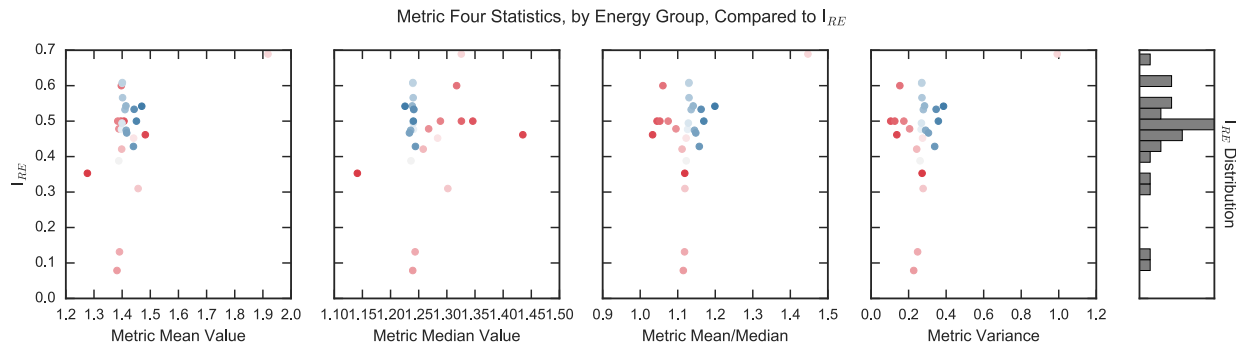
The beam problem material variants provide a very interesting opportunity to see the effect of material properties on I_{RE} and on the anisotropy metric distributions. Based on observations, the distributions for M₄ will be shown for these problem variants in 4.28 and 4.29. Figure 4.28a shows the M₄ distribution for each energy group as a violin plot for the original steel version of the problem. Figures 4.28b and 4.28c show the air and concrete variants of the problem, respectively. Note the similarity between the metric distributions for the steel and concrete variants of the problem (Figs. 4.28a and 4.28c). The metric distributions have similar ranges, similar distributions, and similar mean values. The only energy groups where there are noticeable differences are in the highest energy groups, where the local minimum values differ, and in energy group three, where the distribution between the two problems differs.

Compare what was observed in the concrete and steel variations of the problem to Figure 4.28b, which contains the M₄ distributions for air. The range in values for each of these violins is much larger than either 4.28a or 4.28c. Energy group 11 does not bottom out as it does in the previous two problems. The fastest energy group is strongly peaked upwards, as are many low energy groups. While the distribution of each of the metrics for this problem are much broader, the main body of the distributions are centered around lower values than either 4.28a and 4.28c.

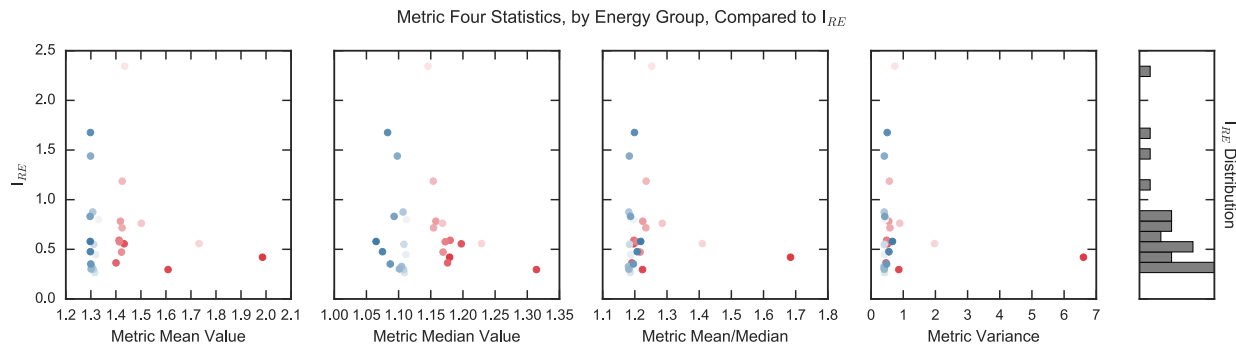
The differences in the violin plots are purely due to differences in the sampling physics of the problem. Despite different materials in the concrete and steel variants of the problem, 4.28c and 4.28a have similar violin distributions. This tells us that while the overall energy spectrum of the problem may be different, the distribution of anisotropy within the problem may be more dependent on how likely particles are to collide. That is, because both steel

and concrete have higher interaction probabilities than air, their anisotropy distributions will be closer to each other than air.

Because the problem geometries and mesh sizes are identical between each of these problems, it is likely that the selection of values is at similar locations in each of the problems. However, because the filter matrix described in Section 4.1.3 is based on the contribution flux, which is problem specific, these will still differ between problems. Further, the number of cells selected from each energy group will differ between problems.



(a) I_{RE} for M_4 for steel beam geometry



(b) I_{RE} for M_4 for air beam geometry

Based on the violin plots in 4.28, it was observed that the M_4 distribution was far different in the air variant of this problem geometry than the steel or concrete variants. This is also observable in Figure 4.29, which plots the relative error improvement metric, I_{RE} with different metric distribution values. Recall that a low I_{RE} means that the Ω method achieved a superior relative error to standard CADIS.

Figures 4.29a through 4.29c shows the relative error improvement factors for each of the steel beam material variants described in 4.28. For both the steel and concrete problems, CADIS- Ω has favorable values for I_{RE} in most energy bins. In Figures 4.29a and 4.29c there appears to be a trend in I_{RE} with both the metric variance and the metric skew—the ratio of the mean to the median values—which indicates that the metric distribution rather than

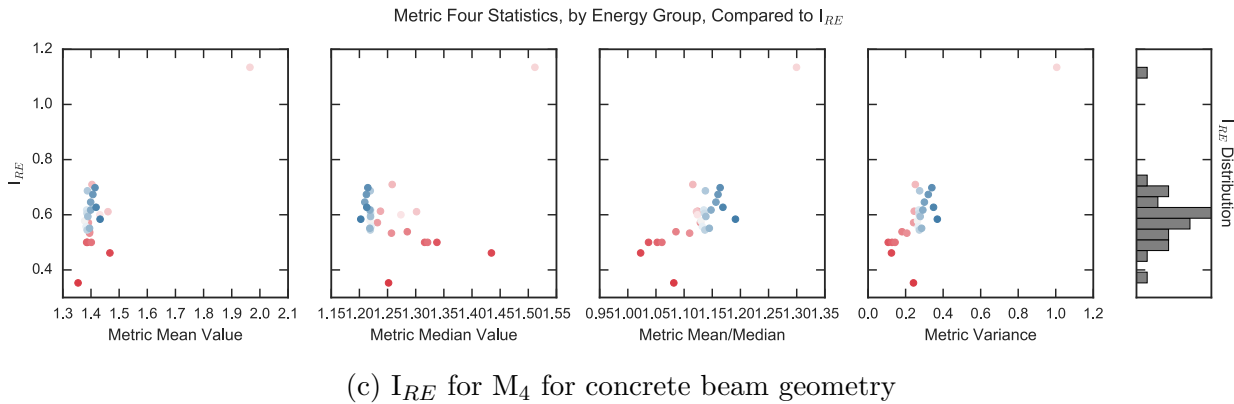


Figure 4.29: Scatterplots of values describing M_4 distribution against I_{RE} for steel beam problem geometry material variants. As with the distributions in 4.28, M_4 is based on values filtered out in cells located above the contribution flux average value. The values on the x-axes of the figures are evaluated based on the subset of M_4 values. Coloring of datapoints correspond to the energy groups.

the metric average are more likely to be related to the improvement in the relative error for these problems. This trend is not observable for the air variant in Figure 4.29b. In fact, the metric mean and median values are better indicators for I_{RE} than the distribution values.

Looking at the distributions of I_{RE} it is clear that despite the similar metric distribution values, the concrete and steel variants of this problem do have different performances. Disregarding energy group 11, which is an outlier in all three problem figures, the two problems have similar ranges of I_{RE} . However, the highest energy groups have the lowest I_{RE} for the concrete problem, while the lowest values in the steel problem occur in intermediate energy groups.

4.2.5 U-Shaped Corridor

The U-shaped air corridor embedded in concrete FOM and timing results are summarized in Tables 4.15 and 4.16. Figures 4.30 and 4.31 show the results obtained by the track length tally in CADIS, CADIS- Ω and the nonbiased analog Monte Carlo.

Much like the single- and multiple-turn labyrinths, the U-shaped air corridor has a pathway of preferential movement for particles in a concrete shield. In this problem, the particles travel down the legs of the u-bend to a detector on the other side of the corridor. The particles should have preferential flowpaths through the air ducts, but it is possible for low energy particles to traverse the concrete barrier between the source and detector. The high energy particles tallied in the detector are more likely to have traveled through the air ducts and the low energy particles may be supplied from the shield or from scattering down the air duct.

The FOM table for the u-shaped corridor shows that this is a fairly difficult problem

	CADIS		CADIS- Ω		analog
	MC	MC _{hybrid}	MC	MC _{hybrid}	MC
tally avg	64.1	51.9	60.2	38.3	0.378
max RE	0.0183	0.0148	0.0144	0.00913	0.0644
min RE	14.9	12	13.4	8.54	–
time (mins)	54.6	67.5	188	296	15.5

Table 4.15: Figure of Merit comparison between methods for U-shaped air corridor in concrete.

		CADIS	CADIS- Ω	analog
		time (minutes)		
MCNP time	total	54.61	187.92	15.54
deterministic time	advantg_time	0.19	0.21	–
	denovo_time	12.68	105.90	–
	dispose_time	0.01	0.35	–
	omega_time	0.00	1.49	–
	total	12.87	107.60	–
wall time		67.48	295.52	15.54

Table 4.16: Detailed timing results for U-shaped air corridor in concrete.

for CADIS, CADIS- Ω , and the analog. For the tally average FOM, CADIS and CADIS- Ω achieve a FOM two orders of magnitude higher than the nonbiased analog. Both methods have comparable FOMs. In fact, CADIS and CADIS- Ω are in relative agreement for all FOMs calculated with the Monte Carlo runtime. Interestingly, the nonbiased analog Monte Carlo has a higher maximum relative error FOM than either method. However, this analog tally for this problem has many nontallied bins (as can be gathered from the major discrepancy in results in Figures 4.30 and 4.31). For the few bins that were tallied, the analog has a high FOM.

The tally results for the u-shaped corridor in Figure 4.30 show general agreement between CADIS and CADIS- Ω . The nonbiased analog has no agreement with either method. Comparing their relative errors in Figure 4.31, we can gather that this is a difficult problem for both methods. At high energies both CADIS and CADIS- Ω have very high relative errors, indicating untrustworthy results. To get the relative error in these regions for CADIS- Ω to below 0.10—a fairly standard threshold for Monte Carlo—it would have to run nearly 40x longer, or 900 hours. However, CADIS- Ω achieves a uniformly lower relative error than CADIS for all energy bins. Because the time to run CADIS- Ω is so much longer, the FOM is impacted and appears worse than CADIS. Therefore, should CADIS- Ω use the same runtime as CADIS, CADIS will achieve superior relative errors. Conversely, if CADIS- Ω uses

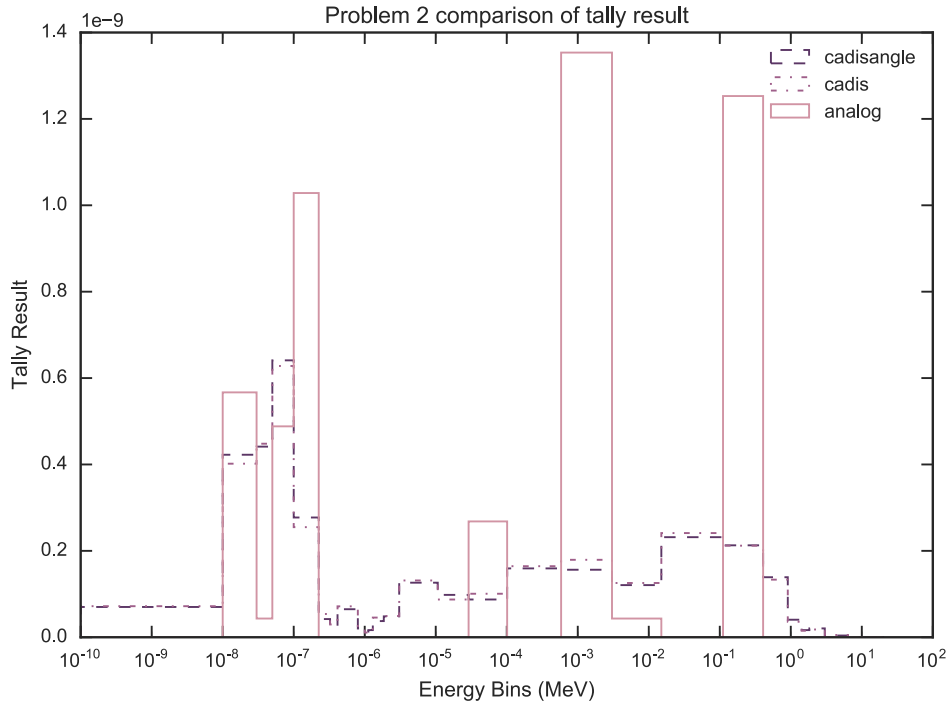


Figure 4.30: Tally results comparison between methods for U-shaped air corridor in concrete.

the same particle count as CADIS, CADIS- Ω will achieve superior relative errors.

While the u-shaped bend problem does not have FOMs for CADIS- Ω that significantly improve upon CADIS', CADIS- Ω still achieved lower relative errors than CADIS. Figure 4.32 shows the flux distributions in the U-bend located at the midplane containing the NaI detector. Figure 4.32a shows the adjoint scalar flux, Figure 4.32b shows the angle-integrated contributon scalar flux, and Figure 4.32c shows the Ω -flux, all at the same problem midplane.

As with the single-turn labyrinth, the adjoint scalar flux in Figure 4.32a shows substantial ray effects in the air regions near the adjoint source. As expected, the ray effects are mitigated once the particles interact with concrete. The difference in flux value between the orange region and the yellow regions of the plot is on the order of two- to three- orders of magnitude. The two ray effect fingers are separated by a distance of 10-20cm, meaning that a particle traversing air in this region may experience fairly large differences in importance between scattering events.

In this problem the forward source is offset in the z-plane from the detector by 100cm. The effects of this on the flux are visualized well by the contributon flux in Figure 4.32b. In the left-leg of the u-bend, the contributon flux decreases near the bottom. This is because particles are more biased in a deeper z-plane, towards the forward source. It is also clear from this figure that in the high energy region, the contributon flux streams particles through the concrete shield.

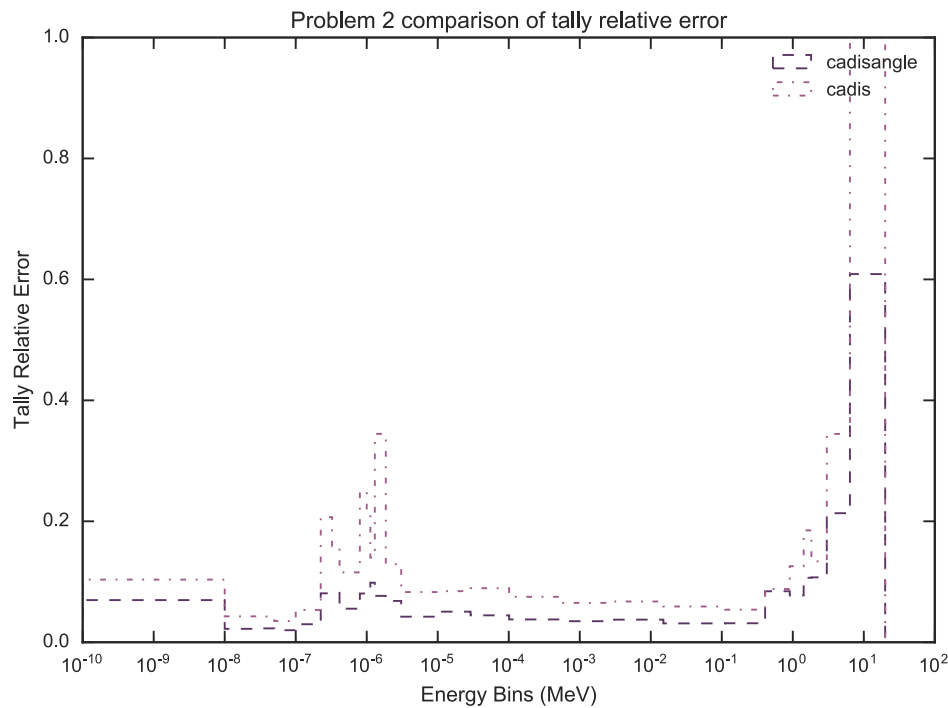
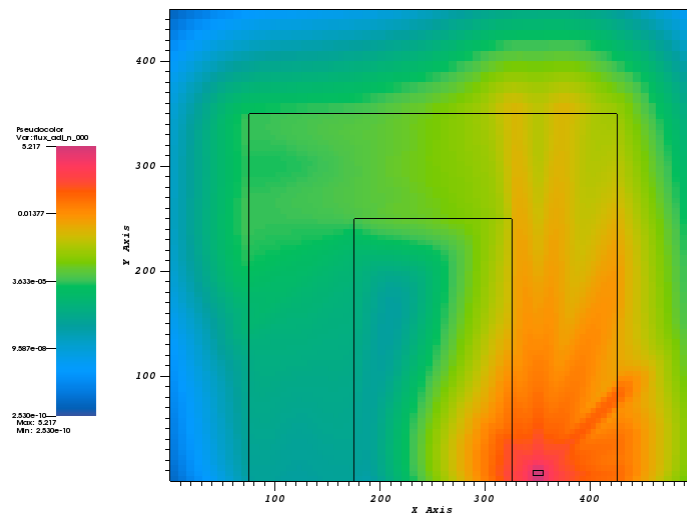
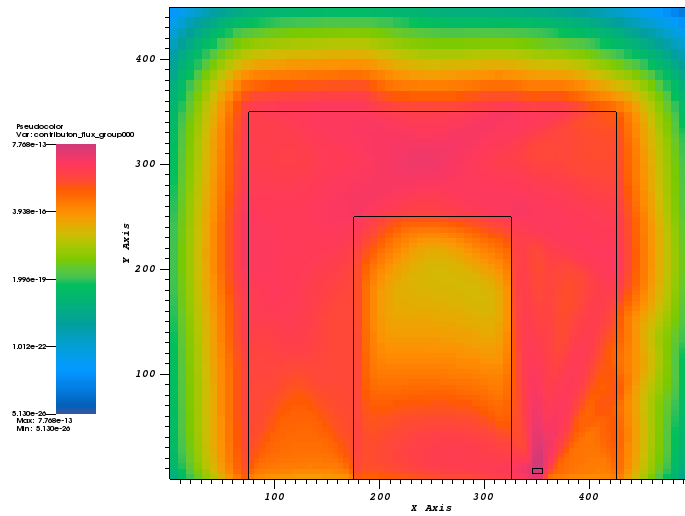


Figure 4.31: Tally relative error comparison between methods for U-shaped air corridor in concrete.



(a) Adjoint flux distribution, highest energy group



(b) Contribution flux distribution, highest energy group

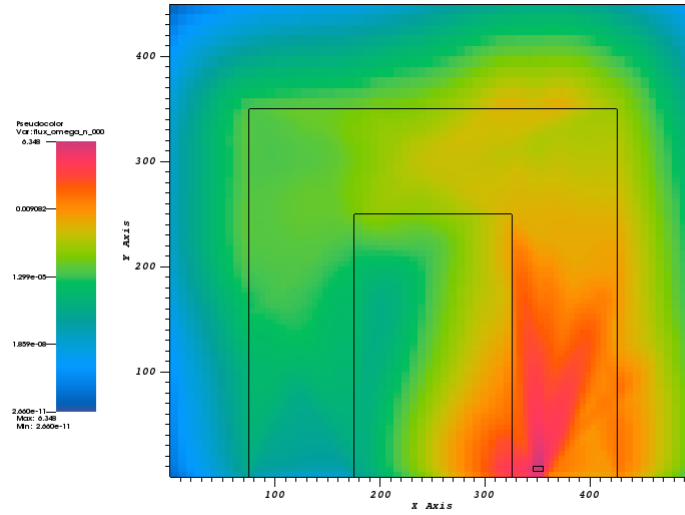
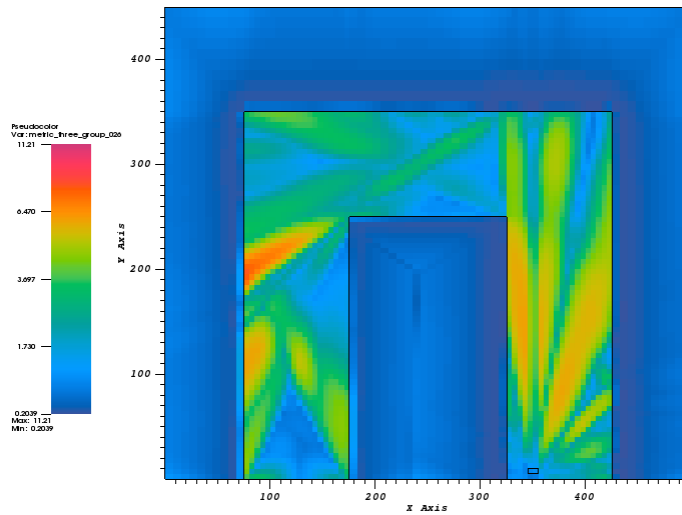
(c) Ω flux distribution, highest energy group

Figure 4.32: Flux distributions at problem midplane for U-shaped corridor. Distributions shown are for the highest energy group. In this problem the forward source and detector region are located in different z-plane locations.

The Ω -flux shown in Figure 4.32c does not attempt to force particles through the shield like the contribution flux, nor does it have as substantial of ray effects as the adjoint scalar

flux distribution. However, the ray effects in this variant are not completely mitigated. There appears to be a cone of particles extending into the u-bend that are of greater importance than the other regions near the detector. This is a clear effect of the forward flux distribution. However, the region just to the right of the detector location is of possible consequence. Between the detector and directly to the right, the flux decreases in magnitude more than two orders of magnitude. It is possible that the large gradient in importance could be adversely affecting the time achieved by the Ω methods for this problem.



(a) M_3 distribution, visualized in plane containing detector

Figures 4.33a and 4.33b show the anisotropy metrics for the u-shaped bend. Figure 4.33a shows the M_3 distribution, which as one may recall is the ratio of the contributon maximum angular flux to the contributon average angular flux in the cell. M_4 , which is visualized in Figure 4.33b, divides M_3 by the ratio of the maximum to average adjoint angular fluxes.

Comparing these two figures we can identify the effect of this normalization on the anisotropy metrics. Beginning with the M_3 distribution plot in Figure 4.33a, it is clear that we still observe the secondary ray effects in the flux anisotropies that were observed in the labyrinth problems. On the right side of the u-bend, we observe ray effects in the anisotropy that are likely from the adjoint flux distribution. On the left side of the bend we observe oblong circular distributions of anisotropy. These are more likely to be from particles emanating forward source distribution. The contributon flux anisotropies are much stronger in the air channels than in the concrete shield, as we would expect. In the shield immediately bounding the air, we observe a fairly isotropic flux distribution, but as particles reach closer to the edges the anisotropy increases slightly.

The M_4 distributions shown in 4.33b show how certain features of the anisotropy are removed when using the control adjoint angular flux. In particular, the shield region becomes

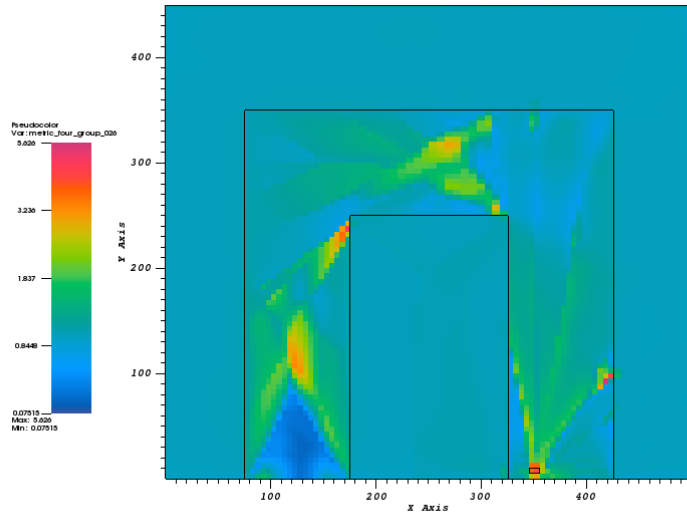
(b) M_4 distribution, visualized in plane containing detector

Figure 4.33: Anisotropy metrics plotted at problem midplane ($z = 55$) for U-shaped corridor. Energy group shown is for lowest energy.

completely normalized, meaning that the isotropy in the contribution flux matches that of the adjoint flux. The air regions are where real and substantial differences occur. In particular, we see peaks in the anisotropy where the forward and adjoint fluxes meet. At the top of the bend, the adjoint and forward fluxes have scattered relatively few times and thus generate a high anisotropy in the contribution flux.

These anisotropy plots illustrate how in certain regions the flux anisotropy may be very high. Further, they show regions where the fluxes strongly interact with one another. In addition to helping to quantify the effectiveness of the method, they reveal interesting features of the solution that may not be obvious using standard flux figures.

4.2.6 Shielding with Rebar

The problem with rebar embedded both in the x- and y- directions in concrete has results summarized in Tables 4.17 and 4.18. Figures 4.34a and 4.34b show the results obtained by the track length tally in CADIS, CADIS- Ω and the nonbiased analog Monte Carlo.

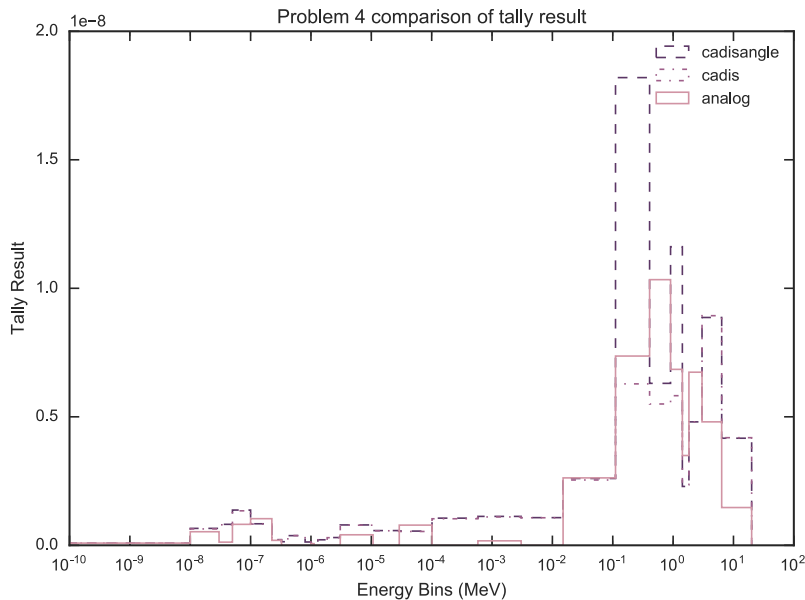
The FOM results for the rebar-embedded concrete show that this is a very poor problem for CADIS- Ω , in general. CADIS- Ω has lower FOMs than CADIS in all measures. CADIS- Ω spends fractionally over five—both deterministically and in Monte Carlo—the transport time that CADIS does. Further, CADIS- Ω has poorer FOMs in both the tally average and maximum relative error than the nonbiased analog. This is due to CADIS- Ω requiring nearly 30x longer to run Monte Carlo than the nonbiased analog.

	CADIS		CADIS- Ω		analog
	MC	MC _{hybrid}	MC	MC _{hybrid}	MC
tally avg	1.15	1.09	0.0136	0.0127	0.948
max RE	0.0345	0.0327	0.00117	0.00109	0.0186
min RE	235	223	199	186	—
time (mins)	328	346	1.55e+03	1.66e+03	53.8

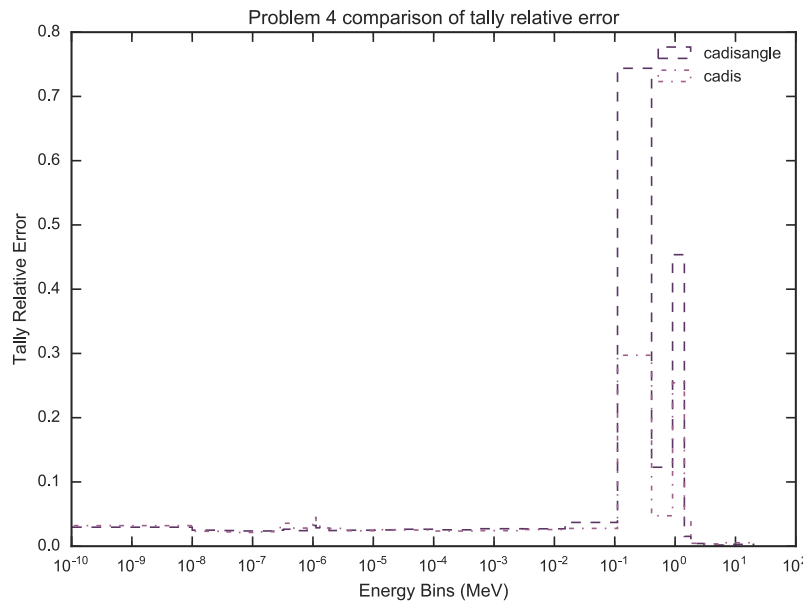
Table 4.17: Figure of Merit comparison between methods for rebar-embedded concrete.

		CADIS	CADIS- Ω	analog
		time (minutes)		
MCNP time	total	327.81	1550.54	53.82
deterministic time	advantg_time	0.28	0.29	—
	denovo_time	17.70	105.09	—
	dispose_time	0.03	0.41	—
	omega_time	0.00	2.05	—
	total	17.98	107.43	—
wall time		345.79	1657.97	53.82

Table 4.18: Detailed timing results for rebar-embedded concrete.



(a) Tally results comparison.



(b) Tally relative error comparison.

Figure 4.34: Tally result and error for rebar-embedded concrete, monodirectional Monte Carlo source

Figure 4.34a shows that the tally results for the rebar-embedded concrete do not generally agree between any method. CADIS and CADIS- Ω have better agreement with each other than with the nonbiased analog, but at high energies their results differ significantly. However, in comparing their relative errors in Figure 4.34b, the large discrepancy in their results is explained by the very high relative errors in this region. As with the U-shaped air corridor, neither method achieves satisfactory relative errors below 0.10 in high energy bins. However, both methods achieve comparatively good relative error results in energy bins below 10^{-1} MeV.

It is interesting that this problem appears to perform far more poorly than the steel beam in concrete. At this point, we must ask ourselves why a similar, but slightly more complex problem would have such substantively different results in the FOMs. This problem is undoubtedly difficult for both CADIS and FW-CADIS, but why does CADIS- Ω have such a poor performance in high energy bins which are usually more anisotropic than lower energy bins.

Section 4.1.2 described that flux anisotropy can be induced by the problem materials, geometry, or the source definition. Three of the characterization problem have monodirectional sources: the steel beam in concrete, the rebar-embedded concrete, and the nuclear medicine therapy room. At this point in the work it was discovered that ADVANTG does not support monodirectional sources, though it has in the past. As a result, the importance

maps generated by ADVANTG/Denovo automatically use an isotropic source distribution. However, the Monte Carlo input is not edited to reflect an isotropic source. As a result, the importance map does not match the physics in the problem.

This difference in the source definition did not affect the steel bar in concrete problem (Section 4.2.4) because the source comprises the entire wall at $x = 0$. However, both the rebar and the medical therapy room will have importance maps that do not match the physics of the defined Monte Carlo input. The results presented in Tables 4.17 and 4.18, as well as Figures 4.34a and 4.34b reflect a Monte Carlo simulation with a monodirectional source and a deterministic solver providing an importance map with an isotropic source. This, though unexpected, issue provides an opportunity for us to investigate the Ω -method's sensitivity to incorrect importance maps.

Tables 4.19 and 4.20 show the FOM and timing results for a Monte Carlo simulation with an isotropic source defined. Note that the deterministic times in Table 4.20 match those in Table 4.18. This is because the lack of support for monodirectional sources results in a deterministic solution that is agnostic to the defined Monte Carlo source. Figures 4.35a and 4.35b show the tally results and relative error for the case where the Monte Carlo and deterministic sources are consistent.

	cadis		cadisangle		analog	
	MC	MC_adjusted	MC	MC_adjusted	MC	MC
tally avg	80.5	45.6	260	132	0.257	
max RE	1.52	0.862	1.31	0.662	0.109	
min RE	221	125	214	109	—	
time (mins)	23.5	41.4	111	218	9.15	

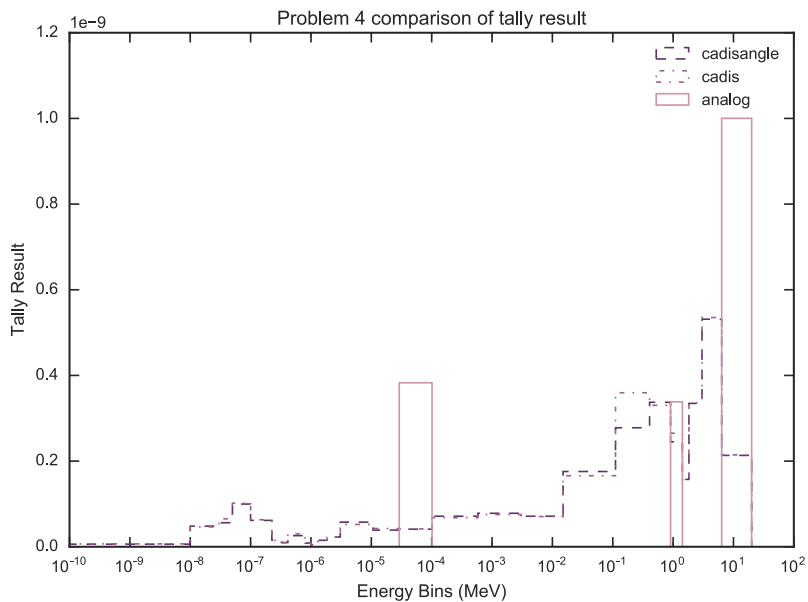
Table 4.19: Figure of Merit comparison between methods for rebar-embedded concrete, isotropic Monte Carlo source.

The results in Table 4.19 are quite different than those in Table 4.17. The time for both CADIS and CADIS- Ω is reduced by more than an order of magnitude. In the original run of this problem, CADIS- Ω took 1,500 minutes to converge. Here that time is reduced to 111 minutes. Further, the tally average and tally maximum RE FOMs change between the tables by several orders of magnitude. This means that in addition to the shortened time reducing the FOMs, the relative errors also improved between the monodirectional and isotropic point source variants.

The tally results between Figs. 4.35a and 4.34a, show that having a consistently defined source between deterministic and Monte Carlo transport results in a closer tally result between CADIS and CADIS- Ω . This is also confirmed in Figs. 4.35b and 4.34b. In the original version of this problem CADIS- Ω 's relative errors at energy bins $> 10^{-1}$ were more than twice that of the REs achieved by CADIS. Interestingly, we see the opposite occur in the isotropic source definition. In figure 4.35b, CADIS has some energy bins with relative errors almost

		cadis time (minutes)	cadisangle time (minutes)	analog time (minutes)
MCNP time	total	23.47	110.67	9.15
deterministic time	advantg_time	0.28	0.29	—
	denovo_time	17.70	105.09	—
	dispose_time	0.03	0.41	—
	omega_time	0.00	2.05	—
	total	17.98	107.43	—
wall time		41.45	218.10	9.15

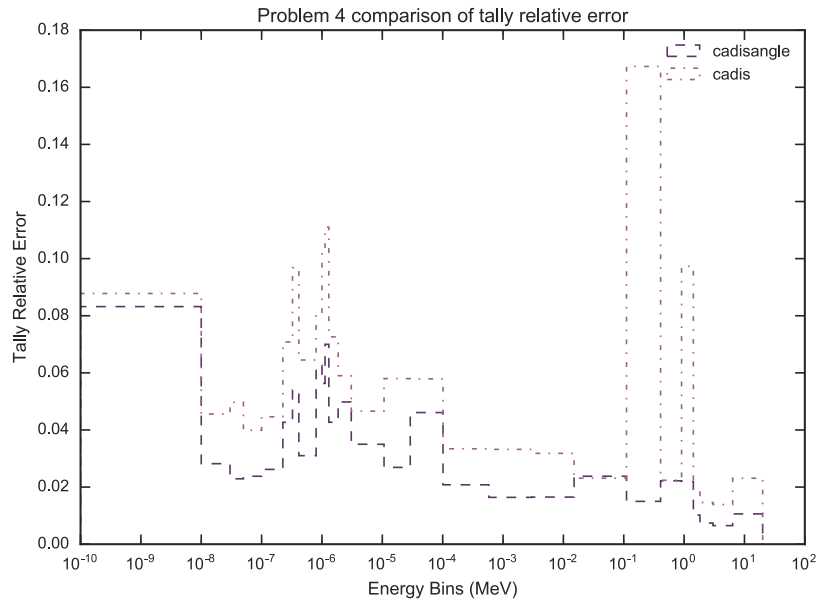
Table 4.20: Detailed timing results for rebar-embedded concrete, isotropic Monte Carlo source.



(a) Tally results comparison.

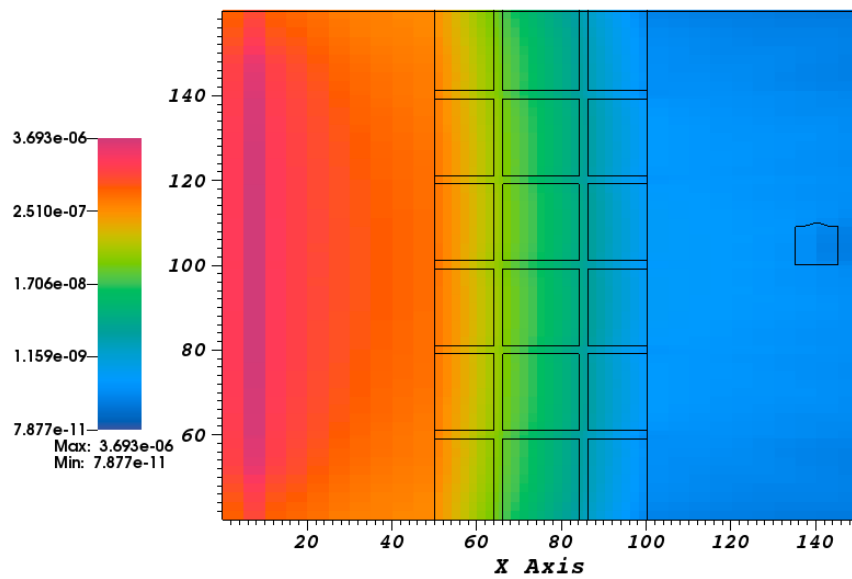
9x thos of CADIS-Ω in the same bin. However, it is worth noting that the scales between these two problems is very different. The highest RE achieved by CADIS in Figure 4.35b is lower than either CADIS or CADIS-Ω’s RE in the monodirectional problem.

The plots in Figure 4.36 show the highest energy flux for the foward problem in Fig. 4.36a and the lowest energy Ω-flux distribution for the Ω-method in Figure 4.36b. Figure 4.36a clearly shows that the plate source on the left side of the problem is isotropically emitting particles. The Ω-flux in Figure 4.36b shows the preferential flowpaths for particles through the steel at low energies. Recall that the deterministic flux distributions will not change between the isotropic and monodirectional source definitions in Monte Carlo, so these



(b) Tally relative error comparison.

Figure 4.35: Tally result and error for rebar-embedded concrete, isotropic Monte Carlo source



(a) Forward flux distribution, highest energy group

figures and any map of the metric distributions in the problem are the same regardless of the Monte Carlo source definition.

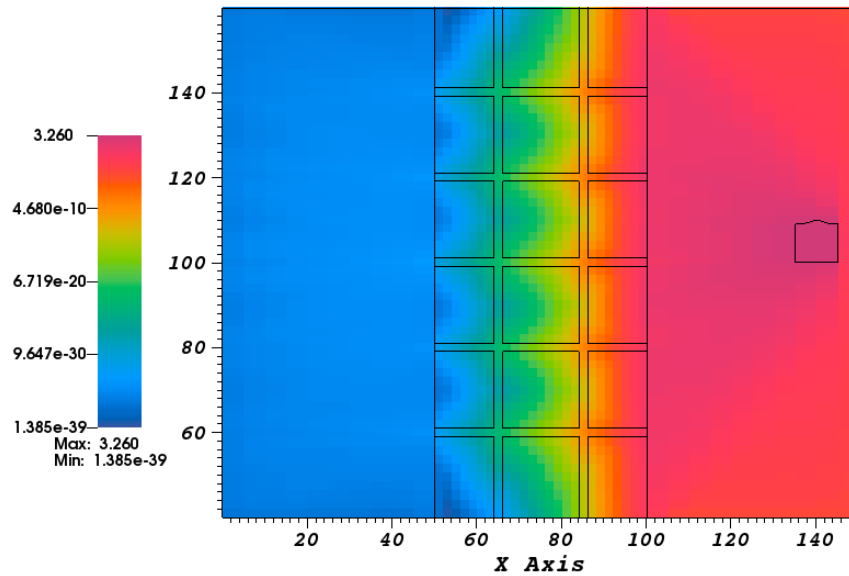
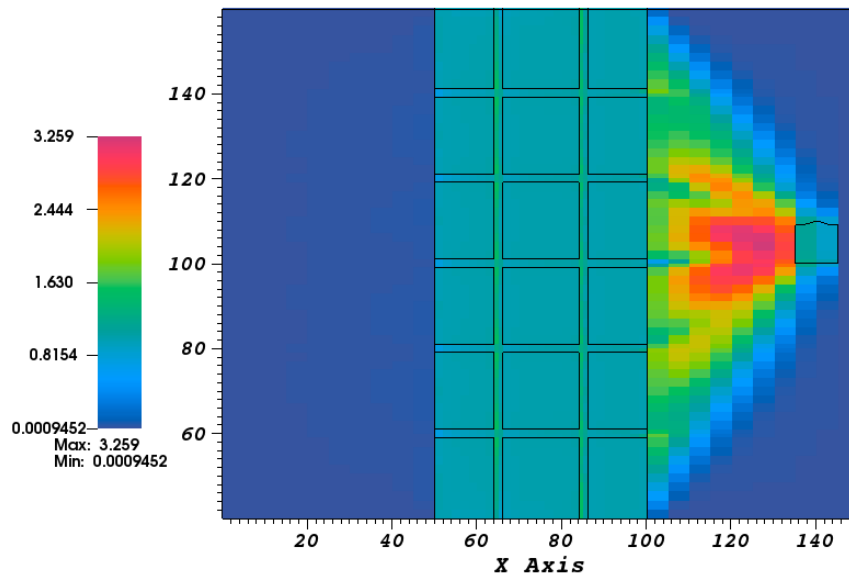
(b) Ω flux distribution, lowest energy group

Figure 4.36: Forward and Ω -flux distributions, rebar embedded in concrete. Slice is located at $y = 100$ centimeters

(a) M_2 distribution, lowest energy group.

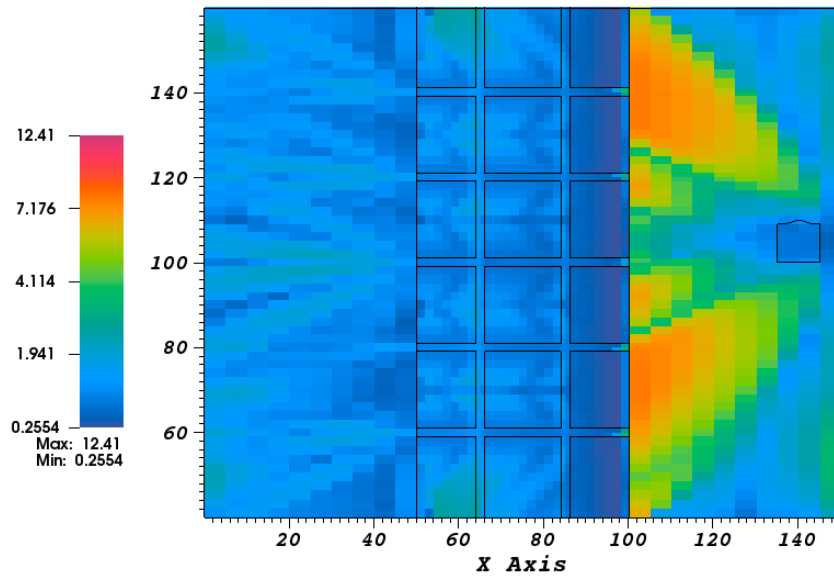
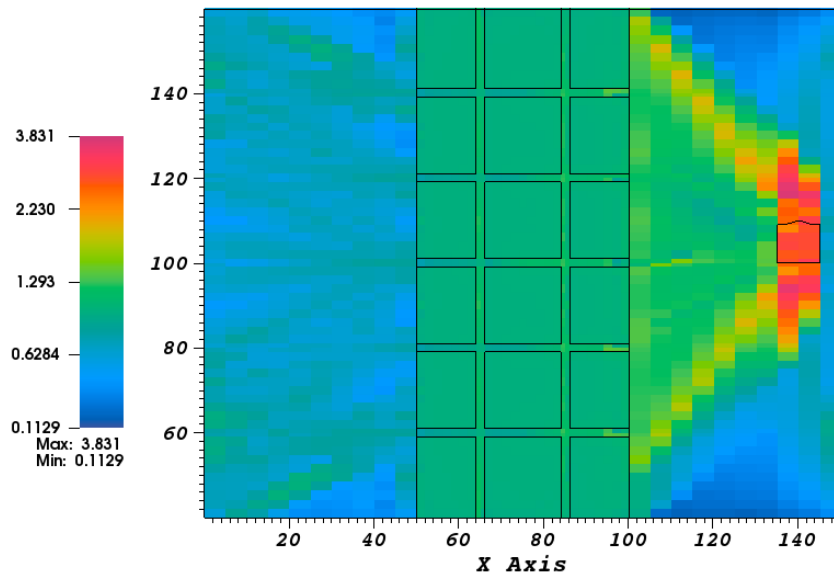
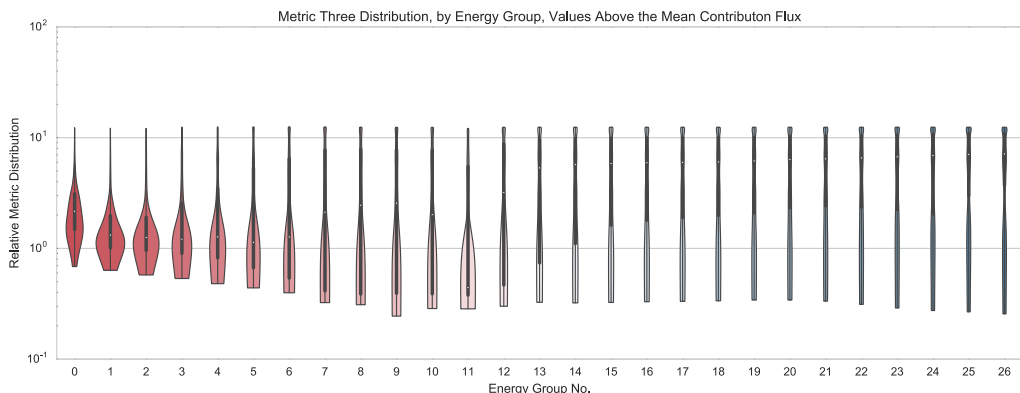
(b) M_3 distribution, lowest energy group.(c) M_4 distribution, lowest energy group.

Figure 4.37: Metric distributions for rebar-embedded concrete. Slice at $y = 100$ centimeters. Lowest energy group distributions shown.

The subfigures of 4.37 show the M_2 , M_3 , and M_4 distributions for the lowest energy group for the rebar problem. Recall that the M_2 distribution directly compares the Ω and adjoint scalar fluxes. Figure 4.37a shows that the biggest deviations of the Ω -flux from the adjoint are near the adjoint source. This was similarly observed in the steel beam problem variants. The regions of concrete are the same between CADIS and CADIS- Ω , but the rebar support structure shows that the Ω flux has a slightly higher importance for these regions. Glancing back towards the adjoint source region, the flux importances can be seen separating into fingers that line up with the concrete blocks in the problem.

The M_3 distribution of 4.37b shows the anisotropy of the contributon flux for this problem, and the M_4 distribution in Figure 4.37c shows the result of normalizing this anisotropy by the adjoint anisotropy. In the concrete blocks of Figure 4.37b some interesting anisotropy distributions occur closer to the forward source. As with Figure 4.37a, we can see the anisotropies separate into fingers that line up with the concrete blocks. On the adjoint source side of the shield, the anisotropies are the highest right next to the concrete blocks. On the forward source side of the shield, the areas next to the blocks are the least anisotropic. When the metric is normalized by the adjoint in Figure 4.37c, some of the anisotropy effects are mitigated, meaning that the adjoint angular flux is the driving force behind the features that we observed in Figure 4.37b. However, on the forward source side of the shield there are strong anisotropies that line up with each of the metal rebar structures.



(a) M_3 distributions rebar embedded in concrete, filtered above the mean contributon flux.

While the metric distributions and the flux maps do not differ between the Monte Carlo source types, the scatterplots of I_{RE} and I_{FOM} will. Figure 4.38a shows a violin plot of the M_3 distributions for this problem. Figure 4.38b shows I_{RE} for the problem with a monodirectional Monte Carlo source trended against several metric values for M_3 values using the mean contributon flux filtering algorithm. Figure 4.38c shows these trends for the problem with an isotropic Monte Carlo source using the mean contributon flux filtering algorithm.

After inspecting the metric distributions against I_{RE} and I_{FOM} , no distinct trends were observable with any metric and either improvement factor. Because M_3 had the best trends,

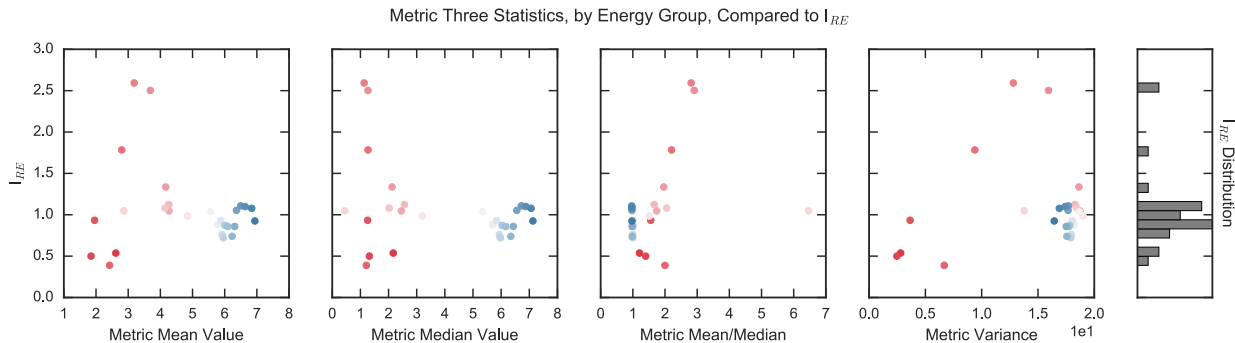
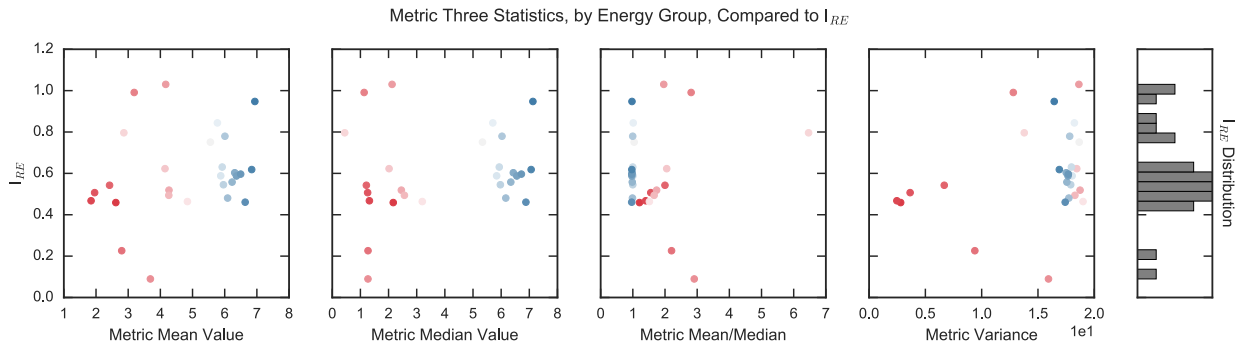
(b) I_{RE} for M_3 for rebar embedded in concrete, monodirectional Monte Carlo source.(c) I_{RE} for M_3 for rebar embedded in concrete, isotropic Monte Carlo source.

Figure 4.38: M_3 distribution and I_{RE} scatterplot for rebar-embedded in concrete. Values of M_3 have been filtered to be from cells that are above the contribution mean value.

it is included in the plots of Figure 4.38.

Figure 4.38a shows that low energy cells have a large spread but no centering value. There exist some very anisotropic cells at low energy groups, but there exist also some very isotropic cells. Conversely, in high energy groups the metric distribution has a very clumped distribution of values where the contribution max angular flux is higher than the average contribution angular flux in the cell.

Using values that can be computed from the distributions shown in Figure 4.38a, the relative error improvement between CADIS- Ω and CADIS can be plotted as shown in Figs. 4.38b and 4.38c. The x-values between each of these figures will be the same, but the y-ordinate values will differ as a result of their differing Monte Carlo source distributions.

In general Figure 4.38b shows there exist many energy bins where CADIS- Ω achieves a poorer relative error than CADIS. The bins where the comparative error is the worst is in intermediate energy regions. At low energy regions the relative errors are comparable, but as shown in the timing table, the FOM will be much lower for CADIS- Ω . There does appear to be a slight trend in I_{RE} with the ratio of the metric mean to the metric median

and with the metric variance. As with the steel beam problem, this shows that the metric distribution is a better predictor of the improvement in the relative error than the metric average or median value. However, these trends are not strong, and it would be difficult to predict the performance of a similar problem based on metric distributions. Comparing the results of Figure 4.38c to Figure 4.38b, some of these observations change with the isotropic source definition. First, CADIS- Ω performs better than CADIS uniformly in all energy bins. Next, there exists no trend in the metric distribution and I_{RE} . We cannot conclude that any version of the M_3 distribution can predict whether the Ω method will improve convergence for this problem.

It is possible that the filter matrix is not fine enough for this particular problem to pull out metric values of high importance, but even values filtered out above the mean contribution flux did not have strong correlations. However, with the cutoffs appearing in the distributions of 4.38a, choosing too high of a filter value may also remove much of the metric distribution.

Both CADIS and CADIS- Ω improve in the relative errors that they achieve as a result of having a source distribution that matches between the Monte Carlo and deterministic runs. As a result, the comparison between isotropic and monodirectional sources in this problem shows that having an importance map that does not match the problem will slow down convergence. Further, we can conclude that CADIS- Ω is more sensitive to having an importance map that doesn't match the Monte Carlo. This may be because the larger gradients in importance exacerbate splitting and rouletting from an unexpected source.

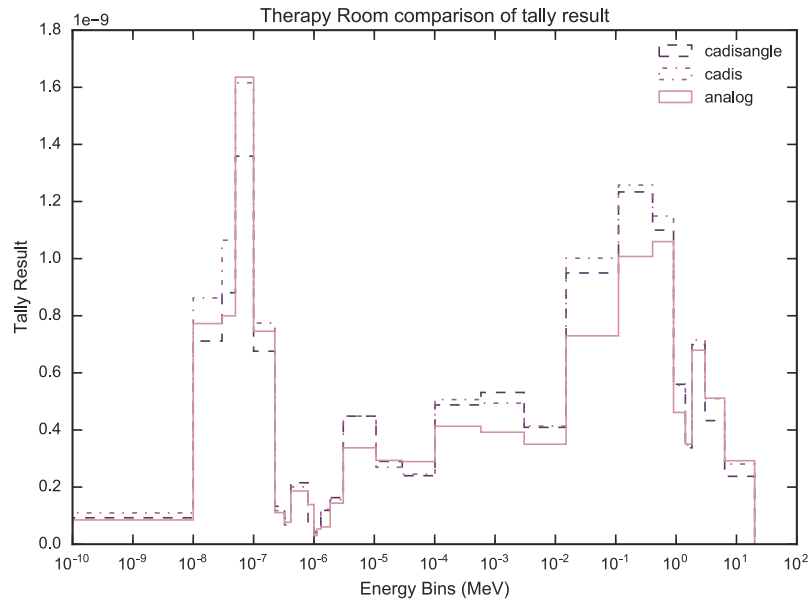
4.2.7 Therapy Room

The problem with a simplified representation of a nuclear medicine therapy room has FOM summarized in Table 4.21. Figures 4.39a and 4.39b show the results obtained by the track length tally in CADIS, CADIS- Ω and the nonbiased analog Monte Carlo. Note that the results for this problem had issues with reported times for the deterministic run, so the adjusted Monte Carlo (FOM_{hybrid}) is not reported and the timing table is not reported.

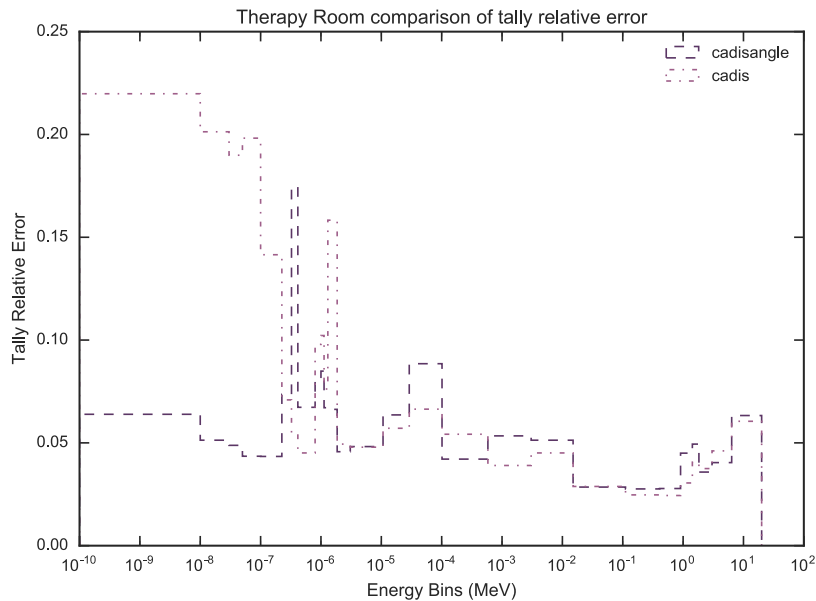
	cadis		cadisangle		analog
	MC	MC_adjusted	MC	MC_adjusted	MC
tally avg	5.81	5.71	106	8.34	2.81
max RE	0.463	0.455	0.822	0.0649	0.0136
min RE	37.6	37	32.9	2.6	0.793
time (mins)	44.7	45.4	39.9	506	248

Table 4.21: Tally relative error comparison between methods for simplified medical therapy room, Monte Carlo monodirectional source.

The therapy room with a monodirectional Monte Carlo source is a problem where CADIS- Ω performs fairly well when compared to CADIS and the nonbiased analog Monte Carlo.



(a) Tally results comparison.



(b) Tally relative error comparison.

Figure 4.39: Tally result and error for simplified medical therapy room, monodirectional Monte Carlo source.

For the Monte Carlo runtime-exclusive FOMs, CADIS- Ω achieves better FOMs than CADIS and the nonbiased analog in both the tally average relative error and the tally maximum relative error. This is likely due to a softening of the importance map as a result of the concrete walls surrounding the therapy room. As a result, reflecting forward and adjoint particles decrease the strong gradient that exists in other problems, like the exit of the single turn labyrinth.

For this problem, CADIS- Ω achieved similar relative errors to CADIS for intermediate- and fast- energy bins. However, for low energy bins CADIS performed poorly and CADIS- Ω achieved satisfactory relative errors. These low energy bins are the only ones where CADIS- Ω really substantially outperformed CADIS. In a similar problem it would be advantageous to use CADIS- Ω as a method, but with deterministic runtime incorporated it may still be worthwhile to run with CADIS instead. If a user desires a tally with low energy bins exclusively, CADIS- Ω will be the advantageous method.

	cadis		cadisangle		analog	
	MC	MC_adjusted	MC	MC_adjusted	MC	
tally avg	29.8	11.4	192	72.4	52.3	
max RE	0.829	0.316	3.51	1.32	0.292	
min RE	387	148	423	159	10.7	
time (mins)	287	753	281	747	91	

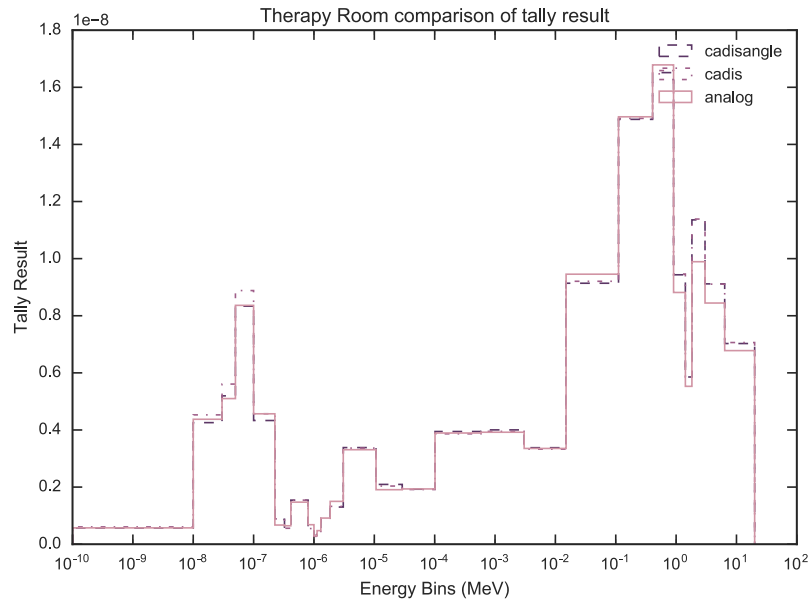
Table 4.22: Tally relative error comparison between methods for simplified medical therapy room, Monte Carlo isotropic source.

As discussed in Section 4.2.6, the monodirectional source distribution in Monte Carlo is not actually reflected in the importance map generated by ADVANTG. As a result, the results for the isotropic source are shown in Table 4.22 and Figure 4.40.

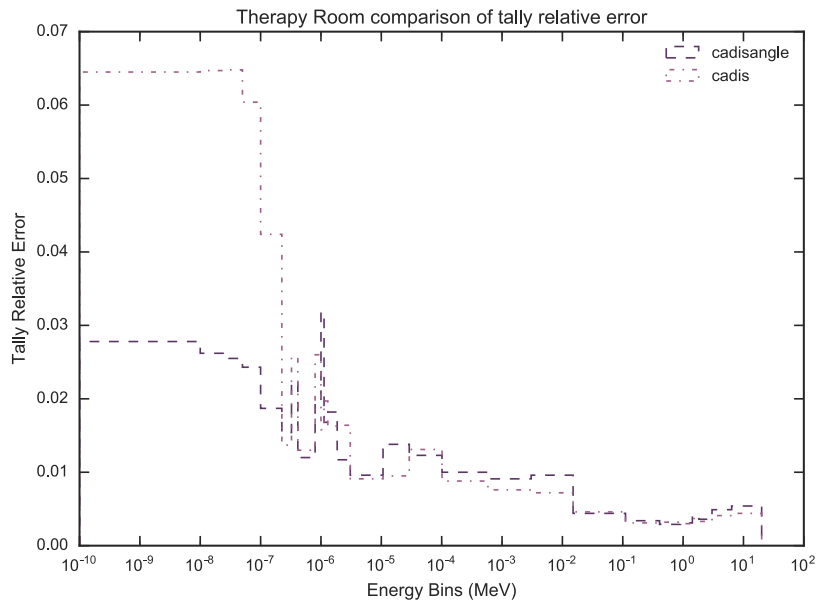
Comparing the results from Tables 4.22 and 4.21, the isotropic source definition does improve the FOMS achieved by CADIS, CADIS- Ω , and the analog Monte Carlo. The minimum relative error FOMs see a factor of 10 improvement for both CADIS and CADIS- Ω . The time to run the biased problems is quite a bit longer, which is likely due to the placement of the source in the problem. Because the monodirectional source forced particles into the water phantom, they were sent into a region with relatively little variation in the flux. The Ω -method, in particular, avoids a region with very strong preferential flow. Avoiding splitting and roulette as a result of crossing paths with large variations in the flux would allow the problem to run faster.

Despite the longer runtimes, CADIS and CADIS- Ω both achieve better FOMS in every measure by changing the source definition. Again, the effects of using the wrong importance map are reflected in longer runtimes for both problems.

Figure 4.40 shows the tally result and relative error for the isotropic source defined in Monte Carlo. Comparing the tally results of the isotropic source in Figure 4.40a to the



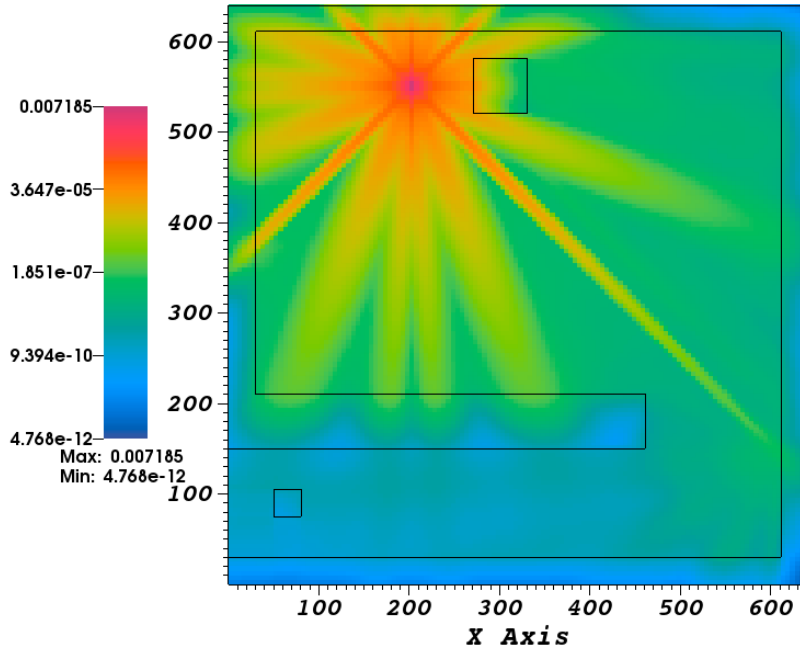
(a) Tally results comparison.



(b) Tally relative error comparison.

Figure 4.40: Tally result and error for simplified medical therapy room, isotropic Monte Carlo source.

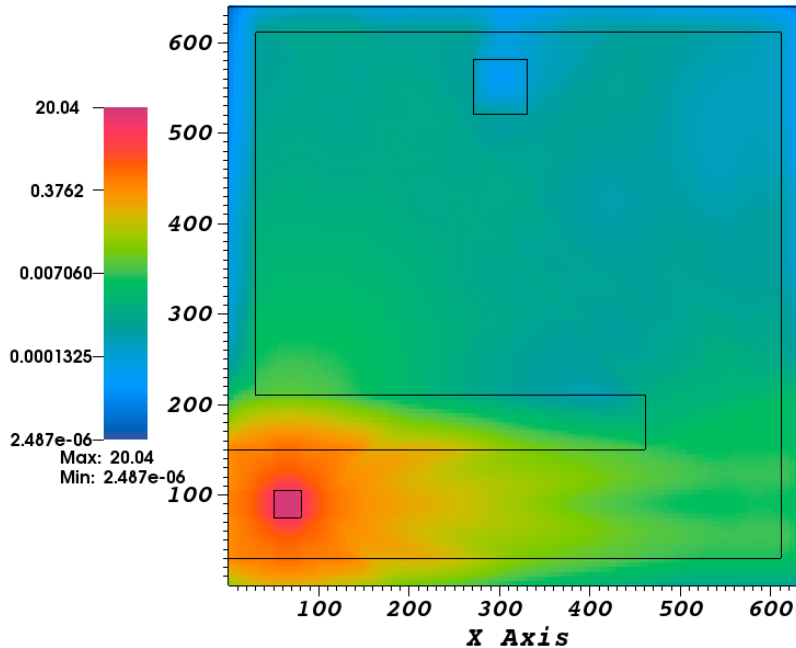
monodirectional in Figure 4.39a, we can see that the results between all three methods agree better for the isotropic source distribution. The shapes of the relative error compare similarly between Figs. 4.40b and 4.39b, however the relative errors achieved by CADIS and CADIS- Ω are far smaller in the isotropic case. In both source definitions, CADIS struggles transporting low energy particles more than intermediate- or high-energy particles. CADIS- Ω handles these energies better, but it struggles in the lower-energy resonance regions slightly more than CADIS. As a result, there is some tradeoff with effectiveness for each method.



(a) Forward flux distribution, highest energy group

The flux maps for the therapy room are shown in Figure 4.41. Figure 4.41a shows the forward flux for the highest energy group. This figure has very strong ray effects that dominate the flux behavior near the water cell and near the forward source. Over just a few centimeters, the forward flux varies two- to three- orders of magnitude. The wall to the bottom right of the figure shows some secondary ray effects that occur after scattering. This is much more subtle than near the forward source, but there are three groupings of flux direction after this scatter, which may be magnified in the Ω -flux by the adjoint.

Figures 4.41b and 4.41c show the adjoint and Ω -fluxes for the therapy room problem. Unlike the labyrinth variants, where the Ω methods softened ray effects, there exist much stronger ray effects in the Ω -flux map for the therapy room. This is because the ray effects are primarily from the forward flux, which does not affect the standard adjoint flux whatsoever. However, the integration of the forward and adjoint in the Ω calculation causes some of the forward ray effects to be carried over into the adjusted adjoint. A compounding factor to this



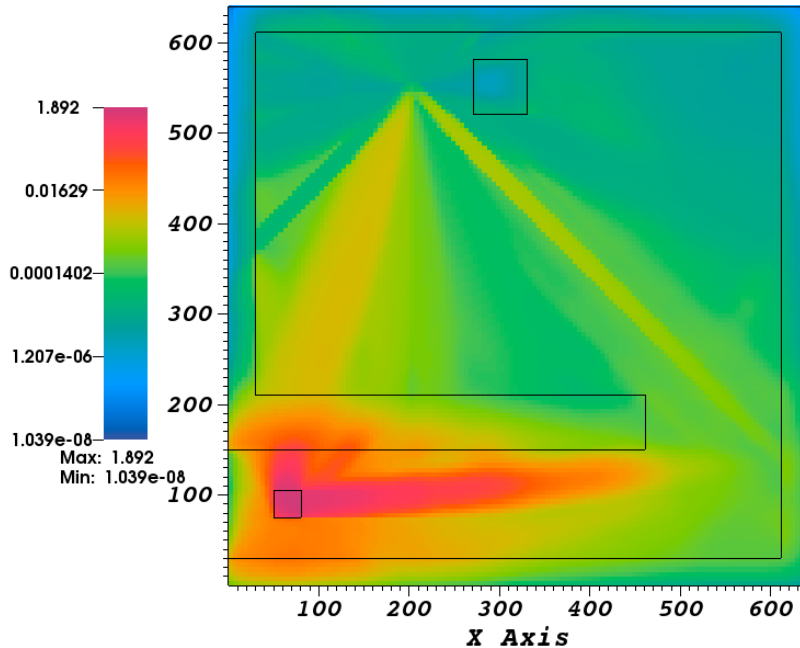
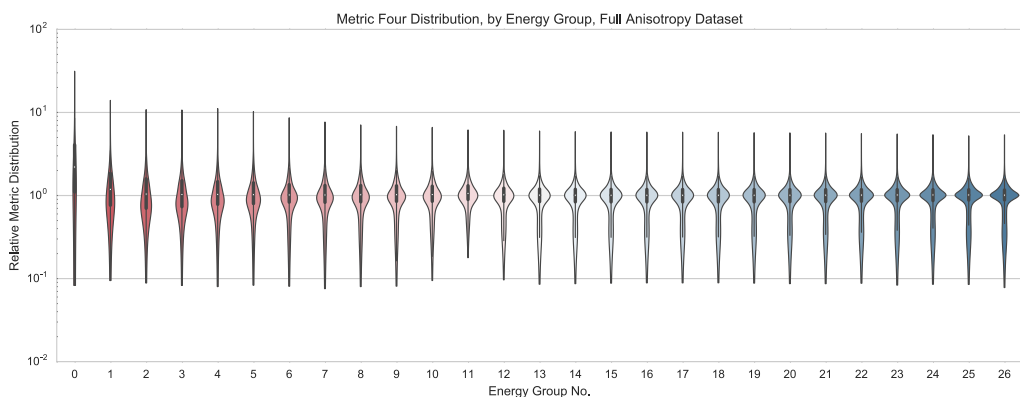
(b) Adjoint flux distribution, highest energy group

is that the adjoint particles travel in exactly the opposite direction to the forward particles at the region where the hallway meets with the room. It was discussed previously that the contribution flux will be magnified if forward and adjoint particles are travelling in opposite directions. Not only is this the case in the therapy room, but they are travelling in opposite directions down a ray effect. This magnifies the ray effect in the problem, so there is a tight band of particle travel diagonally across the Ω problem.

Figure 4.42 shows the M_4 distribution and the trends of I_{RE} for different values of the M_4 distribution for both the isotropic and monodirectional variants of the therapy room. These figures do not use a filtering algorithm. This is because this particular problem was run on a slightly earlier version of ADVANTG that did not output the angle-integrated contribution fluxes. As a result, the values used for the filter matrix are not accessible, and filtering cannot be used in this analysis. Future studies of this particular problem should compare the effects of the filtering algorithms of the distributions of Figs. 4.42b and 4.42b.

Figure 4.42a shows the full violin plots by energy group for the therapy room. Here we see that the lower energy groups have values clustered around a value slightly above 1. Violins in intermediate to high-intermediate energy groups have a lower mean value than the low energy violins, but their distribution tends to broaden. The broadening of the distribution is particularly evident for energy group violins valued ≤ 8 .

Figures 4.42b and 4.42c show the effect that this distribution has on I_{RE} for both the monodirectional and isotropic variants of the problem. Again, none of the anisotropy metrics

(c) Ω -flux distribution, highest energy groupFigure 4.41: Flux distributions at $z = 150$ centimeters for radiation therapy room.(a) Unfiltered M_4 distributions medical therapy room.

showed a strong trend for I_{RE} or I_{FOM} with any distribution, so the best figure was included here. Recall that a value below unity for these figures indicates that CADIS- Ω achieved a lower relative error in that bin. In both figures CADIS- Ω has roughly half of its values above unity and half below. There are some very low energy bins in which CADIS- Ω far outperforms CADIS, but then there are intermediate energy groups that CADIS- Ω 's performance falters.

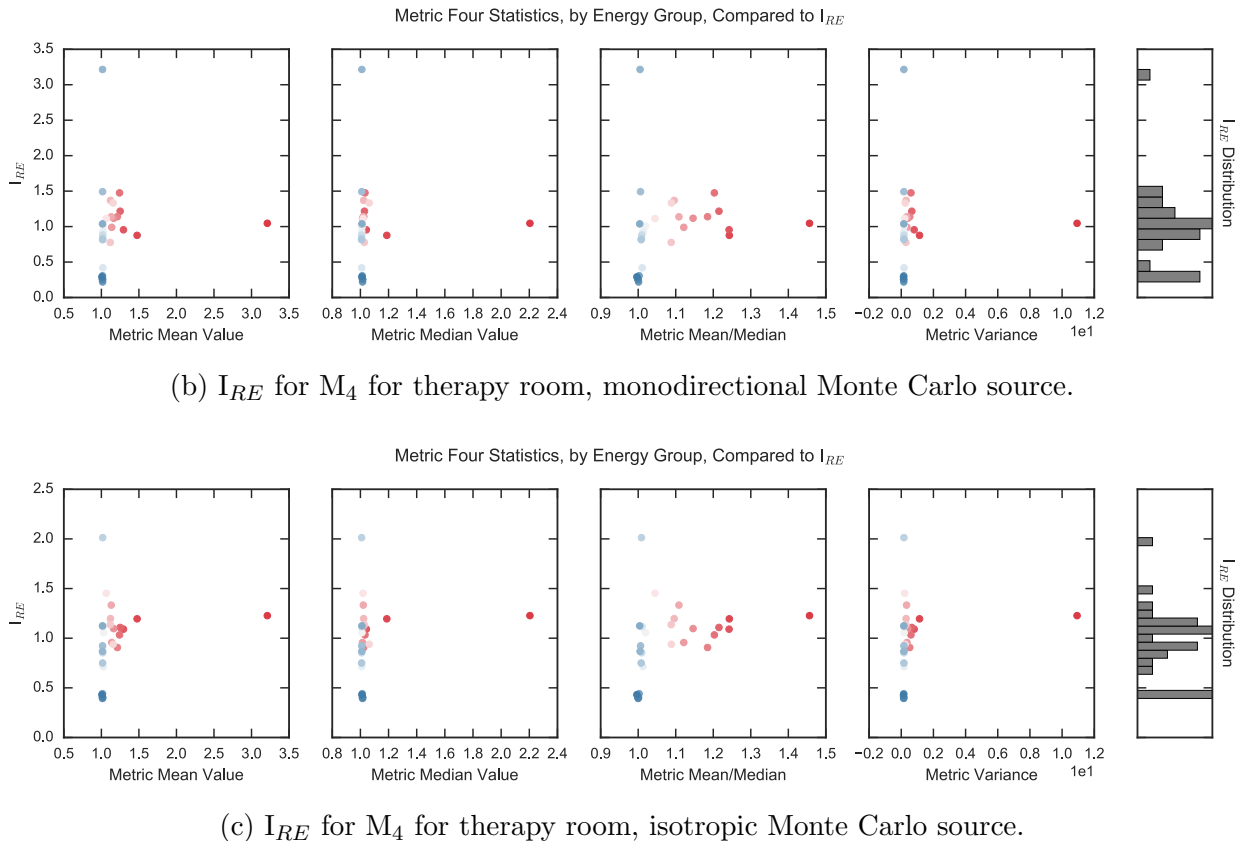


Figure 4.42: M_4 distribution and I_{RE} scatterplot for medical therapy room.. Values of M_4 have not been filtered with a filtering algorithm.

Neither figure shows a particular trend, but the metric skew does appear to be the subplot most closely resembling a trend.

In comparing Figure 4.42 to 4.38, this problem does not show as significant of a change in I_{RE} with respect to changing source definitions. This means that the ratio of relative errors between CADIS and CADIS- Ω remains the same, despite both achieving far lower relative errors overall in the isotropic case. That means, for this problem, CADIS and CADIS- Ω are both equally sensitive to a mismatch in importance map. This could be a result of the large fraction of air in the problem, which dominates the behavior of both methods. Conversely, the rebar problem required both CADIS and CADIS- Ω to sample frequently in the center of the problem, so the effects of mismatching maps was more isolated from other effects.

4.3 Sensitivity to Deterministic Parameter Choice

At this point in the Ω -method characterization, it has been shown how the Ω -methods behave in problems with differing geometries and materials. However, each of the problems presented

in Section 4.2 was run with the same deterministic calculation parameters. While the angular flux may have differed in these problems due to differences in the way the problems were constructed, it did not vary due to deterministic solver choices. Some deterministic solver choices will change the angular fluxes used to calculate the Ω -flux. Consequently, this may affect the behavior of the Ω -methods. This section will explore the effects of deterministic solver choices on the Ω -method's performance.

Section 4.2 showed that the Ω -methods have a strong weakness to “thin” materials, as CADIS and FW-CADIS do. Recall that a “thin” material is characterized by a low density, and thus a low macroscopic cross section, or interaction probability. In a pure streaming problem, the particle flux will decrease by a factor of r^2 from the source and never interact. In a thin material, a particle may stream several centimeters before interacting. As a result, the importance of a particle, which is related to the adjoint- or omega-flux, may vary several orders of magnitude over a mean free path of travel distance. At a collision, the particle then requires several orders of magnitude of sampling events.

The Ω -method's weakness to “thin” materials was confirmed by running the steel beam problem with air and concrete in the geometric location of the steel beam. In the “thin” material air version, CADIS- Ω performed poorer than CADIS. This was a strong contrast to the same geometric configuration with a steel beam, where CADIS- Ω outperformed CADIS. The success of CADIS- Ω in this problem also showed that the incorporation of the Ω -flux into a problem with materials with very different moderating properties but both with high probabilities of interaction, improves the performance of the Ω -methods beyond CADIS or the nonbiased analog.

Due to CADIS- Ω 's superior performance to CADIS in the problem with a steel beam in concrete, this is the problem that will be used to characterize CADIS- Ω 's sensitivity to deterministic parameter choice. In this section, the effect of deterministic solver choices on the performance of the Ω methods will be investigated. In particular, we are interested in how parameters that influence the angular flux will affect the performance of the Ω -methods. By using the same problem with differing solver options, the effect of solver options can be isolated from the material and geometric effects. By doing so, we seek to determine how resilient the Ω -methods may be to using low-fidelity solver options, how different the sensitivity of the Ω -methods are to solution quality when compared to CADIS, and how varying angular parameters may speed up or slow down the time to a desired solution. By quantifying these effects, we can determine the best parameter selection for the Ω -methods for this type of problem.

4.3.1 Parametric Study Description

The angle sensitivity parametric study will cover the subset of computational parameters that are most likely to influence the Ω method's solution. Because the Ω -flux is calculated from an angular integration of the forward and adjoint flux, calculation parameters that are most likely to influence the angular flux solution are the variables that will be perturbed. The two parameters that will be studied are the quadrature order and the P_N order.

The quadrature used in a deterministic solver is used to discretize the problem in angle. Quadrature options are split into two separate selections: the quadrature set or type, and the quadrature order. Because the Ω -methods require rotational symmetry, only quadrature sets that have rotational symmetry (generally these are triangular quadrature sets) can be used with the Ω -methods. In ADVANTG/Denovo, the triangular quadrature sets are: linear-discontinuous finite element, level-symmetric, and quadruple range. As discussed previously, quadruple range is selected as the ADVANTG default because it has good properties and guarantees positivity in the flux. Different quadrature sets have separate properties and are a realm of study unto their own. Thus, we will vary only quadrature order and not quadrature type in this sensitivity study.

Quadrature orders specify how fine of a resolution the quadrature set will be. As quadrature order increases, the angular discretization becomes finer, and the size of the angular flux matrices increases. The Ω methods use angular flux values that are written to a file after a Denovo transport solve, which are then read into memory to compute the Ω -flux. We expect to observe much slower deterministic recorded times in T_{det} —and, by extension, T_{hybrid} —for high quadrature orders because of the I/O demand to read and write the angular flux values. This I/O demand will not be as extreme for standard CADIS, as the angular flux values are not written in that case. Recall that the ADVANTG default quadrature order is 10. The quadrature orders used for the sensitivity study aimed to choose orders surrounding this value. This resulted in quadrature orders 5, 7, 10, 12, 15, 17, and 20 being chosen for variations in this parameter.

The P_N order determines the fidelity of the scattering expansion. The availability of P_N orders is dependent on the cross section dataset that is being used. For the 27G19N cross section library, the P_N order extends to 5. As a result, P_N orders of 1, 3, and 5 are chosen for variations in this parameter.

While the P_N order does affect angular information in the problem, it will not change the size of the angular flux matrices. As a result, deterministic runtimes between differing P_N orders may vary, but not as significantly as they will in differing quadrature orders due to the lack of change in I/O requirements as P_N order changes.

Other deterministic parameters may influence the variance reduction parameters calculated by the Ω methods. The spatial discretization, while not a primary factor influencing the angular flux, still may affect the Ω -methods' performance. A finer energy group structure may also influence the Ω -method solution. Finer energy groups will more effectively reflect resonance regions in scattering and absorption. Scattering effects in certain energy regions will have angular dependence and, thus, may have a stronger effect on the angular flux than a coarser energy discretization. Because these particular solution effects do not directly influence the angular flux and angular effects will be difficult to isolate, they will not be included in the angular sensitivity parametric study.

Several factors in the deterministic calculation should not have a strong effect on the angular flux distribution. These include the spatial solver, the convergence criteria for the solvers, and the within group solver types. Because these factors should not influence the angular flux any more than any other part of the solution, they will also not be included in

this parametric study.

4.3.2 Quadrature Order

The results that will be presented in the next two subsections will be similar to those presented in Section 4.2. However, our goal is to see how changing deterministic parameter type affects the results in the tally region. With this in mind, the presentation of the results may be adjusted to more effectively show the effect each parameter has on influencing the Monte Carlo transport.

Table 4.23 contains the FOM results for each of the quadrature orders run in the parametric study. The results are grouped by FOMs calculated with the same relative error. The first three sections of the table pertain to different FOM values, and the last section of the table shows timing results for the standard Monte Carlo (T_{MC}) and the total walltime (T_{hybrid}) for the calculation.

In the tally average relative error subsection of Table 4.23, two strong dips in the FOM appear in the CADIS results at S_N orders 5 and 10, and a dip in the CADIS- Ω FOMs occur at S_N order 12. These dips are much larger relatively than in the maximum or minimum relative error subsections of the table. This indicates that for these particular quadrature orders, fewer particles contribute to the detector response across all groups. We can also see in the CADIS- Ω results that quadrature orders 10, 15 and 17 all have a similar FOM for the tally average relative error using the Monte Carlo runtime. However, the FOMs for the same quadratures do not decrease more significantly when using T_{hybrid} to calculate the FOM, as suggested in Section 4.3.1. This suggests that the increased deterministic runtime for I/O is offset consistently by the change in the FOM between quadrature orders for CADIS- Ω .

In this subsection of the table it is also notable that the oscillations between maximum and minimum FOM values is much larger for CADIS- Ω than for CADIS. For low quadrature orders, CADIS- Ω shows substantial improvement in the FOM, while CADIS remains somewhat constant (this is omitting the major dips in FOM values noted in the previous paragraph). At higher quadrature orders, however, CADIS- Ω 's performance is inverted and decreases with increasing quadrature order. CADIS, however, remains fairly constant in FOM for S_N orders 12 and above. Both methods far outperform the nonbiased analog Monte Carlo run.

The maximum relative error portion of the table also has several notable datapoints. For CADIS, the dips in FOM are still visible for S_N orders 5 and 10, but quadrature order 7 does not achieve the same high FOM as quadrature orders 12 and above as it does in the tally average subsection of the table. If the maximum relative error convergence is the limiting factor for the user, it appears that using any quadrature order above 10 is a good choice for CADIS. CADIS- Ω , conversely, has more varied results. No observable trend exists in the FOM with increasing quadrature order for CADIS- Ω . A dip in the FOM occurs at quadrature order 12, as it did in the tally average subsection of the table. This dip, like CADIS' dips, is not as significant as the dip in the tally average FOMs. Generally, CADIS has higher FOMs when using the maximum relative error as a success metric. In fact, the

only quadrature order where CADIS- Ω 's FOM is larger than CADIS' is at quadrature order 10.

	S_N order	CADIS		CADIS- Ω		analog
		MC	MC_{hybrid}	MC	MC_{hybrid}	
tally avg	S_N 5	683	677	1.81e+03	1.79e+03	
	S_N 7	2.55e+03	2.53e+03	2.46e+03	2.45e+03	
	S_N 10	669	659	2.96e+03	2.93e+03	
	S_N 12	2.46e+03	2.41e+03	187	183	1.39
	S_N 15	2.48e+03	2.42e+03	2.98e+03	2.92e+03	
	S_N 17	2.47e+03	2.39e+03	2.96e+03	2.88e+03	
	S_N 20	2.46e+03	2.35e+03	1.89e+03	1.81e+03	
max RE	S_N 5	4.89	4.85	2.86	2.84	
	S_N 7	7.71	7.64	4.35	4.32	
	S_N 10	3.74	3.69	6.71	6.64	
	S_N 12	14.3	14.1	0.764	0.748	0.0448
	S_N 15	14.7	14.3	3.87	3.79	
	S_N 17	14.8	14.4	7.98	7.78	
	S_N 20	14.1	13.5	6.09	5.85	
min RE	S_N 5	1.14e+03	1.13e+03	1.09e+03	1.09e+03	–
	S_N 7	1.37e+03	1.36e+03	1.26e+03	1.25e+03	–
	S_N 10	1.43e+03	1.41e+03	1.32e+03	1.3e+03	–
	S_N 12	1.46e+03	1.43e+03	1.33e+03	1.3e+03	–
	S_N 15	1.47e+03	1.43e+03	1.32e+03	1.3e+03	–
	S_N 17	1.46e+03	1.42e+03	1.31e+03	1.28e+03	–
	S_N 20	1.46e+03	1.39e+03	1.31e+03	1.26e+03	–
Time (mins)	S_N 5	302	305	1.13e+03	1.14e+03	
	S_N 7	324	327	1.62e+03	1.63e+03	
	S_N 10	414	420	2.11e+03	2.14e+03	
	S_N 12	406	414	2.09e+03	2.14e+03	22.3
	S_N 15	404	413	2.1e+03	2.14e+03	
	S_N 17	405	418	2.11e+03	2.17e+03	
	S_N 20	406	425	2.12e+03	2.21e+03	

Table 4.23: Figure of Merit results for steel beam embedded in concrete, with variations in quadrature order. Subdivisions of the table indicate calculations of the FOM using different relative errors. The analog case has a single value for each relative error as it is not dependent on changes in deterministic calculation parameters.

In the minimum relative error subsection of Table 4.23 the CADIS and CADIS- Ω FOM

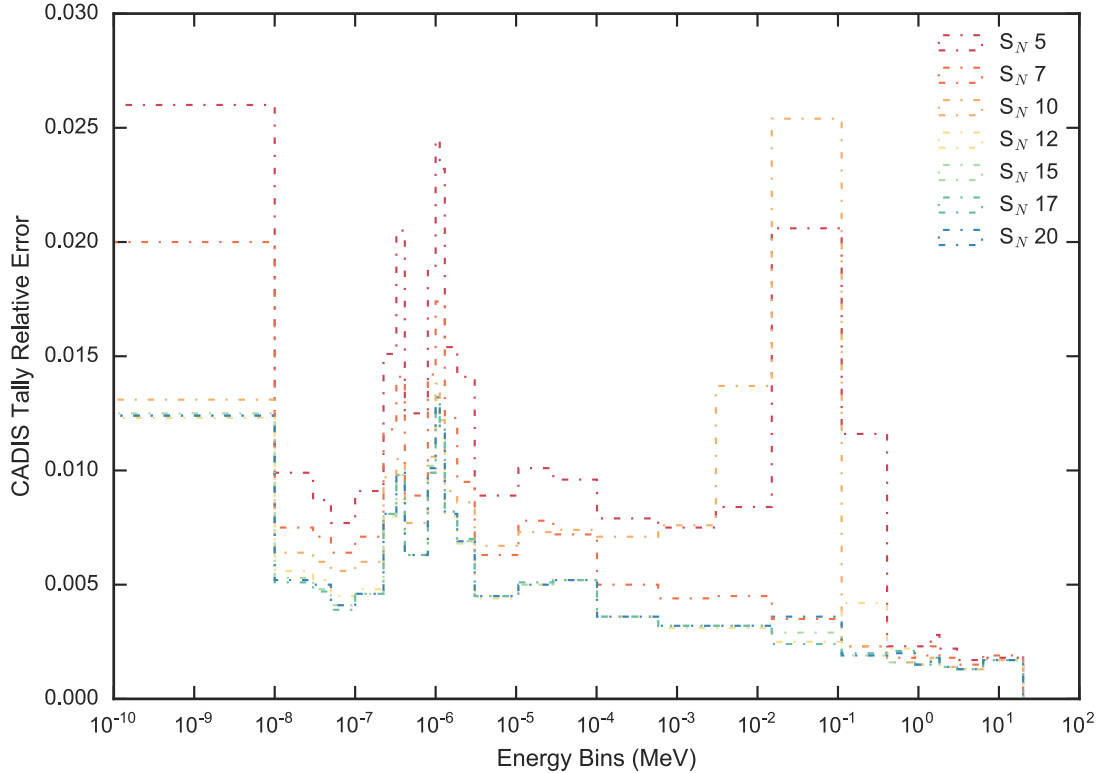
behavior is much more well-behaved than it is for the preceding two subsections of the table. There are no dips in the FOM value for either method, so the lowest relative error will consistently get better with increasing quadrature order. A slight shift to a $< 1\%$ lower FOM occurs for quadrature orders 17 and 20, which indicates that increasing quadrature fidelity does not help improve the FOM past S_N order 15. Similar behavior is observable for CADIS- Ω in the minimum relative error subsection of the table. CADIS- Ω has a consistently lower-valued FOM between 5%-10% for all quadrature orders when compared to CADIS. A turnover occurs in the CADIS- Ω FOMs at a lower quadrature order, meaning that CADIS- Ω does not benefit from increasing S_N order as much as CADIS using this FOM as a metric. However, beyond quadrature order 15 neither method sees a benefit in the FOM by increasing the quadrature order.

The timing results in the last section of the table show how much longer it takes CADIS- Ω to transport the standard Monte Carlo than CADIS. This was also noted in Section 4.2.4. In the introduction to this section, it was predicted that the I/O demands for CADIS- Ω would impact the MC_{hybrid} FOMs as quadrature order increases. However, because the CADIS- Ω Monte Carlo times are already so much longer than CADIS', this impact is not as significant as expected. Further, the increase in deterministic runtime seems to change similarly to the increase in Monte Carlo runtime as the importance map changes. This explains why the FOMs were not impacted so negatively in the previous sections of the table.

Let us use an illustrative example to compare the FOMs between CADIS and CADIS- Ω . Returning again to Table 4.23, at S_N order 5 the non-MC runtime is three minutes for CADIS, while it is around ten minutes for CADIS- Ω . At S_N order 20, the CADIS non-MC runtime is 19 minutes; the CADIS- Ω time is 100 minutes. For each of these cases, the non-MC runtime is about 4% that of the Monte Carlo runtime. Because this fractional time is fairly consistent between CADIS and CADIS- Ω , we do not see a strong impact on FOM_{hybrid} from the significantly longer non-MC runtimes in CADIS- Ω .

Table 4.23 shows that for the FOM using the tally average relative error, CADIS- Ω outperforms CADIS for most quadrature orders (with exceptions being S_N orders 7 and 12). For the majority of the quadrature orders, CADIS- Ω gets more particles to the tally region than CADIS in the same amount of time. By increasing quadrature order, CADIS- Ω generally increases the number of particles to the tally as a whole, while CADIS remains fairly constant. The table also shows that by using either the maximum or minimum relative error to calculate the FOM, CADIS generally outperforms CADIS- Ω . However, while both the maximum and minimum RE FOMs increase with increasing quadrature order in CADIS, this is not the case for the tally average FOM. This could be interpreted as that as the quadrature order increases, more particles reach the extreme tally bins, but fewer particles end up in the tally overall. For CADIS- Ω , this behavior is not quite the same. Instead, a peak occurs in the tally average FOMs at intermediate quadrature orders, and the minimum RE FOM decreases with increasing quadrature order.

In the Subsection 4.2, it was discussed that while the FOM shows how quickly a tally may approach a desired value, it does not show how effectively each method transported particles to the tally location. Because the same particle count was used in each variation

(a) Relative errors of CADIS results for differing S_N orders.

of the steel beam problem in the angle sensitivity study, the relative error results achieved by each method can reveal how well each method transported the same number of starting particles. The next several plots will present this information.

Figures 4.43a and 4.43b show the relative errors for all tally bins for each quadrature order run of the problem with the steel beam in concrete for CADIS and CADIS- Ω , respectively. Unlike Table 4.23, these plots show the overall behavior of the tally results as a function of changing quadrature order, so the behavior of non-extreme tally bins can also be observed. As noted in the discussion accompanying Table 4.23, these intermediate are important in evaluating the tally average relative error.

Figure 4.43a plots the tally relative error results for each of the CADIS runs, binned by energy. The warmer colored red and orange lines show the low quadrature order results, while the cooler colored lines correspond to higher quadrature results. For all of the energy bins below 10^{-4} MeV, a reduction in the relative error with increasing quadrature order can be observed. For quadrature orders S_N 12 and above, the relative error does not show as much of an improvement in the relative error. Between 10^{-4} and 10^0 MeV, large spikes in the relative error for quadrature orders 5 and 10 exist, explaining the poor behavior of the tally average RE FOM and tally maximum RE FOM for CADIS. Quadrature order 7 has

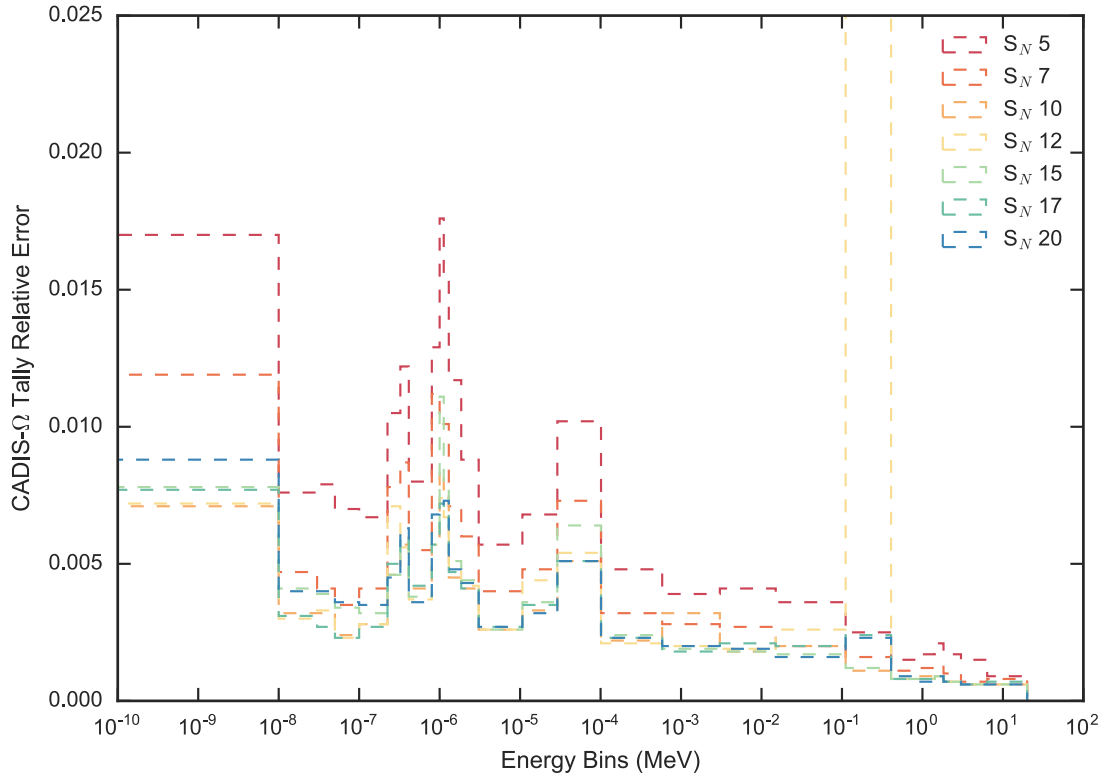
(b) Relative errors of CADIS-Ω results for differing S_N orders.

Figure 4.43: Relative error results for CADIS (Figure 4.43a) and CADIS-Ω (Figure 4.43b) for different quadrature orders for the problem with a steel beam in concrete.

relative errors much closer to quadrature orders 12 and above. Because these relative error spikes span so many bins, they affect the overall tally convergence, and, by extension, the tally average FOM. At very high energies ($> 10^0$ MeV), there is very little improvement in the relative error with increasing quadrature order.

Figure 4.43b shows the relative error results for CADIS-Ω. A number of interesting features exist in this figure that are not reflected in Figure 4.43a. For example, in the lowest energy region a decrease in the relative error is seen up to S_N 10, but then the relative error increases for higher S_N orders. In the wider energy bins between 10^{-6} and 10^{-1} MeV, quadrature orders 10 and above all achieve a similar relative error. This is not true in narrow energy bins, where higher quadrature orders do tend to have a lower relative error. Moving to higher energies, we can observe a significant spike in the relative error between 10^{-1} to 10^0 MeV for S_N order 12. Although this spike does not span several energy bins like those seen in Figure 4.43a, it is very high when compared to the other relative error bins. As a result, this single tally bin throws off the tally average FOM results in addition to the

tally maximum RE FOM, as observed in Table 4.23. In energy bins above this spike, most quadrature orders produce similar FOMs. The lowest valued energy bin is located in this high energy region.

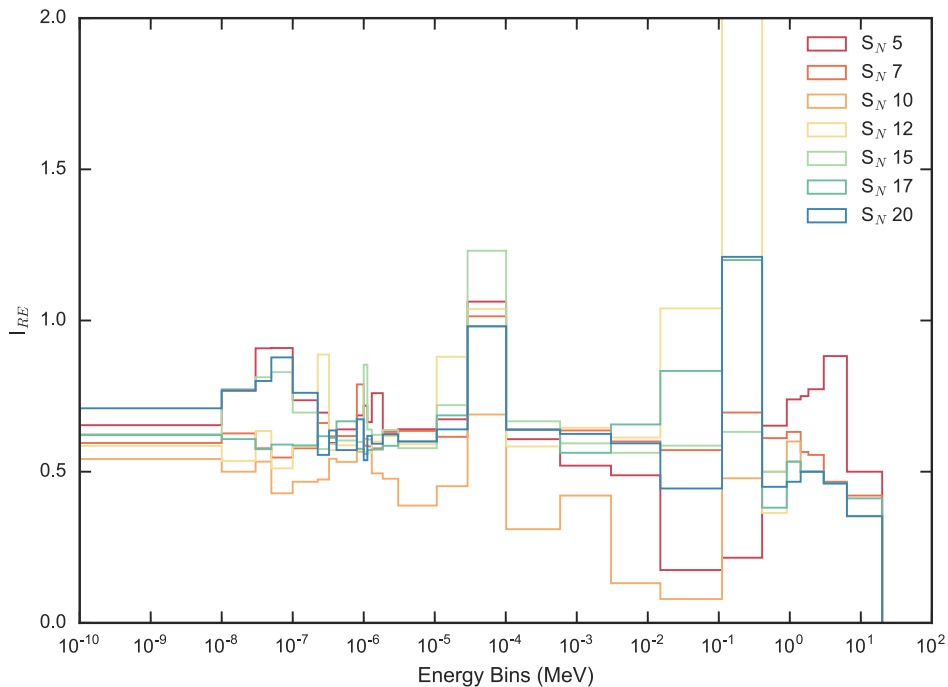


Figure 4.44: Relative error ratio (Eq. (4.1)) between CADIS- Ω and CADIS as a function of quadrature order for the problem with a steel beam embedded in concrete.

While Figure 4.43 shows the how the relative errors of the tally change with different quadrature orders, we have no indication of how CADIS and CADIS- Ω change in comparison to one another. Figure 4.44 shows the relative error improvement factor for each quadrature order. A value below unity indicates that CADIS- Ω achieved a better relative error than CADIS for that bin and quadrature order. In this figure we can clearly see the effect that the problematic energy bins in each method have on the improvement factor. In CADIS we observed that bins in the 10^{-3} to 10^{-1} were problematic for quadrature order 10; this is reflected in the very low value of I_{RE} for that energy range and quadrature order, as shown in by the orange line reaching the lowest values of I_{RE} . Conversely, we observed that CADIS- Ω had a very problematic energy bin between 10^{-1} and 10^0 at quadrature order 12. The value of this I_{RE} is far above the y-limit of Figure 4.43, illustrated with the yellow line.

Figure 4.43 also shows that quadrature order 10 is generally the order in which CADIS- Ω outperforms CADIS the most. For this quadrature error, CADIS- Ω achieves the lowest error when compared to CADIS. The reasons for this are twofold: first, it is one of the best performing quadrature sets for CADIS- Ω , which achieves its lowest relative errors in almost

every energy bin in this quadrature order; second, it is a very poorly performing quadrature set for CADIS. This synergistic combination results in the best overall quadrature order for CADIS- Ω .

A region where quadrature order 10 is not the best quadrature order is in energy regions above 10^{-1} MeV, where the higher quadrature orders—like 15, 17 and 20—outperform CADIS more. In the low ($< 10^{-5}$ MeV) and high ($> 10^0$ MeV) energy regions, CADIS- Ω obtains lower relative errors than CADIS for all quadrature orders. In intermediate energy regions, some spikes occur in regions that indicate a lower relative error is achieved by CADIS. However, generally CADIS- Ω achieves lower relative errors than CADIS for most energy bin and most quadrature orders. Returning again to the relative error figures of 4.43, the spike in I_{RE} between 10^{-5} and 10^{-4} MeV is explained by a relatively low relative error achieved by CADIS, where in CADIS- Ω a large spike in the relative error occurs. This is reflected in the ratio for I_{RE} .

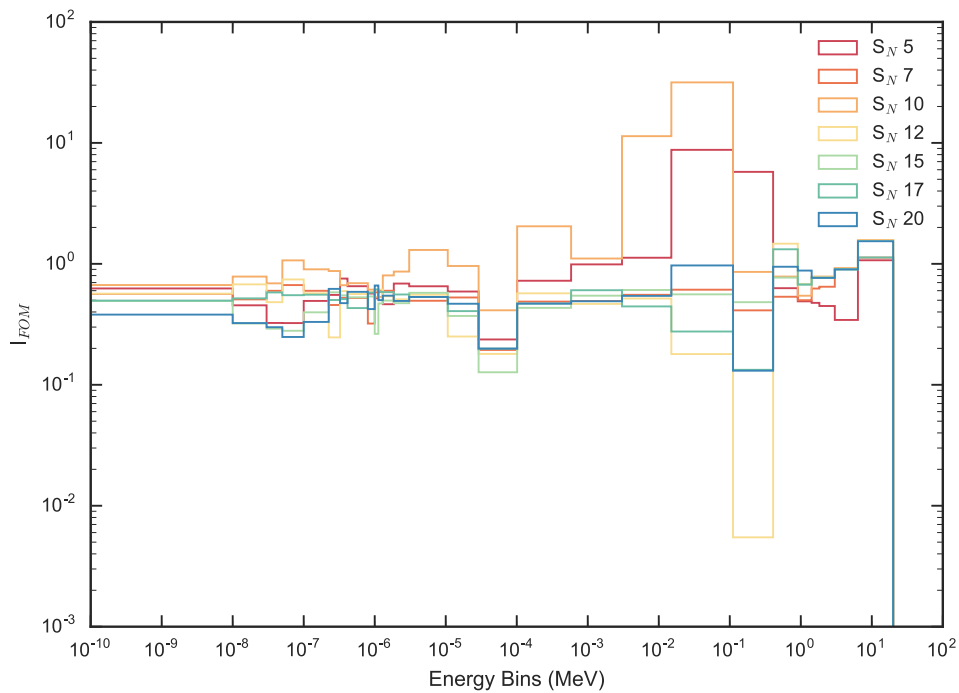


Figure 4.45: Figure of merit improvement factor (Eq. (4.2)) between CADIS- Ω and CADIS with changes in quadrature order for the problem with a steel beam embedded in concrete.

Figure 4.45 complements the results to Figure 4.44. Here the FOM improvement factor is plotted rather than the relative error improvement factor. Because a higher valued FOM is a better result, values above 10^0 indicate that CADIS- Ω outperformed CADIS. On this plot it is quite clear that for higher energies, CADIS- Ω consistently outperforms CADIS more in higher quadrature orders, as observed with I_{RE} .

Let us return again to the high and low-energy regions of the plot, as explored with Figure 4.44. In this region it can be observed that for low energies, generally I_{FOM} decreases with increasing S_N order. This behavior reverses at high energies, where the ratio increases with increasing quadrature order. This may be an effect of anisotropy in each energy group, as the highest energy has the most anisotropy in the flux. Recall from Section 4.2.4 that the anisotropy metric was much higher at high energies than it was at low energies. It is possible that for this more anisotropic energy group, increasing the quadrature order improves the importance map in the Ω methods more, resulting in a better relative error, and, consequently, a better FOM. This would also explain the complementary behavior at low energies. Low energies generally have more isotropic behavior, and increasing the quadrature order would not help to improve anisotropy information in the importance map. As a result, increasing quadrature order would not help the FOM at low energies.

Despite a higher relative FOM at high energies, in higher quadrature orders CADIS- Ω 's performance does not generally exceed CADIS'. For quadrature order 20, CADIS- Ω 's FOM is almost always lower than CADIS. On Figure 4.45, the cooler toned lines which correspond to higher quadrature orders have lower values than the warmer toned lines. For quadrature order 5, the relative errors on Figure 4.44 were bookended by higher order quadratures at middle and low energies. This behavior is not the same in Figure 4.45, where the lowest quadrature order has a higher relative FOM than any of the quadrature orders above 10. This means that the time required to solve higher quadrature orders affects the FOM more negatively than the quadrature order decreases the relative error (and positively affects the FOM). It could also mean that the relative error improvement changes more for CADIS than CADIS- Ω with increasing quadrature order. As a result, the improvement factor at lower quadrature orders is better for CADIS- Ω than at higher quadrature orders.

4.3.3 Scattering (P_N) Order

Table 4.24 is much like that of Table 4.23, but with differing P_N orders than quadrature orders. The table is split into four regions, the first three corresponding to FOMs calculated with different relative errors and the last corresponding to Monte Carlo and hybrid runtimes for the problem. Each of the three first subsections of the table have different trends with P_N order, which will be described in the next several paragraphs.

In the tally average relative error subsection of the table one can see that CADIS has a dip in the FOM for P_N order 3; both P_N orders 1 and 5 are higher overall. This effect is not seen in CADIS- Ω , where a decrease in the FOM is observed with increasing P_N order. As a result, for CADIS- Ω , lower P_N orders are sufficient for generating biasing parameters, but for standard CADIS the highest P_N order achieves the best tally average FOM. Further, for every P_N order, the tally average FOM is higher for CADIS- Ω than CADIS.

As with Table 4.23, a dip in CADIS' FOMs is also observable in the maximum relative error subsection of the table. However, the dip observable at P_N order 3 also exists in the CADIS- Ω FOMs. If a user desires to have all tally bins to be below a particular relative

error, P_N order 3 is the worst option for both methods in this problem. For P_N order 1 CADIS- Ω is the better choice, and for P_N order 5, CADIS is the better choice.

		CADIS		CADIS- Ω		analog
P_N order		MC	MC_{hybrid}	MC	MC_{hybrid}	MC
tally avg	P_N 1	1.76e+03	1.74e+03	2.99e+03	2.96e+03	
	P_N 3	671	661	2.97e+03	2.94e+03	1.39
	P_N 5	2.21e+03	2.16e+03	2.45e+03	2.42e+03	
max RE	P_N 1	7.19	7.09	8.06	7.98	
	P_N 3	3.75	3.7	6.74	6.66	0.0448
	P_N 5	14.8	14.5	8.24	8.12	
min RE	P_N 1	1.5e+03	1.48e+03	1.33e+03	1.31e+03	–
	P_N 3	1.43e+03	1.41e+03	1.32e+03	1.31e+03	–
	P_N 5	1.24e+03	1.22e+03	1.57e+03	1.55e+03	–
time (mins)	P_N 1	394	399	2.09e+03	2.11e+03	
	P_N 3	413	419	2.1e+03	2.13e+03	22.3
	P_N 5	559	571	2.55e+03	2.59e+03	

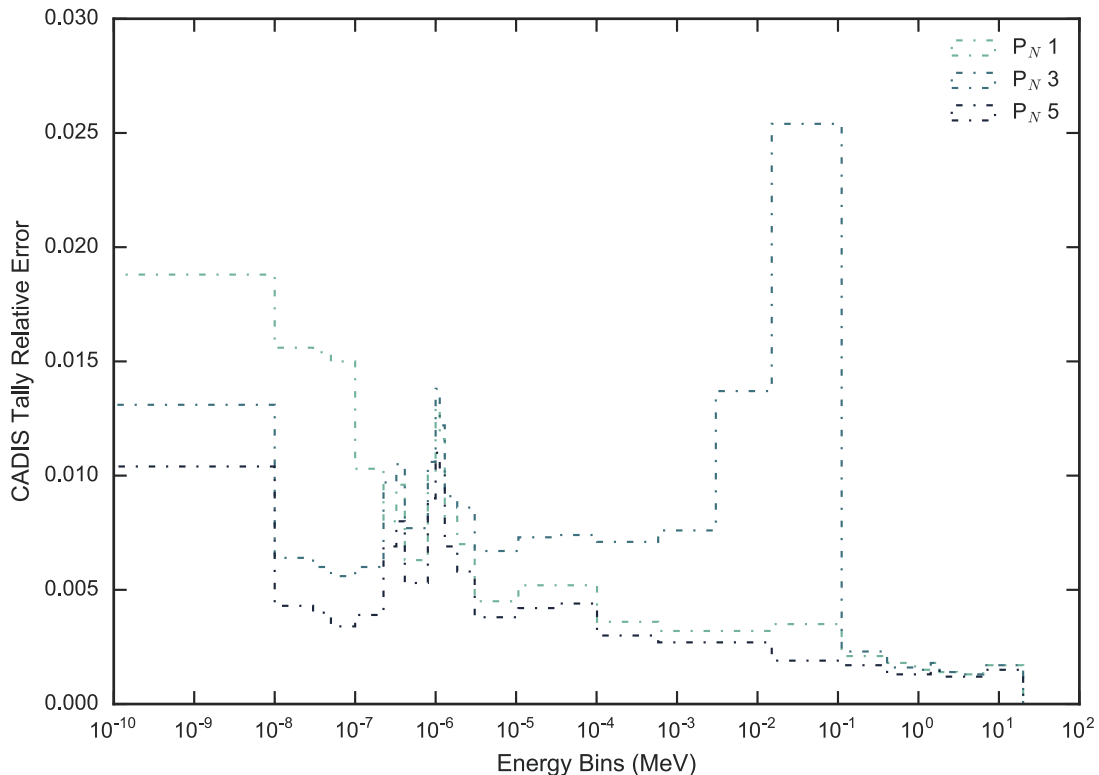
Table 4.24: Figure of Merit results for steel beam embedded in concrete, with variations in P_N order. Subdivisions of the table indicate calculations of the FOM using different relative errors. The analog case has a single value for each relative error as it is not dependent on changes in deterministic calculation parameters.

Comparing the FOMs for CADIS and CADIS- Ω using the minimum relative errors, some interesting trends are visible. In Table 4.23 we observed that as quadrature order increased, the minimum relative error FOM generally increased or stayed the same for both CADIS and CADIS- Ω . This is not the case in Table 4.24. As P_N order increases, the minimum relative error FOM for CADIS decreases, but for CADIS- Ω it increases. This means that increasing P_N order does not move more particles (and reduce the relative error) in the energy bin with the lowest relative error in CADIS, but it does in CADIS- Ω . Unlike the maximum relative error subsection of the table, at low P_N order CADIS outperforms CADIS- Ω , and at high P_N orders CADIS- Ω outperforms CADIS.

As with Table 4.23, Table 4.24 shows that the behavior of the FOMs do not follow the same trends between different relative error measurements. Depending on the user requirements for the method, one may be a better option than the other. For example, in comparing the FOMs using the maximum relative error, CADIS is better with higher P_N order. With the FOMs using the minimum relative error, CADIS- Ω is better with higher P_N orders.

Looking at the timing results in the last section of the table, we can see that CADIS- Ω takes at least five times longer than CADIS to perform a hybrid run. This is similar to

what was observed for the quadrature order results. However, increasing P_N order increased CADIS Monte Carlo runtimes roughly 40% between P_N orders 1 and 5, and increased CADIS- Ω runtimes about 22% for the same quadrature orders. While the total amount of time added to CADIS- Ω runtimes is longer, it is relatively less than the amount that was added to CADIS.



(a) Relative errors of CADIS results for differing P_N orders.

Figures 4.46a and 4.46b provide additional information on interpreting Table 4.24. Figure 4.46a shows the tally relative error results for each of the P_N order CADIS runs, and Figure 4.46b shows the relative error results for CADIS- Ω . In Figure 4.46a the highest relative error for CADIS' P_N order 1 is the most thermal energy bin, for P_N order 3 is the tally bin between 10^{-2} , and for P_N order 5 is the resonance region around 10^{-6} . The lowest relative error bin, however, is the same for all P_N orders. This bin is located just below the highest energy bin. The shifting location of the highest valued relative error energy bin helps to explain the strange trend of the FOMS in the second region of Table 4.24. Because the relative error bins become larger in epithermal energy groups at P_N order 3, and this shift spans several energy bins, it also helps to explain the tally average FOM shift to a lower value at P_N order 3.

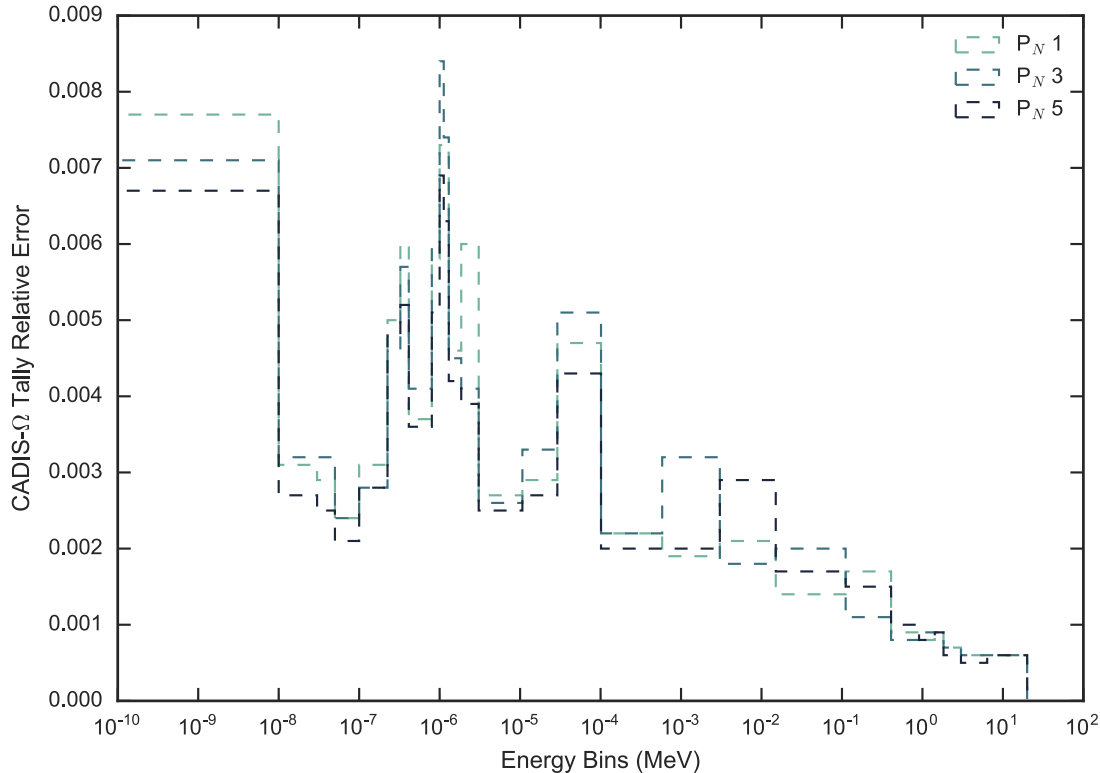
(b) Relative errors of CADIS-Ω results for differing P_N orders.

Figure 4.46: Relative error results for CADIS and CADIS- Ω with changes in P_N order for the problem with a steel beam in concrete.

In Figure 4.46b, no significant shift in the relative error happens at P_N order 3. However, we can observe a shifting location of the highest valued relative error. At P_N order 1 the highest valued relative error for CADIS- Ω is the lowest energy bin. At P_N order 3 the highest relative error bin is the resonance region located near 10^6 MeV, and at P_N order 5 these two bins appear to have a similar relative error. The highest overall observed relative error occurs in P_N order 3, which is why we see the shift to a lower FOM at P_N order 3 for the maximum relative error subsection of Table 4.24. This shift is not as significant as the several-bin spanning shift in CADIS, so it does not affect the tally average FOM in CADIS- Ω .

From Figures 4.46b and 4.46a, we can conclude that shifts in the relative error that dramatically change between P_N orders can affect the overall tally convergence. This shift is not predictable, and may not be observed if combined with a different set of deterministic parameters, such as quadrature order 15, where both CADIS and CADIS- Ω have no spikes in their relative errors.

Figure 4.47 shows the relative error improvement factor by different P_N orders. This plot

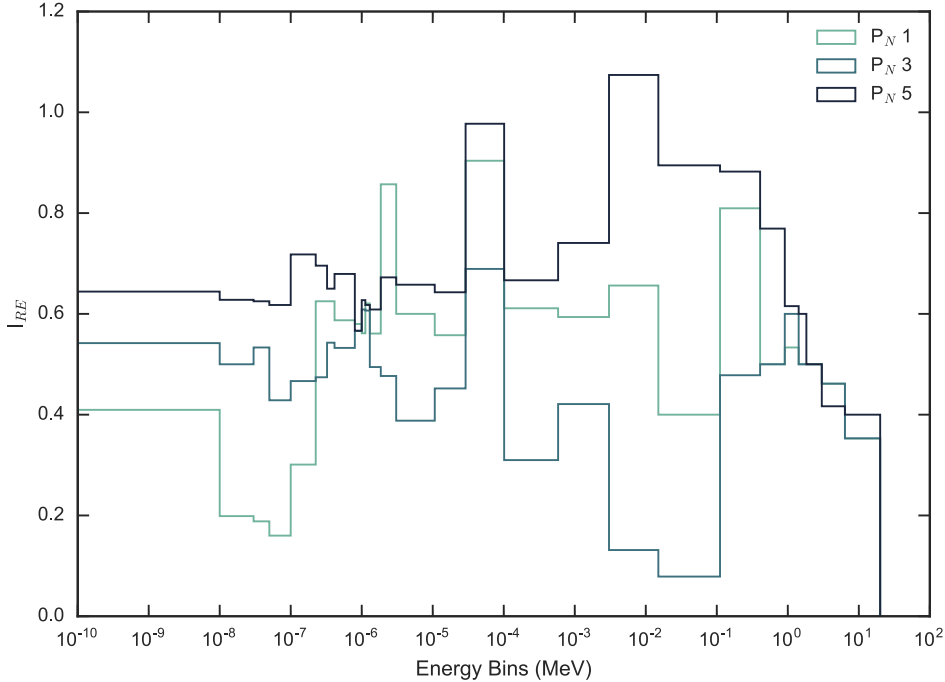


Figure 4.47: Relative error improvement factor (Eq. (4.1)) between CADIS- Ω and CADIS with changes in P_N order for the problem with a steel beam embedded in concrete.

complements what was observed in Figure 4.44. Recall that a value below unity indicates that CADIS- Ω achieved a better relative error than CADIS for a given energy bin and quadrature order. First, with the exception of a few energy bins in P_N order 5, CADIS- Ω has better relative errors than CADIS for the majority of P_N orders and energy bins. In general, P_N order 3 has the most energy bins that obtain low values of I_{RE} , and P_N order 5 has the fewest.

Another interesting feature illustrated in this plot is that different P_N orders perform the best in distinct energy regions. At low energies P_N order 1 achieves the best relative errors, at intermediate energies P_N order 3 achieves the best relative errors, and at high energies all three perform similarly.

For all three P_N orders, the energy bin located near 10^{-4} MeV is problematic. Returning again to the relative error plots of Figures 4.46a and 4.46b, this particular energy bin had a spike for CADIS- Ω , but remained relatively small for CADIS. The consistency in each method's performance across all P_N orders is reflected in this problematic energy bin.

Figure 4.48 shows the FOM improvement factor with increasing P_N order. As with the quadrature orders, the runtimes of CADIS- Ω impact the FOMs that it achieves such that many more energy bins are more in CADIS' favor than in the relative error plot. However, many more energy bins are above 10^0 I_{FOM} in P_N order than for quadrature order. As

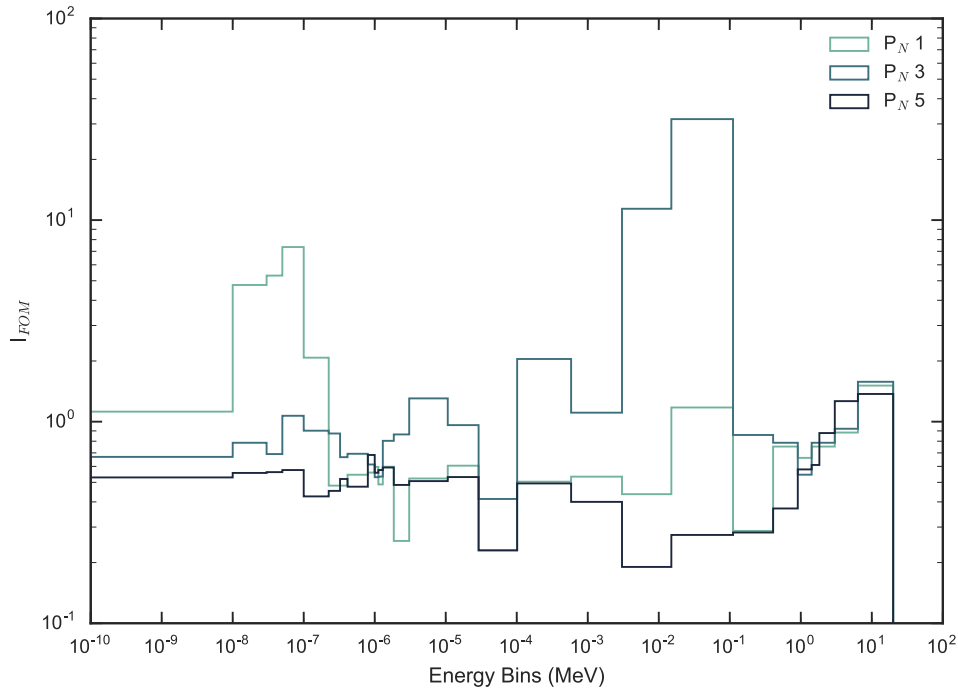


Figure 4.48: Figure of merit improvement factor (Eq. (4.2)) between CADIS- Ω and CADIS as a function of P_N order for the problem with a steel beam embedded in concrete.

with I_{RE} , the shift in performance in different energy groups changes with P_N order. At low energies, P_N order 1 achieves the best FOMs for CADIS- Ω , at intermediate energies P_N order 3, and at high energies all three P_N orders have superior performance with CADIS- Ω .

It should be noted that there is no P_N order for which CADIS- Ω obtains better FOMs than CADIS in all energy bins. Contrast this to the relative error plot, where CADIS- Ω had almost universally better relative errors than CADIS. Again this underscores the negative impact that time has on CADIS- Ω 's FOM.

4.3.4 General Observations

At this point we are interested in which deterministic parameter value affects CADIS- Ω and CADIS' performance more significantly. We have looked at how varying each metric changes the relative error, I_{RE} , and I_{FOM} , and from that we have observed trends associated with varying each parameter. However, we have not compared each metric against the other. Figures 4.49 and 4.50 aid in this comparison. As with P_N order and S_N order, these plots show either the relative error or Figure of Merit results for the angle sensitivity study. Unlike the plots with I_{RE} and I_{FOM} , these figures show how the FOM and relative error change for a single method. That is, how much does the relative error or the Figure of Merit

change between the lowest- and highest- valued parameters run for CADIS or CADIS- Ω . These figures are useful to show how sensitive CADIS and CADIS- Ω are to P_N order and quadrature order, respectively.

In Figure 4.49, the ratio of the relative error in each tally bin is taken between the lowest and highest-valued parameter run of the parametric study. For P_N order (the purple lines in the figure) this is calculated with RE_{P_N1}/RE_{P_N5} and for quadrature order (the green lines in the figure) it is calculated with RE_{S_N5}/RE_{S_N20} . A ratio above unity means that the relative error obtained by the higher-valued parameter (P_N order 5 or S_N order 20) is lower than that of the lower-valued parameter.

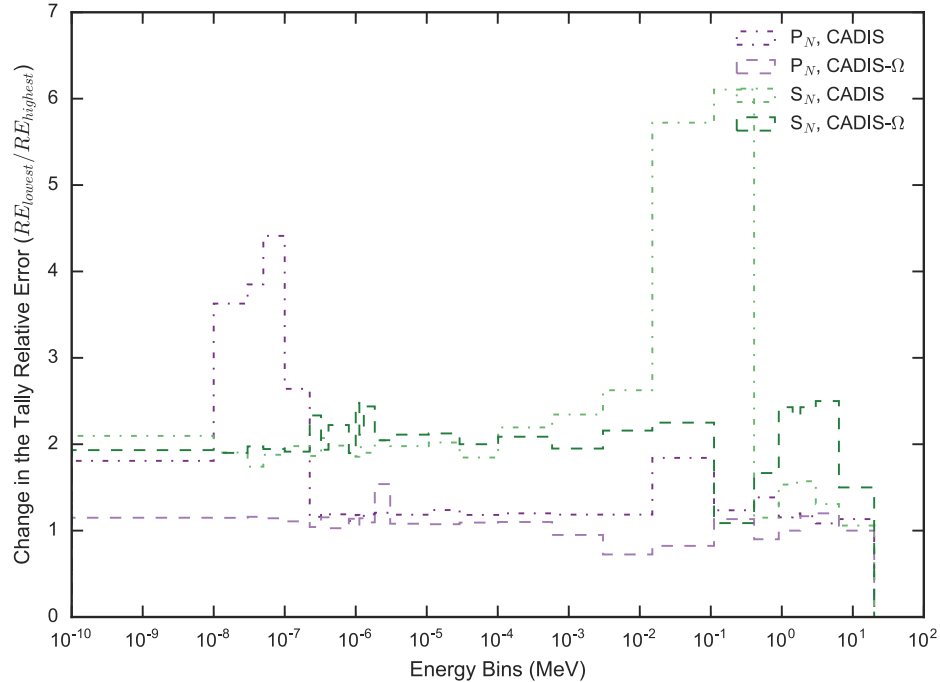


Figure 4.49: Ratio in the relative errors between the lowest and highest variable in the angle sensitivity study for CADIS and CADIS- Ω .

Figure 4.49 shows that a greater change in the relative error occurs for both CADIS and CADIS- Ω from S_N order 5 to 20 than it does for P_N orders. A notable exception to this is for CADIS in the energy range from 10^{-8} to 10^{-7} MeV, where the relative error improvement for P_N order exceeds any quadrature order line. Returning to the relative error results for just CADIS, as shown in Figure 4.46a, this energy range has a very high relative error for P_N order 1, especially when compared to the other energy regions nearby. In this energy range, the relative error drops from 0.015 to .005 from P_N order 1 to 3, but the energy bin immediately adjacent only drops about .005 total. The greater change in the relative error for this region accounts for the spike we see in Figure 4.49.

The data in this figure also shows us that increasing P_N order for CADIS- Ω does not reduce the relative error in the energy range from 10^{-3} to 10^0 MeV. CADIS- Ω 's purple line on this figure is located below unity in that energy region. Generally this line for CADIS- Ω does not see a huge improvement with increasing P_N order. For a problem like this, a low P_N order may be a good enough choice.

CADIS' results in the same energy region show improvement in the relative error. However, in many centrally-located energy bins, this improvement is very small. If a tally existed for a similar problem in these energy ranges, it may be sufficient to use CADIS with a low P_N order as well.

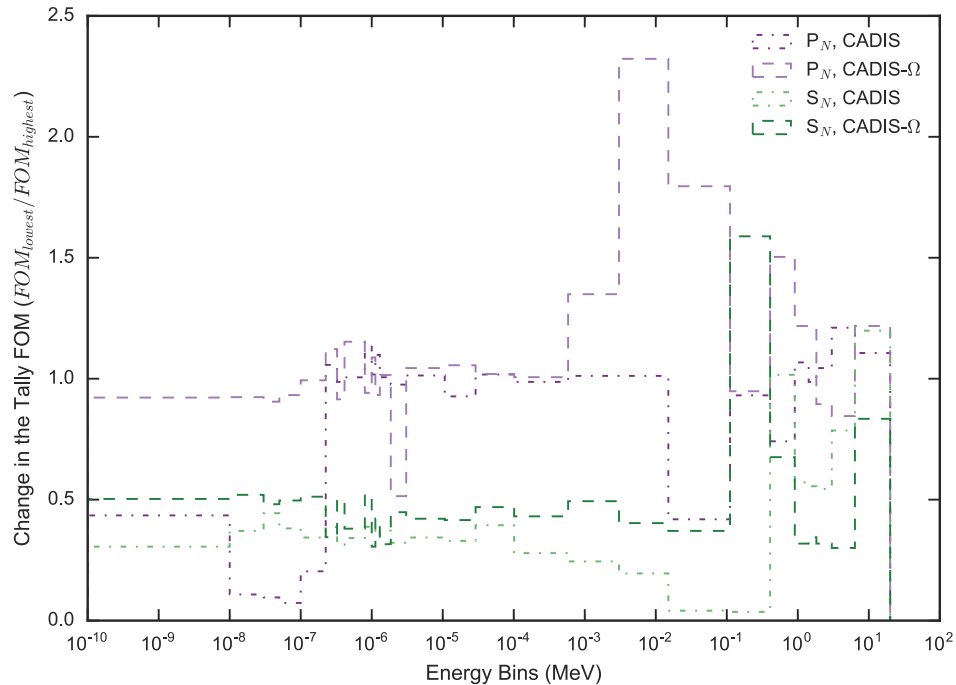


Figure 4.50: Ratio in the figure of merits between the lowest and highest variable in the angle sensitivity study for CADIS and CADIS- Ω .

In Figure 4.50, the linestyles and colors match those in Figure 4.49. The y-axis of this figure shows the ratio of the FOMs for the lowest- and highest-valued parameters. The purple lines are calculated by the ratio of FOM_{P_N1}/FOM_{P_N5} ; the green lines show the ratio of FOM_{S_N5}/FOM_{S_N20} ; the linestyles indicate the method type. In this plot, a low-valued ratio reflects a higher valued FOM obtained by the finer P_N or S_N order.

Some features from 4.49 are continued in Figure 4.50. For example, the energy bins between 10^{-8} and 10^{-7} MeV still show a large change for P_N order in CADIS. However, the addition of time to calculate the FOMs affects both methods. In Figure 4.49, we observed that for both methods, increasing P_N order or quadrature order generally decreased the

relative error. In Figure 4.50, this is not the case. At low energies, all methods have higher FOMs with increasing parameter resolution. At intermediate energies, only S_N order strongly changes the FOM. At high energies, energy bins for both S_N and P_N order wildly oscillate between improved and not improved.

The CADIS lines in Figure 4.50 generally lie at lower values than CADIS- Ω . Consequently, larger changes in the FOM are observable with increasing either P_N or S_N order. This is the case for most energy bins, but not above 10^0 MeV. In this region, CADIS- Ω and CADIS shift between energy bins in which method sees a larger change with parameter value selection.

By inspecting both Figure 4.49 and 4.50, a few common themes appear. First, CADIS has a larger change in the tally relative error and FOM than CADIS- Ω for most energy bins. Second, this general observation does not hold for energy bins greater than 10^{-1} . At these energy regions, CADIS- Ω achieves a better relative error with increasing S_N order, but not P_N order. Neither CADIS- Ω or CADIS have a dominant trend in FOM values in this region. Another observation is that generally S_N order has a greater effect on the relative errors and FOMS for both methods. This is not the case in the high energy region for FOM values, where both methods are comparable.

4.4 Method Recommendations

The performance of CADIS- Ω has been characterized and compared against CADIS and a standard, nonbiased analog Monte Carlo run for a series of problems. Section 4.2 showed how varying geometric configuration and material composition of various problems with anisotropy affected the performance of the Ω methods. Subsections 4.3.3 and 4.3.2 showed how varying P_N order and quadrature order changed the tally results and tally convergences for the steel beam problem embedded in concrete. In doing this characterization, we sought to determine in which problems and with which solver options the Ω methods were best suited. A secondary objective was to determine the sensitivity of the Ω -methods to changes in the solver options. With these objectives in mind, we can evaluate the Ω methods' performance based on the study performed in the preceding subsections.

4.4.1 Problem Selection

Section 4.2 revealed that CADIS- Ω does not outperform CADIS for all problems containing anisotropy in the flux. Depending on how and where the flux anisotropy was induced in the problem, CADIS- Ω had the potential to significantly increase the FOM in Monte Carlo. These results were not consistent, and are not entirely predictable.

In comparing the single turn and multiple turn labyrinths, it was observed that more scattering effects decrease the effectiveness of CADIS- Ω . Because more scattering is required to penetrate the multiple turn labyrinth, the performance of CADIS- Ω was poorer. In the

single turn labyrinth energy bins that had more isotropy in the flux induced by scattering also were poorer performing for CADIS- Ω .

To add to this complexity, problems with little- to no- scattering were also difficult for CADIS- Ω to handle. These problems were also problematic for CADIS, as they were generally comprised of “thin” materials to induce streaming effects. As a result, sampling events occurred over several centimeters, which also was over several orders of magnitude in flux change. This resulted in very high relative errors, as observed in the beam facility problem. This was not as problematic in the therapy room example because the problem was bounded by 10cm of concrete, which allowed for particle scattering rather than leakage.

Several material variants of the steel beam in concrete problem were run. The results of this small study confirmed that both CADIS and CADIS- Ω obtain poorer FOMs with air than with steel or concrete. In the case of the air variant, the FOMs obtained by CADIS- Ω were generally lower than CADIS, but the relative errors were also better. For all material variants of the steel beam problem, CADIS and CADIS- Ω achieved superior FOMs to the nonbiased analog, but these were an order of magnitude lower for the air variant.

The rebar-embedded concrete problem showed that for problems with geometric complexity, CADIS- Ω can also struggle. Because the rebar in this problem was not always directed in line with the detector tally, particles could more freely move perpendicular to the tally path, crossing out of importance with a preferential flowpath. As a result, in high energy bins the tally relative error was very high for both CADIS and CADIS- Ω . However, CADIS- Ω ’s performance was poorer. The FOMs obtained by CADIS- Ω in this problem were one to two orders of magnitude smaller than CADIS or the nonbiased analog.

CADIS- Ω achieved lower relative errors than CADIS for many problems, but often this was offset by a very long runtime. The long runtime impacted the FOM. As a result, even though CADIS- Ω achieves a lower relative error for the same particle count, it may be more advantageous to simply run standard CADIS for longer. In a few instances, the runtime for CADIS- Ω is comparable to CADIS. This occurs in the beam and therapy room problems, for example. Although these problems are not the best for either CADIS or CADIS- Ω , there is no caveat to using CADIS- Ω if choosing a hybrid method.

The characterization problems’ variations in material and geometric configuration showed that there is no distinct behavior for which CADIS- Ω is universally better. However, in problem geometries where preferential flowpaths are directed towards the tally detector, and where materials provide short mean free paths to interaction or resampling sites, CADIS- Ω is a well-suited method.

4.4.2 Deterministic Solver Choice

The angle-based parametric study provided a number of interesting observations on the performance of the Ω methods. First, the effect of T_{det} does not change the FOM with CADIS- Ω more than CADIS. In Section 4.3.2 the hypothesis that I/O requirements would severely impact the FOM for CADIS- Ω was shown to not be as impactful as hypothesized. The FOM

change between FOM_{MC} and FOM_{hybrid} was roughly the same for CADIS as CADIS- Ω because the CADIS- Ω runtimes are so much longer than CADIS.

Next, the only consistent region in which CADIS- Ω outperforms CADIS is in high energies. For almost all P_N orders and all quadrature orders, CADIS- Ω achieved lower relative errors and higher FOMs than CADIS. In high energy bins, increasing quadrature order showed a decrease in I_{RE} , increasing P_N order did not show a large change in I_{RE} . In the same bins, I_{FOM} values above unity were observed for both P_N and S_N order, but no trends with changing parameter value were observed.

By including the runtime to calculate the FOM, the comparative performance of CADIS- Ω dropped when compared to using the relative error. Several energy bins in CADIS- Ω —for quadrature orders and P_N orders—achieved better FOMs than CADIS. However no P_N order consistently outperformed the other, while low S_N orders generally achieved better FOMS for CADIS- Ω than CADIS. However, despite the lack of consistent performance for a single P_N order, the raw values obtained with P_N order are promising. With P_N order there were more energy bins that had high I_{FOM} values than with quadrature order.

Another observation that can be extended from Section 4.2 is that CADIS- Ω consistently biases particles better than CADIS. For the same number of source particles, CADIS- Ω achieves lower relative error than CADIS for most energy bins with both P_N order and quadrature order. This means that while sampling may be slow, the importance map generated with the Ω flux is generally better at moving particles to the tally region than CADIS.

Based on the results in Section 4.3, a number of recommendations can be made based on deterministic solver choice. First, the best P_N order choice is dependent on the energy range in which one is tallying. For low energy regions, P_N order 1 will give the best FOMs relative to CADIS, for intermediate energies P_N 3 is a better choice, and for high energies any P_N order is satisfactory. In general, because lower P_N orders have lower runtimes, these will get the best results for CADIS- Ω the fastest, and have comparatively the best relative errors and FOMs against CADIS. Next, the best S_N order choice is

If one has to choose between varying P_N order and S_N order to improve the importance map for their method, varying S_N order will have a greater impact. This is the case for using either CADIS or CADIS- Ω . However, both methods have a turnaround point at which increasing S_N order does not improve the relative error enough to offset the time increase of the method. For CADIS- Ω , this occurs in bins above S_N 15, and for CADIS it occurs in bins above S_N 12. For this type of problem, and using all energy bins in the tally, CADIS- Ω will obtain the best results with a lower P_N order and intermediate S_N orders.

4.4.3 Lessons Learned

The characterization problems that were run were heavily biased towards low-density streaming to induce anisotropy in the flux. This subset of problems, though highly anisotropic, are not the best for a method so dependent on weight-window type biasing, because particle streaming allowed for particles to cross several orders of magnitude in the flux before resampling. This meant that in a high-importance region a particle may split many thousands

of times in a new splitting event. Unfortunately, the Ω -methods are not immune to this issue and so suffered the same effects as CADIS, even with positive effects like the reduction of ray effects. Further, with the strong dependence on angle, the Ω -fluxes may have exacerbated this streaming-sampling effect in regions with strong angular dependence around the detector. In a problem like the single turn labyrinth, where the Ω -flux generated a strong line of importance between the exit of the labyrinth and the detector and drastically dropped the importance behind the detector, a particle has much more opportunity to cross several orders of magnitude of importance than it does in CADIS. This is likely what caused CADIS- Ω to take longer in Monte Carlo transport than CADIS in many of the characterization problems.

It should also be noted that while the angle-dependent parametric study revealed how P_N order and quadrature order may affect a problem's results, the best parameter choices for this problem are by no means a prescriptive solution for other problems. Section 4.2 showed how different the characterization problems' results were, depending on the source definition, the material composition of the problem, and the geometric configuration of the problem. Using the deterministic parameter choices that appear the best for the steel beam in concrete may not be the best for, say, a multi-turn labyrinth. From this study we have a good starting point from which to further characterize the method for other application problems.